



ADAM MICKIEWICZ UNIVERSITY, POZNAŃ
FACULTY OF PHYSICS
ASTRONOMICAL OBSERVATORY INSTITUTE

DETERMINATION OF PHYSICAL AND
DYNAMICAL PROPERTIES OF ASTEROIDS
OBSERVED BY THE *Gaia* MISSION

KAROLINA JADWIGA DZIADURA

PHD THESIS

Supervisor

Prof. UAM Dr Hab. Przemysław Bartczak

Auxiliary supervisor

Dr Dagmara Oszkiewicz

in Adam Mickiewicz University, Poznań

JANUARY 2024

Summary

Asteroid studies are essential for understanding the formation and evolution of the Solar System and other planetary systems, as well as investigating the origins of water on Earth. Crucial to these studies is the determination of physical properties, such as size and density, which are useful for various applications, including assessing the Yarkovsky effect. The main objective of this thesis was to determine asteroid sizes from the occultation data and to create an efficient approach to utilize the ultraprecise *Gaia* DR2 and DR3 data to determine the Yarkovsky effect.

Gaia not only improves the quality of ground-based and satellite asteroid astrometry by applying its precise stellar catalog for an astrometric reduction but also provides a large number of asteroid astrometry data itself. In this thesis those data were incorporated into the orbit computation using its full covariance matrix along with radar data from the JPL Horizon (if available) and ground-based and satellite data from the MPC. The search for non-gravitational transverse acceleration was a central part of this investigation.

Moreover, I verified and used a new, more precise weighting scheme for astrometry that takes into consideration factors such as the year of observation, the observatory code, the apparent magnitude, the type of observations, and the stellar catalog used for reduction. I also developed new verification methods to cross-check the results. Orbits were computed using different observational arcs. Ultimately, the analysis of the Yarkovsky effect on asteroids allowed for the determination of their densities, which is the least known asteroid parameter.

Furthermore, the precision of stellar measurements provided by the *Gaia* mission has opened new avenues for observing a greater number of occultation events. The study also focused on the creation of a more complex approach to utilize the occultation data, including its uncertainties, for the determination of the asteroid sizes.

In the context of a potentially hazardous asteroid (PHA), precise size and orbit determination along with an understanding of the astrometry constraints are crucial for impact monitoring. This research has analyzed a few PHAs and provides accurate orbit predictions. By applying factors like the Yarkovsky effect, we have enhanced orbit determination, marking an advancement in the practical aspect of PHA monitoring.

Keywords

Asteroids, Astrometry, Yarkovsky effect, Occultations, *Gaia*, Dynamics, Celestial mechanics, Orbit determination, Minor planets

Streszczenie

Badania nad planetoidami są kluczowe dla zrozumienia procesów formowania i ewolucji Układu Słonecznego oraz innych systemów planetarnych, a także dla badania pochodzenia wody na Ziemi. Istotne w tych badaniach jest określenie fizycznych właściwości, takich jak rozmiar i gęstość, które są przydatne w różnych zastosowaniach, w tym w ocenie efektu Jarkowskiego. Głównym celem tego badania było określenie rozmiarów planetoid na podstawie danych z zakryć gwiazdowych oraz stworzenie efektywnej metody wykorzystania danych *Gaia* DR2 i DR3 do określenia efektu Jarkowskiego dla planetoid.

Gaia nie tylko poprawia jakość naziemnej i satelitarnej astrometrii planetoid, wykorzystując swój precyzyjny katalog gwiazd do redukcji astrometrycznej, ale również dostarcza obszernych danych astrometrycznych samych planetoid. Dane te zostały włączone do obliczeń orbit wraz z danymi radarowymi z JPL Horizon (o ile dostępne) oraz danymi naziemnymi i satelitarnymi z MPC. Poszukiwanie niegrawitacyjnych przyspieszeń było kluczowym elementem tego badania.

Badanie skupiło się również na stworzeniu bardziej złożonej metody wykorzystania danych z zakryć, w tym ich niepewności, do określenia rozmiarów planetoid.

Zastosowano metody weryfikacji do sprawdzania wyników. Orbits zostały obliczone przy użyciu różnych łuków obserwacyjnych. Ostatecznie analiza efektu Jarkowskiego pozwoliła na określenie gęstości planetoid, dostarczając kluczowych parametrów do zrozumienia fizycznych właściwości i ewolucji tych małych ciał niebieskich.

Ponadto, precyzja pomiarów gwiazdowych dostarczonych przez misję *Gaia* otworzyła nowe możliwości obserwacji większej liczby zakryć gwiazd przez planetoidy. Badanie skupiło się również na stworzeniu bardziej złożonego podejścia do wykorzystania danych o okultacjach, włączając ich niepewności, w celu określenia rozmiarów planetoid.

W kontekście potencjalnie niebezpiecznych planetoid (PHA), precyzyjne określenie rozmiaru i orbity wraz ze rozumieniem ograniczeń astrometrycznych jest kluczowe dla monitoringu zagrożeń. Niniejsze badanie przeanalizowało kilka PHA i przedstawia ich dokładne orbity. Uwzględniając czynniki takie jak efekt Jarkowskiego, udało się poprawić określenie orbity, oznaczając postęp w praktycznym aspekcie monitoringu PHA.

Słowa kluczowe

Planetoidy, Astrometria, Efekt Jarkowskiego, Zakrycia, *Gaia*, Dynamika, Mechanika nieba, Wyznaczanie orbit, Małe ciała Układu Słonecznego

Contents

List of publications	9
I Current state of the knowledge	15
Asteroid astrometry	17
Orbit determination	24
The Yarkovsky effect	28
II Scientific goals and results	35
Research goals	37
Results	38
Summary and future prospects	50
Bibliography	54
III Publications	65

List of publications

This dissertation has been written as a summary of the scientific activities previously reported in the following articles:

1. **Physical parameters of selected Gaia mass asteroids**

E. Podlowska-Gaca, A. Marciniak, V. Alí-Lagoa, P. Bartczak, T. G. Müller, R. Szakáts, R. Duffard, L. Molnár, A. Pál, M. Butkiewicz-Bąk, G. Dudziński, K. Dziadura, P. Antonini, V. Asenjo, M. Audejean, Z. Benkhaldoun, R. Behrend, L. Bernasconi, J. M. Bosch, A. Chapman, B. Dintinjana, A. Farkas, M. Ferrais, S. Geier, J. Grice, R. Hirsh, H. Jacquinet, E. Jehin, A. Jones, D. Molina, N. Morales, N. Parley, R. Poncy, R. Roy, T. Santana-Ros, B. Seli, K. Sobkowiak, E. Verebélyi and K. Żukowski

Astronomy & Astrophysics 638, A11, 2020

2. **Investigating the most promising Yarkovsky candidates using Gaia DR2 astrometry**

K. Dziadura, D. Oszkiewicz, P. Bartczak

Icarus 383, 115040, 2022

3. **The Yarkovsky effect and bulk density of near-Earth asteroids from Gaia DR3**

K. Dziadura, D. Oszkiewicz, F. Spoto, B. Carry, P. Tanga, P. Bartczak

Astronomy & Astrophysics 680, A77, 2023

Abbreviation	Explanation
MBA	Main Belt Asteroids
NEA	Near-Earth Asteroids
NEO	Near-Earth Objects
PHA	Potentially Hazardous Asteroid
PHO	Potentially Hazardous Objects
TNO	Trans-Neptunian Objects
SSO	Soar System object
NGTA	Non-gravitational Transverse Acceleration parameter (A_2 or da/dt)
RA	Right ascension
DEC	Declination
RMS	root mean square
SNR	Signal-to-noise ratio
<i>Gaia</i> DR2	<i>Gaia</i> Data Release 2
<i>Gaia</i> DR3	<i>Gaia</i> Data Release 3
<i>Gaia</i> FPR	<i>Gaia</i> Focus Product Release
UCAC-4	The Fourth U.S. Naval Observatory CCD Astrograph Catalog
PS1	Pan-STARRS1, Panoramic Survey Telescope and Rapid Response System
2MASS	Two Million All-Sky Survey
ADES	Astrometry Data Exchange Standard
NASA	National Aeronautics and Space Administration
MPC	Minor Planet Centre
ESA	European Space Agency
IAWN	International Asteroid Warning Network
JPL Horizon	Jet Propulsion Laboratory Horizons On-Line Ephemeris System
NEOCP	Near-Earth Object Confirmation Page
DART	Double Asteroid Redirection Test

Table 1: List of acronyms.

Preface

My far-and-beyond fascination with the universe has always underscored the relative smallness of endeavors such as this Ph.D. thesis in the grand scope of existence. However, my down-to-Earth core interest lies in the reality of our cosmic neighborhood, which led me to focus on asteroids, seemingly unassuming entities in the vast field of astronomy. The Solar System, despite its proximity, remains unknown to humanity. Thus, the contribution to this segment of science appears crucial in many aspects.

Someone once told me that I should enjoy writing this thesis because it describes my own work. Therefore, dear reader, **good luck** and enjoy.

Part I

Current state of the knowledge

Introduction

The results presented in this doctoral thesis build upon the work initiated during my master's degree and further developed under grant programs Diamond Grant no. 0062/DIA/2018/47, and PRELUDIUM no. 2022/45/N/ST9/01403 financed by the Ministry of Science and Higher Education of Poland and the National Science Center, Poland. During my master project, as detailed in the publication by [Marciniak et al. \(2018\)](#), my focus was on determining asteroid sizes based on stellar occultation data. Subsequently, my research moved toward the development of new software to reduce occultation data ([Podlewska-Gaca et al., 2020](#)). This put my focus on accurately determined orbits, which are crucial for predicting asteroid occultations. Moreover, the size determination of asteroids is important for the validation of the Yarkovsky effect. Therefore, I focused on this topic.

This motivated me to apply for the MSWiN Diamond Grant titled "Detection of the Yarkovsky effect based on precise astrometric measurements", paving the way for my subsequent involvement with the Gaia mission.

The asteroid orbit determination process typically involves analyzing data spanning more than a century of observational arc, collected using different observing techniques and tools to generate the most precise orbit possible. This endeavour extends beyond the mere assemblage of data. It requires a nuanced understanding and interpretation of both gravitational and nongravitational perturbations. Even with theoretical knowledge of these forces, modelling and detecting them is a challenging task that requires precise methodology and data, as described in [Chapter Results](#).

Asteroid astrometry

The first asteroid (1) Ceres was accidentally discovered in 1801 by the Italian astronomer Giuseppe Piazzi. It was a momentous event in astronomical history. After a few days of observations, Ceres was lost because it disappeared from visibility in the sky as it approached the Sun. It was rediscovered by the orbital calculations of Carl

Friedrich Gauss, who devised a revolutionary method to compute orbits from just three observations.

Max Wolf's introduction of photography to astronomy in 1891 marked another significant advancement, leading to a rapid increase in the number of discovered asteroids. The advent of CCD cameras in the 1990s further accelerated this trend, resulting in the discovery of more than a million asteroids to date.

All asteroid astrometric data (ground-based and satellite) are gathered in the Minor Planet Center¹. For date 13.12.2023 there are 424.7 million observations of 1 329 548 Solar System small objects, including 4598 comets. The MPC provides optical astrometry, which involves measuring the positions of objects in optical wavelengths to determine their coordinates. The typical accuracy of these observations ranges from 0.5 to 1.0 arcseconds. The MPC provides observations in the standard 80-column record (MPC 1992, 80-column format²). This format does not provide, for example, uncertainties of right ascension and declination or a reference catalog for astrometry for early observations, which consists of crucial information for accurate orbit determination.

In July 2018, the Minor Planet Center officially endorsed the Astrometry Data Exchange Standard (ADES) as the preferred format for the submission of astrometric observations. This decision was made after its ratification by the Commission 20 of the International Astronomical Union (IAU) during the General Assembly held in Hawaii, United States, in August 2015. Although both ADES and MPC1992 are currently accepted, however, the new format contains more information, e.g. random uncertainty of observation time, the correlation between uncertainties, reference catalog, number of reference stars in astrometric fit, and many others that had not been available before. ADES includes two file formats: XML (eXtensible Markup Language), which is tag-based, and PSV (Pipe-Separated Values), which are characterized by plain text with pipe symbol '|'. A more detailed description of the ADES format is available on the MPC web pages³.

MPC data also include occultation-derived astrometry marked with "E" in 80-column format. Stellar occultations by asteroids offer a distinct technique for determining the sizes and accurate positions of small bodies in the Solar System. This method utilizes

¹<https://minorplanetcenter.net>

²<https://www.minorplanetcenter.net/iau/info/OpticalObs.html>

³<https://www.minorplanetcenter.net/iau/info/ADES.html>

the phenomenon in which an asteroid passes between an observer and a star, casting a shadow on Earth. Accurately timing the star’s disappearance and reappearance allows for the precise determination of the asteroid’s size and its position in the sky. First observed in 1958 with (3) Juno, this technique has since evolved significantly, especially with the advent of the *Gaia* catalog, which provides precise astrometric measurements (Tanga and Delbo, 2007). Stellar occultations are instrumental not only in size determination (Marciniak et al., 2018), but also in refining models of asteroids (Podlewska-Gaca et al., 2020), discovering rings around planets and dwarf planets (Ortiz et al., 2017), and improving the astrometry of small Solar System bodies⁴. This method, free from physical assumption constraints, is indispensable for researching distant Trans-Neptunian Objects (TNOs), which because of their distance are hard to study using other techniques. (Magnusson et al., 1989; Millis and Dunham, 1989; Braga-Ribas et al., 2011)

Radar observations play a vital role in the orbit calculations for NEAs. Comprising round-trip time measurements in microseconds and Doppler shifts in Hz, radar data provide critical constraints in range and range-rate space, complementing conventional sky coordinate observations. This is mainly because these parameters are linked to distance and radial velocity, unlike traditional observations, which only determine positions in the sky. Therefore, radar introduces additional constraints in a dimension that is not accessible by conventional astrometry. Integration of radar data significantly reduces orbit uncertainty and improves the signal-to-noise ratio (SNR) for the A2 parameter. Radar observations are possible only for NEAs and a few Mars-crossing asteroids. To date (13.12.2023), there are 4,277 radar observations available for asteroids on ⁵. Some of the radar observations are also available in MPC.

The final group of astrometric measurements for determining asteroid orbits is derived from sky surveys. Ground-based surveys like ATLAS, PanSTARRS, Catalina, LINEAR, NEAT, Spacewatch, and LONEOS contributed significantly to this effort. In space, NEOWISE (Near-Earth Object Wide-field Infrared Survey Explorer) NASA satellite along with the earlier HIPPARCOS mission (High Precision Parallax Collecting Satellite), an ESA project, marked a significant milestone as the first space-based

⁴http://www.esa.int/Safety_Security/Planetary_Defence/Apophis_impact_ruled_out_for_the_first_time

⁵<https://ssd.jpl.nasa.gov/sb/radar.html>

survey that provided precise measurements of stellar positions, motions, and asteroid astrometry. HIPPARCOS laid the foundation for its successor, the *Gaia* mission.

Gaia, an ESA spacecraft proposed in October 1993 by Lennart Lindegren and Michael Perryman, was launched on 19 December 2013 in French Guiana by a Soyuz-STB/Fregat-MT rocket and is now orbiting the L2 Lagrangian point. As a pivotal ESA project, *Gaia*'s primary goal is to create a three-dimensional map of the Milky Way, offering unprecedented precision in tracking the positions and movements of stars. The introduction of the *Gaia* spacecraft⁶, with its ultra-precise astrometry observations, marks a significant advance in the field. The spacecraft features two mirrors, which function as independent telescopes: SM1 (preceding field of view) and SM2 (following field of view), with their usage indicated in the data in `transit_id` column. These telescopes observe two fields of view separated by a constant angle of 106.5 degrees, operating simultaneously to provide high-precision astrometry and map billions of celestial objects with remarkable accuracy. The stellar position accuracy reaches 0.01 mas, and the distance error is 1% for approximately 10 million objects, with a brightness accuracy of 0.1%. Furthermore, it provides radial velocity and composition for objects brighter than $V < 17$ mag. Its limiting magnitude is 20.5 mag, and it observes 70 million stars and makes 14,000 SSO observations per day. *Gaia* collects approximately 100 TB of raw data daily with its 106 CCDs with a total of nearly one billion pixels, the largest CCD camera sent into space to date. These data are then transmitted to Earth and processed by the *Gaia* Data Processing and Analysis Consortium (DPAC), an extensive European team of scientists and software developers. The primary responsibility of DPAC is to process the *Gaia* data to produce a thoroughly tested *Gaia* catalog. *Gaia* transmits 40 GB of data daily, collected by three large ESA ground stations (35 m). Deep Space Antenna 1 in New Norcia, Australia; Deep Space Antenna 2 in Cebreros, Spain; and Deep Space Antenna 3 in Malargue, Argentina. ⁷ (Prusti et al., 2016)

The *Gaia* spacecraft scanning law, detailed in figure 1, is a superposition of three motions designed to achieve the most uniform coverage of the sky possible. The spacecraft maintains a fixed 45-degree angle between its instrument axis and the Sun to ensure maximum parallax sensitivity. Its spin axis undergoes a slow precession around the Sun, creating overlapping sky coverage loops also for asteroids, which are primarily

⁶<https://sci.esa.int/web/gaia>

⁷<https://www.cosmos.esa.int/web/gaia>

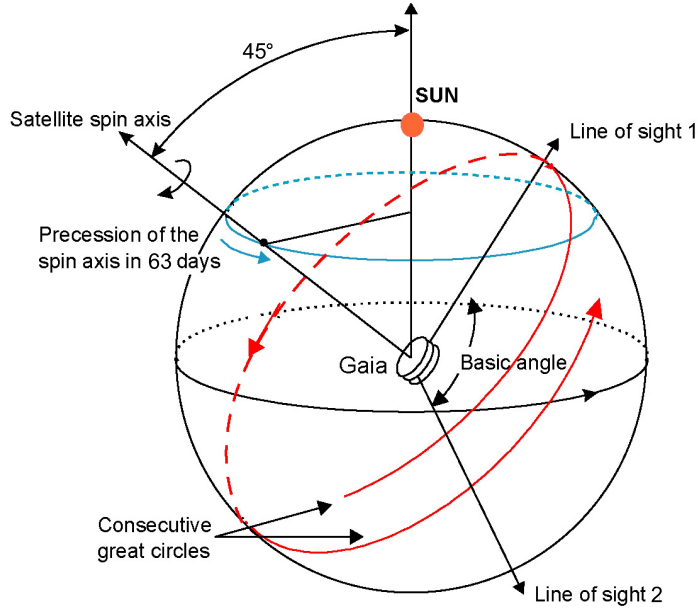


Figure 1: An image depicting Gaia’s scanning law, illustrating the movement of its spin axis and the corresponding trajectory of its observational direction (red). This image is sourced from the Gaia archive.

concentrated along the ecliptic. Areas around the solar elongation of 45 deg and 135 deg (Tanga et al., 2022) receive more frequent scans, leading to a higher density of observations in these regions, avoiding solar conjunction or opposition. Therefore, the number of observations for each object varies on the basis of its position in the sky, particularly its ecliptic latitude. The effectiveness of this scanning strategy over a 5-year period is visually shown in figure 2.

Gaia catalog includes almost 2 billion astronomical objects. Most of them are stellar objects, since this mission was dedicated to observing non-moving distant objects (Gaia et al., 2018; Vallenari et al., 2023). Gaia has also been used effectively for asteroid astrometry. The spacecraft slowly spins, scanning the sky, and objects move across its CCD camera field. The two telescopes on the spacecraft scan almost the same field 106 minutes apart. Initially, objects are analyzed in the first line of the CCD, the sky mapper, and then the astrometry field collects data only from small squares around the objects. A maximum of nine positions can be recorded for each transit. As asteroids, according to their own motion, move through the CCD camera, they may drift outside the scanning square following sidereal tracking, resulting in fewer observations per transit, especially for fast-moving objects. In particular, subsequent catalogs provide submilliarcsecond astrometry for asteroids at ~ 8 to ~ 21 mag (Tanga et al., 2022).

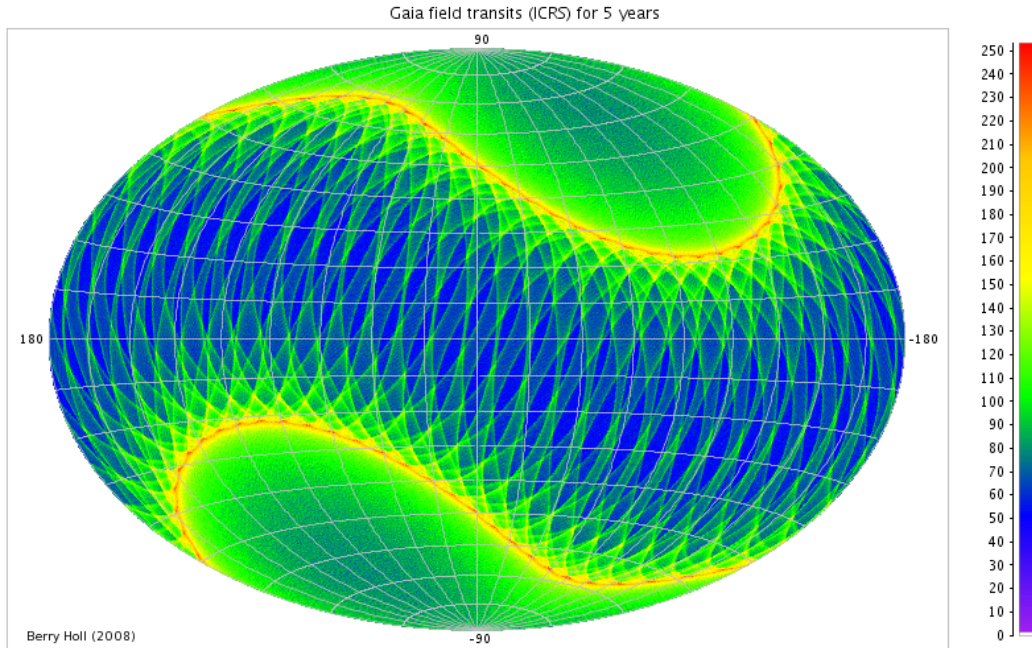


Figure 2: The number of field transits in ICRS after 5 years of *Gaia* scanning with two telescopes. The colorbar in the image indicates the frequency of scans in different areas. Copyright: Berry Holl, the *Gaia* archive.

Asteroids with the smallest astrometric errors are in the range of 10 to 18 mag (Tanga et al., 2022). Moreover, the accuracy of the *Gaia* Along-Scan (AL) direction is, on average, three times more precise than that of the Across-Scan (AC) direction. This disparity is attributed to the fact that AL data are derived from *Gaia*'s astrometric field, whereas AC information is solely sourced from the sky mapper field of the CCD. This leads to a significant correlation between right ascension (RA) and declination (DEC) in *Gaia* astrometry. This aspect, while less critical for stars, is fundamental for asteroid measurements. Astrometric uncertainties have two components, random and systematic. The systematic component is usually much smaller and is related to the altitude uncertainty of the *Gaia* satellite. It is crucial to use the entire covariance matrix, including the standard systematic error, the standard random error, and the correlation between RA and DEC, for accurate use of the *Gaia* data in the orbit determination process. The resulting uncertainty of the position given by *Gaia* is represented by a confidence ellipse as in figure 3.

The initial data release, *Gaia* DR1, was published in 2017, comprising only stellar astrometry and photometry. This catalog was used as a reference for ground-based and satellite asteroid astrometry measurements (Brown et al., 2016). Subsequent *Gaia*

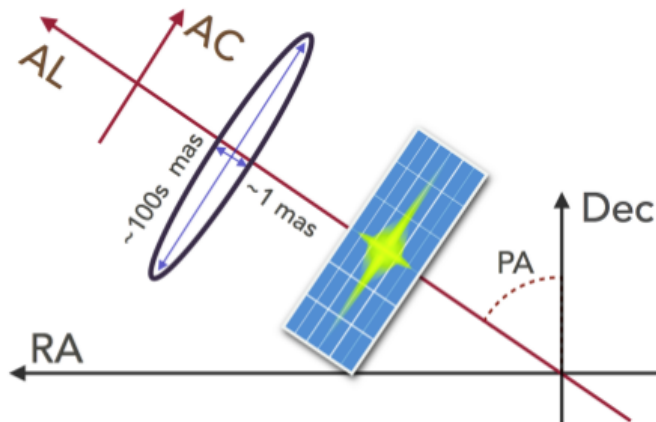


Figure 3: The significant disparity in astrometric precision along AL, achieving sub-milliarcsecond levels, compared to the AC axis, where precision is several hundred milliarcseconds. This leads to an elongated uncertainty ellipse in the AC direction, though it should not be construed as a two-dimensional Gaussian distribution. The position angle (PA) refers to the angle between the declination axis and the AC direction - included in data as `position_angle_scan`. Credit: [Spoto et al. \(2018\)](#)

releases also included extensive data on stars and more; however, this thesis focuses on asteroid data; thus, I do not mention it later. *Gaia* DR2, released in 2018, contained 22 months of observational data for 14,099 asteroids and nearly 2 million astrometric positions ([Spoto et al., 2018](#)). *Gaia* DR3, released in 2023, spanned 34 months of observations for almost 160,000 objects, with more than 23 million astrometric positions ([Tanga et al., 2022](#)), supplemented by over 60,000 asteroid spectra. The latest *Gaia* FPR, released in 2023, included the same objects (with a few exceptions) with an extended observational arc of 66 months and over 150,000 orbits for those objects ([David et al., 2023](#)). Each *Gaia* release introduces new validation techniques that improve the quality of the data. For example, although the objects in *Gaia* DR3 and *Gaia* FPR are almost identical, the astrometry (time, RA, DEC) slightly differs between these two catalogs for the same epoch of observations; therefore, now the most recent FPR data release should be used for the most accurate results. A summary of the asteroid data is presented in [table 2](#). Furthermore, due to the precise astrometric data provided by the *Gaia* mission, there is now the potential to predict asteroid occultations with greater accuracy. *Gaia*'s catalog includes precise positions even for faint stars. This improvement opens opportunities to observe asteroid shadows on Earth with increased precision, thus increasing the likelihood of successfully capturing these events.

Table 2: Summary of Gaia Data Releases.

Data Release	Release Date	Data Summary
Gaia DR1	September 14, 2016	0 asteroids
Gaia DR2	April 25, 2018	22 months of data 14,099 asteroids 1,977,702 astrometric positions
Gaia DR3	June 13, 2022	34 months of data 158,152 asteroids and planetary satellites 23,336,467 astrometric positions 60,518 reference spectra
Gaia FPR	October 10, 2023	66 months of data 156,823 asteroids 156,762 orbits 46,264,083 astrometric positions

Every day, we can observe from ten to several dozen events.⁸. The improved accuracy in predicting the path of asteroid shadows ensures that observers are less likely to miss the shadow path. All data from *Gaia* are available in the *Gaia* Archive⁹ (Salgado et al., 2017; Mora et al., 2017). The data format provided by *Gaia* is not ready to use in the generally available orbit computation software without conversion to MPC1992, ADES, or another format. The description of the *Gaia* format can be found in the *Gaia* documentation¹⁰.

The biggest of *Gaia*'s remarkable achievements is its astrometric precision, which reaches up to 10 microarcseconds. This level of precision is akin to measuring the diameter of a human hair from 1000 km away. Such precision is particularly significant for asteroid astrometry. Since the *Gaia* catalog contains a large number of stellar positions, this improves the precision of differential, ground-based asteroid astrometry itself. Moreover, *Gaia* asteroid astrometry is not restricted to large or close approaching objects, as in the case of radar data. In addition, its new data releases (DR2, DR3, and FPR) also contain SSO and more. This is crucial for NEAs since the Yarkovsky effect can only be measured for objects with precise orbits (Spoto et al., 2018; Tanga et al., 2022).

⁸<https://www.asteroidoccultation.com/>

⁹<https://gea.esac.esa.int/archive/>

¹⁰https://gea.esac.esa.int/archive/documentation/FPR/chap_datamodel/sec_dm_focused_product_release/ssoc_dm_sso_observation.html#sso_observation-source_id

Orbit determination

The theory of orbit determination begins with the "Almagest" of Ptolemy (2nd century AD), where he described the geocentric model of the Solar System, building on the ideas previously presented by other Greek philosophers, Aristotle (384–322 BC) and Eudoxus of Cnidus (c. 408–335 BC). However, Aristarchus of Samos (c. 310–230 BC) was the first to propose heliocentric theory; it is Nicolaus Copernicus (1473–1543), widely considered to be the father of this theory in the 16th century ([Copernicus, 1543](#))¹¹. An important contributor to this field was Johannes Kepler (1571–1630), who used Tycho Brahe's (1546–1601) observations of Mars to deduce the elliptical shape of its orbit and formulated his three laws of planetary motion ([Kepler, 1609](#)). Isaac Newton (1642–1727), in 1687, published 'Principia' ([Newton, 1687](#)), introducing a method for determining the orbit of a body following a parabolic path from three observations. Edmund Halley (1656–1742) applied Newton's method to establish the orbits of comets, including Halley's comet ([Halley, 1705](#)). Leonhard Euler (1707–1783), in 1744, formalized Newton's method into an analytical approach ([Euler, 1744](#)), later expanded for elliptical and hyperbolic orbits by Johann Heinrich Lambert (1728–1777). Another key figure is Carl Friedrich Gauss (1777–1855), who in 1801 made a significant contribution to the recovery of the dwarf planet Ceres using only three observations to find its six orbital elements and he derived the method of least squares ([Gauss, 1801](#)). His method is still used today for preliminary SSO orbit determination. Further advances in orbit determination methods were made by Pierre Simon, Marquis de Laplace (1749–1827). In his seminal work, 'Mécanique Céleste' ([marquis de Laplace, 1825](#)), Laplace refined and extended the principles of celestial mechanics. He provided comprehensive methods for calculating gravitational interactions and perturbations affecting planetary orbits and discovered a resonance among the moons Io, Europa, and Ganymede. His work significantly improved the precision of orbit calculations ([Plackett, 1949](#)).

Modern advancements in orbital determination continue to rely on the Least Squares Method, a robust technique pioneered by Carl Friedrich Gauss. For preliminary or-

¹¹From the author: The historical context of the geocentric model, characterized by theories like epicycles and deferents to explain the planetary movement, raises a thought-provoking question about the nature of scientific theories and makes me wonder if, as of today, there is a scientific theory that appears as an obvious statement, supported by other theories that explain and confirm it, only to be eventually proved wrong someday

bit calculations, Gibbs', Lambert's, Gauss's, or other methods are used. Its lasting relevance in the Least Squares Method is supported by the Gauss-Markov theorem (Markov, 1912), which ensures optimal estimators in linear regression models. Recent developments include Monte Carlo methods for uncertainty analysis (Milani and Gronchi, 2010). There are many other orbit determination techniques and applications such as GEM (Marsden, 1991), statistical ranging method (Virtanen et al., 2001), Markov-Chain Monte Carlo ranging (Oszkiewicz et al., 2009), MVC (Moulton-Väisälä-Cunningham) (Marsden, 1985), and more (Orlov, 1939; Kristensen, 2009; Milani, 1999; Muinonen and Bowell, 1993; Press, 1992). Moreover, the development of space-based observatories and advances in radar technology have significantly enhanced the precision and scope of observational data available for orbit determination. These advances allow for the detection of subtle effects, such as the Yarkovsky effect, that were previously unobservable.

Today's orbit determination methods have to take into account the advancements in asteroid astrometry. Modern measurements require the use of advanced software to accurately determine the orbit. These tools also need to be efficient in handling a large volume of astrometric observations. The least-squares fitting algorithm is commonly used for the determination of orbits. This technique adjusts the orbit to minimize discrepancies between observed and calculated positions of celestial objects over time, accounting for perturbations from various celestial bodies and relativistic effects. The book Milani and Gronchi (2010) is an essential resource for understanding the theoretical foundations of modern methods. Within DPAC, orbit computations are performed using the Least Squares Method and exclusively employ *Gaia* data.

In modern orbit determination, the Gauss method is initially used to estimate a preliminary orbit. This method relies on fitting a time function to a number of observations. Then the Least Squares method is employed to fit the model of an unknown function of time based on observations. The target function is nonlinear and lacks an explicit solution:

$$Q(x) = \frac{1}{m} \xi(x)^T \xi(x) \quad (1)$$

Here, $Q(\xi)$ is defined as the target function, representing the objective of the optimization process in orbit determination. This function is minimized to achieve the best fit of

modelled parameters. The vector x comprises the orbital elements, which include, the semi-major axis, eccentricity, inclination, longitude of the ascending node, argument of perihelion, mean anomaly, and an additional transverse acceleration interpreted as the Yarkovsky effect. The m parameter denotes the number of observations, indicating the size of the data set used in the orbit determination. ξ are the residuals, which are the differences between the observed values and those predicted by the current orbital model.

To address the non-linear nature of the orbit determination problem, multiple iterations are necessary. Each iteration involves a slight adjustment, with one iteration of differential correction solving a linearized least-squares problem. The iteration process is terminated on the basis of a set of criteria, based on the size of the last correction $\|\Delta x\|_C = \sqrt{\Delta x^T C \Delta x / N}$ or if the last step has not been useful for the goal of minimizing the function $|Q_{k+1} - Q_k|/Q_{k+1} \ll 1$. Where Δx is the size of the last correction, C is a normal matrix and N denotes the dimensional space of the fit parameters.

However, in this study, I used the weighted least squares problem:

$$Q(\xi) = \frac{1}{m} \xi^T W \xi = \frac{1}{m} \sum_{i=1}^m \sum_{k=1}^m w_{ik} \xi_i \xi_k \quad (2)$$

Where $W = (w_{ik})$ is the weight matrix that assigns different weights to different observations, usually based on their variance or reliability including the inverse of the covariance matrix of the observations. In this context, minimizing $Q(\xi)$ essentially involves adjusting the parameters of the orbital model so that the weighted sum of the squared residuals is as small as possible. This reflects a best-fit scenario in which the model aligns closely with the observational data.

The OrbFit, a product of international collaboration, stands as the most popular open-access software for asteroid orbit determination. Spearheaded by Andrea Milani's team at the University of Pisa, Italy, and receiving significant contributions from the Astronomical Observatory in Belgrade, E.T.S. Ingenieros Industriales at the University of Valladolid, Spain, the INAF Institute for Space Astrophysics in Rome, and JPL-Pasadena. This software is recognized for its capabilities, and through years of usage, testing, and validation, OrbFit has established itself as a reliable tool in the

astrophysical community. Specifically tailored to accommodate Gaia mission data and recommended by DPAC, OrbFit incorporates the A2 parameter as a seventh orbital element, thus improving the accuracy of orbit calculations.

The public version of OrbFit is equipped with multiple error models and weighting schemes, including vfcc17 (Vereš et al., 2017), fcct14 (Farnocchia et al., 2015), and cbm10 (Chesley et al., 2010). The vfcc17 model is adjusted for the orbit determination of newly discovered asteroids with short observational arcs.

Astrometric data, comprising observations from various observatories at different times, often include outliers and systematic errors that can significantly affect orbit determination. These outliers must be carefully removed, as only observations with substantial deviation from the predicted orbit should be excluded. OrbFit addresses this challenge through an automatic rejection procedure, as outlined in Carpino et al. (2003). This process involves the rejection and potential recovery of outlying observations based on χ^2 values derived from standard χ^2 tests. The default rejection threshold is set at $\sqrt{10}$ and $\sqrt{9.21}$ for recovery, aiming rejections at the 1% level for ideally Gaussian errors. Users have the option to disable automatic rejection to consider all available measurements in orbit determination.

OrbFit also features various specialized software:

- Fitobs (mainly used in this study): preliminary orbit computation from 3 observations, differential corrections - orbit improvement by least squares fit to the observations, with/without automatic outlier rejection, state propagation and orbital elements time series, predictions of observations, with confidence boundary, close approach analysis, with confidence boundary, identification of two sets of observations with a single object.
- Catpro: A propagator that adjusts the reference epoch of an orbit catalog to another epoch.
- Bineph: Adds perturbations from other asteroids to the dynamic model for top accuracy.
- Orbfit: preliminary orbits, differential corrections, ephemeris.
- ORBIT9: Offers long-term orbit propagation for asteroids and other SSOs, computation of Lyapunov exponents, and calculation of proper elements

The Yarkovsky effect

The orbital motion of SSOs is significantly influenced by the Yarkovsky effect ([Bottke et al., 2006](#)). The Yarkovsky effect is a non-gravitational phenomenon causing alterations in the semi-major axis of an asteroid's orbit. This effect is associated with the heating of the rotating asteroids' surfaces, followed by thermal reradiation of the energy received from the Sun. We observe the seasonal and diurnal Yarkovsky effect. The seasonal effect arises from the emission of thermal photons over the asteroid's year and consistently causes a decrease in the semimajor axis of an asteroid's orbit. The diurnal effect results from the thermal emission varying over a single asteroid day, affecting the orbit depending on the direction of asteroid rotation. For asteroids rotating in the same direction as their orbit (prograde rotation), the diurnal effect leads to an increase in the semimajor axis, whereas for retrograde rotating asteroids it results in a decrease ([Bottke et al., 2006](#)). It is presented in [figure 4](#).

Factors influencing the strength of the Yarkovsky Effect include an object's size, shape, density, rotational properties, obliquity, albedo, and composition, as well as its orbit, particularly its distance from the Sun. Smaller and less dense objects are more susceptible to this effect due to their larger surface area-to-mass ratio and smaller inertia, which make them more responsive to the subtle forces exerted by thermal radiation. The density of asteroids is one of the least known parameters. Asteroid sizes are better known and are derived from various observational methods including spacecraft flybys, adaptive optic, photometric (low accuracy) infrared (eg. NEOWISE mission), radar and occultation observations.

The Yarkovsky effect was found to be the most significant non-gravitational acceleration affecting an asteroid's orbital elements ([Chesley et al., 2014](#)). These orbital changes are extremely subtle - for an object with a 1 km diameter, the effect is estimated on the order of 10^{-4} AU/My [Greenberg et al. \(2017\)](#) and are challenging to measure. For a 0.5 km NEA, this effect could cause an orbital shift of several dozen kilometres in the semi-major axis (relative to a purely gravitational model) over a decade ([Vokrouhlický et al., 2015](#)).

The Yarkovsky effect was first postulated by Ivan Osipovich Yarkovsky in 1901 ([Yarkovsky, 1901](#)). This concept was then reintroduced and elaborated on by Ernst Julius Öpik in the 1950s ([Öpik, 1951](#)). Despite this early theoretical groundwork

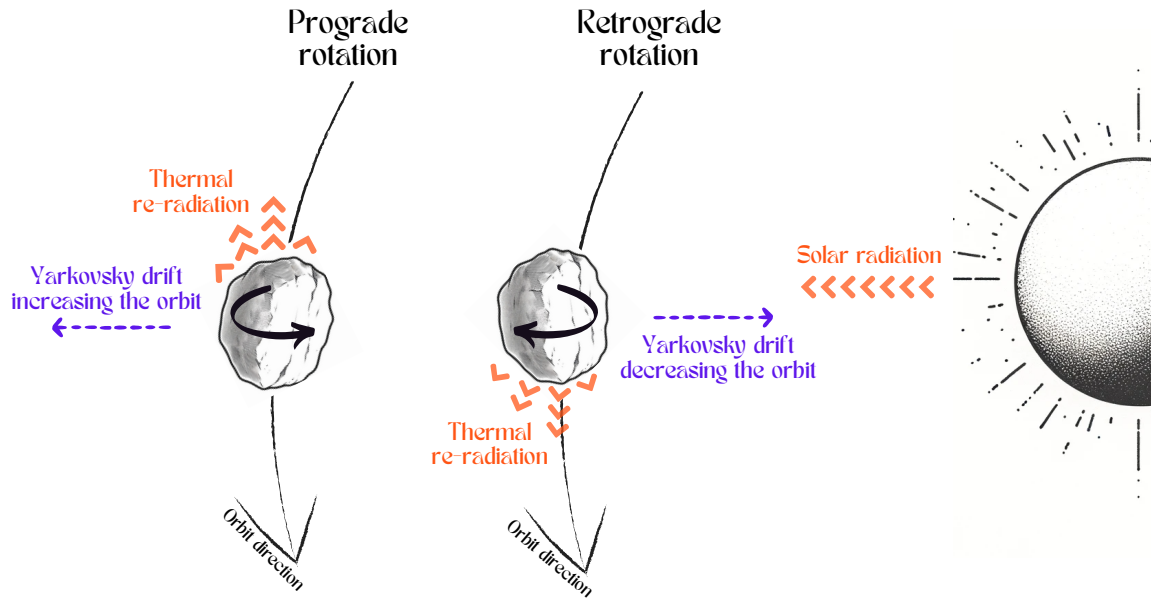


Figure 4: The diurnal Yarkovsky effect: slight orbital Drift in asteroids due to thermal radiation, with the direction dependent on whether the asteroid rotates prograde (counterclockwise) or retrograde (clockwise).

(Vokrouhlický et al., 2000; Bottke et al., 2001; Bottke Jr et al., 2000), the first direct detection of the Yarkovsky effect was achieved much later, initially for the LAGEOS satellite (Rubincam, 1988) and then for the asteroid (6489) Golevka in 2003, using Arecibo radar observations (Chesley et al., 2003). In current times, hundreds of detections have been made for NEAs (Dziadura et al., 2022; Greenberg et al., 2020; Del Vigna et al., 2018; Greenberg et al., 2017; Farnocchia et al., 2013; Nugent et al., 2012; Chesley et al., 2008; Dziadura et al., 2023; Āurech et al., 2018), however, successful direct detections for Main-Belt objects are yet to be achieved. So far it was possible only by analyzing the orbital distribution of the Karin asteroid family (Nesvorný and Bottke, 2004).

In the dynamical realm of our Solar System, though gravitational resonances serve as central mechanisms in redirecting celestial objects into varying orbits, the Yarkovsky effect presents itself as a significant player in the delivery of asteroids to those resonances and its escape from the Main Belt (Āurech et al., 2018; La Spina et al., 2004; Granvik et al., 2018). The dynamics of the Solar System exhibit relative stability, punctuated by empty zones in semi-major axes, known as Kirkwood gaps (Kirkwood, 1866). These gaps have emerged as a result of gravitational resonances with Jupiter,

and additional resonances exist with other massive planets. Gravitational forces have historically ejected asteroids from these semimajor gaps. This is an ongoing process as the subtle influence of the Yarkovsky effect can drive them into these gaps (Morbidei, 1996). The smallest asteroids are affected the most by the Yarkovsky effect, which results in a predominance of smaller objects in the NEA region (Vokrouhlicky and Farinella, 1998; Bottke et al., 2006). Moreover, this effect explains the dispersion of collisional asteroid families (Vokrouhlicky et al., 2015; Bottke, 2020), as well as the evolution of dust disks and asteroid belts in other planetary systems (Veras et al., 2015). These complex mechanisms underline the compound interaction between gravitational and non-gravitational forces in shaping the asteroid population’s distribution and its evolution in our Solar System.

The uncertainty of the semimajor axis must be several times smaller than the predicted Yarkovsky effect; therefore, precise radar observations, which provide precise position, are usually necessary to detect the effect (Del Vigna et al., 2018). Such observations are available only for asteroids approaching Earth. Moreover, the effect depends on the distance from the Sun. Near-Earth asteroids being closer to the Sun than Main-Belt asteroids (located between the orbits of Mars and Jupiter), experience larger (and more easily measurable) changes in the semi-major axis.

Furthermore, the Yarkovsky effect plays a crucial role in close approaches and impact probability predictions (Shor et al., 2012; Farnocchia et al., 2015). There are 2346 objects identified as PHAs (as of 26.07.2023). These are asteroids with orbits that allow them to make close approaches to Earth and are large enough to survive atmospheric entry during a theoretical impact. Space agencies are constantly monitoring those objects. Both NASA¹² and ESA¹³ provide lists of the most potentially dangerous asteroids and comets with a non-zero impact probability.

Potentially Hazardous Objects are of such importance to the Earth that the International Asteroid Warning Network (IAWN)¹⁴ was established in 2013. It is an international association of organizations in response to a potential threat of NEO impact. IAWN has organized NEO observation campaigns. In 2017, the target object was 2012 TC4, which passed Earth at a distance of about 50,000 km (Reddy et al., 2017). The

¹²<https://cneos.jpl.nasa.gov/sentry/>

¹³<https://neo.ssa.esa.int/risk-list>

¹⁴<https://iawn.net/>

orbit was found to be affected by the 5:3 resonance with Earth during its close approach in 2012 (Reddy et al., 2019). Then in 2019, the target of the second campaign was (66391) Moshup. It passes 5,300,000 km from Earth, and the main focus of this campaign was its physical characterization (Reddy et al., 2022b). In 2020-2021, another close-approaching and targeted asteroid was (99942) Apophis (Reddy et al., 2022a). Apophis was on the top of the risk lists for about 17 years (Chesley, 2005). Due to new radar observations and more accurate determination of the Yarkovsky effect (Pérez-Hernández and Benet, 2022), the impact could now be ruled out (at least for the next 100 years)¹⁵. The most recent IAWN campaign in 2021 focused on asteroid 2019 XS, emphasizing the statistical analysis of the quality of the astrometry and data treatment (Farnocchia et al., 2022). The observation campaigns organized by IAWN, which focus on a variety of NEOs and tackle different scientific objectives, highlight the critical role of ongoing astrometric research and data analysis in mitigating potential asteroid threats to Earth. Furthermore, in response to NEOCP¹⁶, list of newly discovered and yet unconfirmed NEOs by MPC, NASA established Scout¹⁷. This software provides orbital analysis and hazard assessment for these newly identified objects. It led to the detection of a few small asteroids (e.g., 2022 WJ1, 2023 CX1) just hours before their impact.

There are two scales used to assess the potential risk of an impact: the Torino scale (Morrison et al., 2004) and its more comprehensive counterpart, the Palermo scale (Chesley et al., 2002). The Palermo scale takes into account the risk of impact, the energy of the impact, and the time remaining until the event, which are all presented as a single number. Based on these scales, the risk analysis is translated into a numerical value which subsequently determines which asteroids are selected for observation and study. This was the case with Apophis, as mentioned before. Currently, the most significant threat is posed by the Bennu asteroid (101955), with a Palermo scale rating of -1.41 (as of 26.07.2023). This is why it was the target of the Osiris-Rex space mission (Goossens et al., 2021) and is now the best-studied asteroid (Chesley et al., 2014; Goossens et al., 2021). Furthermore, the DART mission is another significant initiative that aims to mitigate potential threats from asteroids by demonstrating the kinetic effects of crashing a spacecraft into an asteroid (Cheng et al., 2023).

¹⁵http://www.esa.int/Safety_Security/Planetary_Defence/Apophis_impact_ruled_out_for_the_first_time

¹⁶https://www.minorplanetcenter.net/iau/NEO_dev/toconfirm_tabular.html

¹⁷<https://cneos.jpl.nasa.gov/scout/#/>

In conclusion, larger asteroids that could potentially destroy Earth have already been identified. It is crucial that we continuously monitor their orbits, which are constantly perturbed by gravitational and non-gravitational forces, and their physical properties in order to be prepared for close approaches and possible impacts. However, smaller objects could still pose a significant threat with their ability to obliterate a city or cause a tsunami. They often remain undetected due to their small brightness. They are typically only discovered during close Earth approaches, which could be too late to prevent an impact. For this reason, studying the Yarkovsky effect is of paramount importance. It aids our understanding of the entire asteroid population.

Part II

Scientific goals and results

Research goals

The *Gaia* space mission is revolutionary in its approach and serves a dual purpose in determining multiple physical and dynamical properties of asteroids. On one hand, it delivers astrometric and photometric measurements with unprecedented precision and accuracy requiring new approaches to effectively leverage these data alongside the considerably less accurate ground-based data. On the other hand, *Gaia* improves our ability to determine multiple properties of asteroids through ground-based observations. Specifically, the enhanced precision provided by the *Gaia* mission has led to an increase in the number of accurately predicted asteroid occultations. This advancement permits more frequent and reliable ground-based observations of these events.

The main objective of this thesis was to determine the properties of asteroids observed by the *Gaia* mission from ground- and space-based data. In particular to:

1. Determine asteroid sizes for selected *Gaia* mass asteroids,
2. Determine the Yarkovsky effect by properly incorporating the highly correlated *Gaia* DR2 astrometry,
3. Determine the Yarkovsky effect using *Gaia* DR3 and a new weighting scheme.

Results

In the course of my Ph.D. research, I have contributed to three significant papers that encapsulate the core findings of my studies over the past few years. The following is a detailed description of each publication, highlighting their objectives, methodologies, and contributions to the field.

Determine asteroid sizes for selected *Gaia* mass asteroids

Occultations, traditionally used for refining orbital predictions, serve a dual purpose in my research by also enabling the determination of asteroid sizes and shapes and providing its accurate astrometric positions. These parameters are crucial for understanding the Yarkovsky effect, as the thermal properties and surface area of an asteroid directly influence its force. By analyzing occultation data, we can derive expected values of asteroid sizes or even shapes, which, when combined with density estimates, improve our understanding of asteroid mass and composition. This approach leverages the developed software, to integrate occultation data more effectively. The software's evolution represents an advancement in utilizing occultations.

The program now incorporates all uncertainties involved in the reduction of occultation data, including the observer's location, timing of the observations, and the right ascension (RA) and declination (Dec) of the star. This upgrade marks an improvement over its predecessor, allowing for more accurate and reliable size estimations with its uncertainty. The program, initially based on an older version, has been partially automated and continues to be used at the University for the occultation data. Its operation begins by determining the edges of the asteroid's shape from images obtained from ISAM ¹⁸. It then calculates the parameter related to the direction of a line parallel to the segments of the occultations. The program proceeds to determine the positional parameter for the line that passes through two points of a selected occultation event. Later it computes the intersection points of this line with the edges of the shape

¹⁸<http://isam.astro.amu.edu.pl/>

and determines the minimization parameter as the sum of distances from the edge point and observation to the error range points of individual occultations (RMSD). After calculating the size error of the scale-RMSD distribution function, the result is normalized to the longest radius of the model. The output includes the maximum radius of the model (R), the coordinates corresponding to individual observations, the uncertainty coordinates, the maximum radius of the asteroid, its uncertainty value and RMSD. The code can fit both spherical and more complex models if such data are available.

The paper [Podlewska-Gaca et al. \(2020\)](#) refers to the determination of the physical parameters of 13 main belt asteroids using the SAGE algorithm and combining it with thermophysical models and occultation data. Occultations were used to scale the shape models of these asteroids and confirm the main shape features. In the future aiding in precise density calculations when combined with mass from Gaia. Accurate estimation of the theoretical value of the Yarkovsky effect is feasible primarily for asteroids that are well-modelled. Occultation data are vital in this context, as they provide insights into the spin-axis orientation and size of the asteroids, both of which are critical parameters for predicting the expected Yarkovsky effect.

Determine the Yarkovsky effect by properly incorporating the highly correlated *Gaia* DR2 astrometry

Although designed to map the Milky Way, the *Gaia* mission influences all branches of astronomy, including the science of the Solar System. *Gaia* asteroid observations, have different accuracy in the Along-Scan (AL) and Across-Scan (AC) directions, with the AL direction exhibiting superior precision at the submilliarcsecond level, in contrast to the AC direction, where accuracy is considerably lower, up to approximately one arcsecond. This extreme astrometric accuracy and the high correlation inherent in *Gaia* observations require a new approach to the computation of asteroid orbits.

In [Dziadura et al. \(2022\)](#) I investigated the Yarkovsky effect, using *Gaia* DR2 astrometry. The article explores the potential of *Gaia* DR2 in detecting and estimating the

Yarkovsky effect in asteroids identified as promising candidates before the launch of *Gaia*.

Significant emphasis was placed on using the data *Gaia* together with its complete covariance matrix, including the high correlation between the RA and Dec components. This aspect is particularly important compared to typical ground-based observations, which are generally treated as uncorrelated and assumed Gaussian. The study specifically targeted 42 asteroids identified as promising candidates for the Yarkovsky effect by [Mouret and Mignard \(2011\)](#), all of which had corresponding observations in the release of *Gaia* DR2. For these asteroids, the empirical A2 parameter was meticulously estimated and its reliability was thoroughly evaluated.

Throughout my Ph.D. research, I used various versions of OrbFit (5.0.5, 5.0.6 for tests and ephemeride comparison methods, 5.0.7 to incorporate *Gaia* data in ADES format, and the latest version featuring a new weighting scheme. Before my visit to MPC (described in the next section), I mainly used the fcct14 weighting scheme ([Farnocchia et al., 2015](#)), which was then the most suitable for my calculations. Before using OrbFit for my research, I performed test with well-studied objects such as (6489) Golevka, (101955) Bennu, (2063) Bacchus, and others to thoroughly understand all aspects of the software. The long least squares of the software and extensive verification make it a reliable foundation for my work.

The core of my methodology for determining asteroid orbits hinges on the least-squares method and differential corrections. This approach allows for the refinement of initial orbit estimations by iteratively minimizing the residuals between observed and calculated positions. My implementation focuses on improving the precision of these calculations, particularly by incorporating the high-quality data provided by the *Gaia* mission.

My research used all available data sources: *Gaia* DR2 catalog data, complemented by optical radar data from the MPC and JPL databases. A crucial aspect of this process involved my development of custom code to convert *Gaia* data into the ADES format. This conversion was critical for the integration of various data types. I determined the geocentric position of *Gaia*, as required by OrbFit, from its barycentric coordinates using the DR2 database. Previously, I relied on downloading *Gaia*'s geocentric positions from JPL Horizon as necessitated by OrbFit version 5.0.7. However, the JPL Horizon predictions did not account for engine burns and orbital adjustments, leading

to potential inaccuracies. By directly computing the geocentric position of Gaia using its Barycentric coordinates from DR2 and Earth’s position from JPL, I significantly improved the accuracy of my results. Furthermore, I adhered to the JPL ephemeris DE441 version, which is recommended for Gaia data. I have also adopted an approach that includes both systematic and random uncertainties in my calculations. Observation covariance (rmsra, rmsdec, rmscorr) is computed from the sum of random and systematic covariance matrices. Although random uncertainties are typically larger, accounting for systematic ones is crucial, especially in detecting subtle phenomena such as the Yarkovsky effect. I used Gaia data with more decimal numbers for observational time (e-6 s) and position (e-12 AU).

In previous studies [Fedorets et al. \(2018\)](#); [Hanuš et al. \(2018\)](#) the number of observations in each transit was transformed to a single so-called normal point, while here I use all observations. To critically evaluate my methodology, I determined the Yarkovsky effect for all objects in this work, comparing the use of a single observation from each transit versus employing all observations. The results, presented in [Dziadura et al. \(2022\)](#) in Table 7, indicate that there are no significant discrepancies in the A2 and SNR values between the two methods. These findings and the methodology are explained further in the Results section, which showcases the robustness and reliability of our long-term data processing approach.

Integration of the *Gaia* DR2 data significantly improved the SNR of the detection of the Yarkovsky effect. Reliable detection (SNR > 3) of the Yarkovsky effect (A2) was found for 12 asteroids. The results suggest that the Yarkovsky drift detection potential of the *Gaia* data is substantial, as exemplified by asteroids such as (66391) Moshup, where the SNR improved more than 5 times after including DR2. Additionally, the study highlighted the correlation between the rotational direction and the Yarkovsky effect, with most detected objects being retrograde rotators.

The study compared empirical estimations of the Yarkovsky effect with expected values based on the physical and orbital properties of the objects studied. Various models were used for comparison, including the works of [Greenberg et al. \(2020\)](#) and [Del Vigna et al. \(2018\)](#). The study found consistency between the empirical and expected values in most cases, validating the effectiveness of *Gaia* DR2 to improve the detection of the Yarkovsky effect.

The article concludes that *Gaia* DR2 astrometry significantly improves the detection

and estimation of the Yarkovsky effect in asteroids. The findings of this study are instrumental in deepening our understanding of the dynamical evolution of asteroids, highlighting the promising potential of future *Gaia* data releases in this area of research. Furthermore, the importance of utilizing the entire covariance matrix of *Gaia*, which encompasses systematic and random uncertainties along with their correlations, is emphasized.

Determine the Yarkovsky effect using *Gaia* DR3 and a new weighting scheme

The data from *Gaia* DR3 are considerably more precise than ground-based observations, exhibiting a level of accuracy that is significantly higher. Given the stark contrast in precision and accuracy between these sets of data, it is important to use an appropriate weighting model to integrate them effectively. This model must account for the differing orders of magnitude in precision and ensure that each observation is proportionately influential in the overall analysis. This advanced weighting model has been used in my third publication ([Dziadura et al., 2023](#)), where its application was instrumental in enhancing the results.

During my Ph.D. studies, I entered into a collaboration with Dr Federica Spoto, codeveloper of OrbFit and an expert in orbit determination. In 2022 I went for a research visit to the Minor Planet Center (MPC), and we collaborated on developing an innovative weighting scheme. My primary role involved rigorous testing the latest version. A paper detailing this advanced weighting model is currently in preparation [Spoto et al. in prep. \(2024\)](#) as an evolution of the error model originally proposed by [Farnocchia et al. \(2015\)](#), and this updated approach yields more precisely defined weights for each observation. Although this weighting model was implemented in [Dziadura et al. \(2023\)](#), it was not thoroughly explained. Thus, I describe the model in detail below.

To derive the scheme, all astrometric observations and their residuals were downloaded from the MPC database. Then they were categorically divided into 49,727 groups based on the year of observation, the observatory code, the apparent magnitude, the type of observation, and the stellar catalog used for the reduction. For each group, the

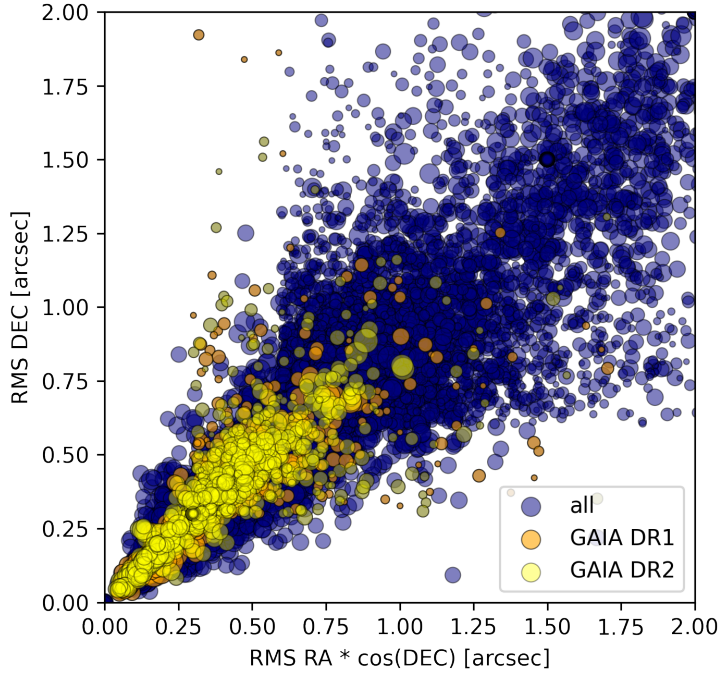


Figure 5: RMS in $RA * \cos(DEC)$ and DEC for all astrometric measurements in MPC (dark blue). Observations reduced with *Gaia* DR1 are indicated in orange, and those reduced with *Gaia* DR2 are shown in yellow. The size of the points in the figure is proportional to the number of observations within each group, displayed on a logarithmic scale.

mean astrometric residuals were determined, which were subsequently converted into RMS values in RA and DEC. These weight values matrix (W as in Equation 2) were then utilized as weights for each observation in the orbit computation process. The distribution of these weight groups is illustrated in figure 5, where the size of the point indicates the logarithm of the number of observations in each group. In particular, two stellar catalogs that were used for the astrometry reduction, *Gaia* DR1 and *Gaia* DR2, were marked in yellow and orange. The RMS values were markedly smaller for objects reduced with these catalogs, with the largest values being approximately 17 arcsecs for DEC and 12 arcsecs for $RA * \cos(DEC)$.

An example of this is shown in figure 6, which features two observatories of the ATLAS robotic astronomical survey, namely Mauna Loa and Haleakala. This survey primarily targets NEAs and contributes significantly to considerable amounts of asteroid astrometry. This particular comparison effectively demonstrates the advances in astrometric

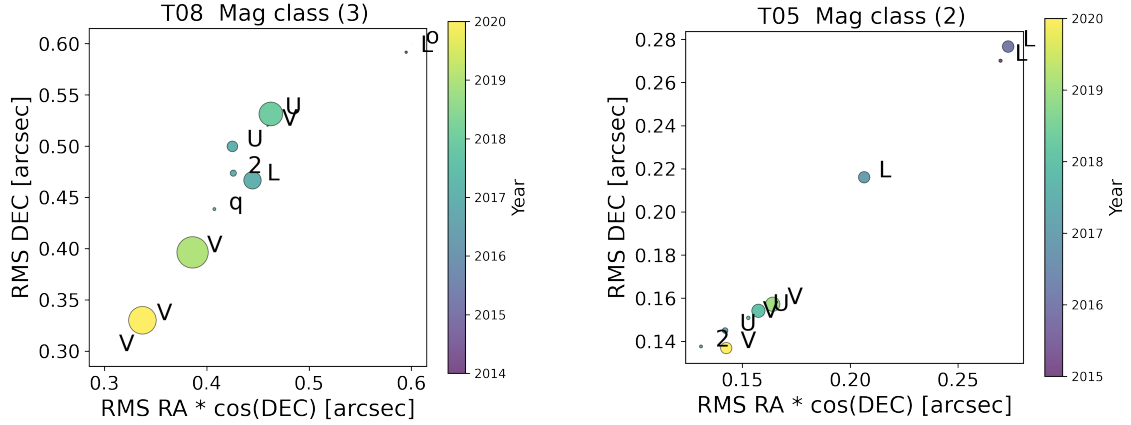


Figure 6: RMS in RA * cos(DEC) and DEC for two observatories (T08, T05) across two magnitude classes (3, 2), with specific catalogs used for reduction indicated: U - *Gaia* DR1, V - *Gaia* DR2, q - UCAC-4, 2 - PS1-DR2, L - 2MASS. T08 denotes the ATLAS-MLO at Mauna Loa Observatory and T05 denotes the ATLAS-HKO at Haleakala Observatory. The colorbar in the figure represents the year of the observations. The size of the points in the figure is proportional to the number of observations within each group.

reduction achieved through the adoption of the latest *Gaia* catalog, in contrast to the earlier reliance on the 2MASS catalog in 2015, at the beginning of the ATLAS survey. In particular, the smallest residuals are observed in the data processed with *Gaia* DR2. These plots are categorized into two magnitude classes, and the size of the point linearly represents the number of observations per group.

An additional layer of analysis is presented in [figure 7](#), RMS values for all catalogs are plotted across six magnitude classes. This plot is particularly insightful, as it highlights a notable predominance of asteroids in magnitude classes 3 and 4. Consequently, the trends and patterns observed within these classes are likely to be more representative of the broader asteroid population’s behaviours and characteristics. It is important to note that the axes in [figure 7](#), which encompass data from all catalogs, are broader compared to those in [figure 6](#), which are limited to observations reduced using the *Gaia* stellar catalog. This shows that using the *Gaia* stellar catalog for reduction improves ground-based and satellite asteroid astrometry.

To further demonstrate the improvement in astrometric residuals after applying the new weighting scheme in orbit determination, [figure 8](#) displays post-fit residuals for five different asteroids. Comparison between the two weighting schemes shows that the covariance confidence ellipse was considerably more constrained when employing the

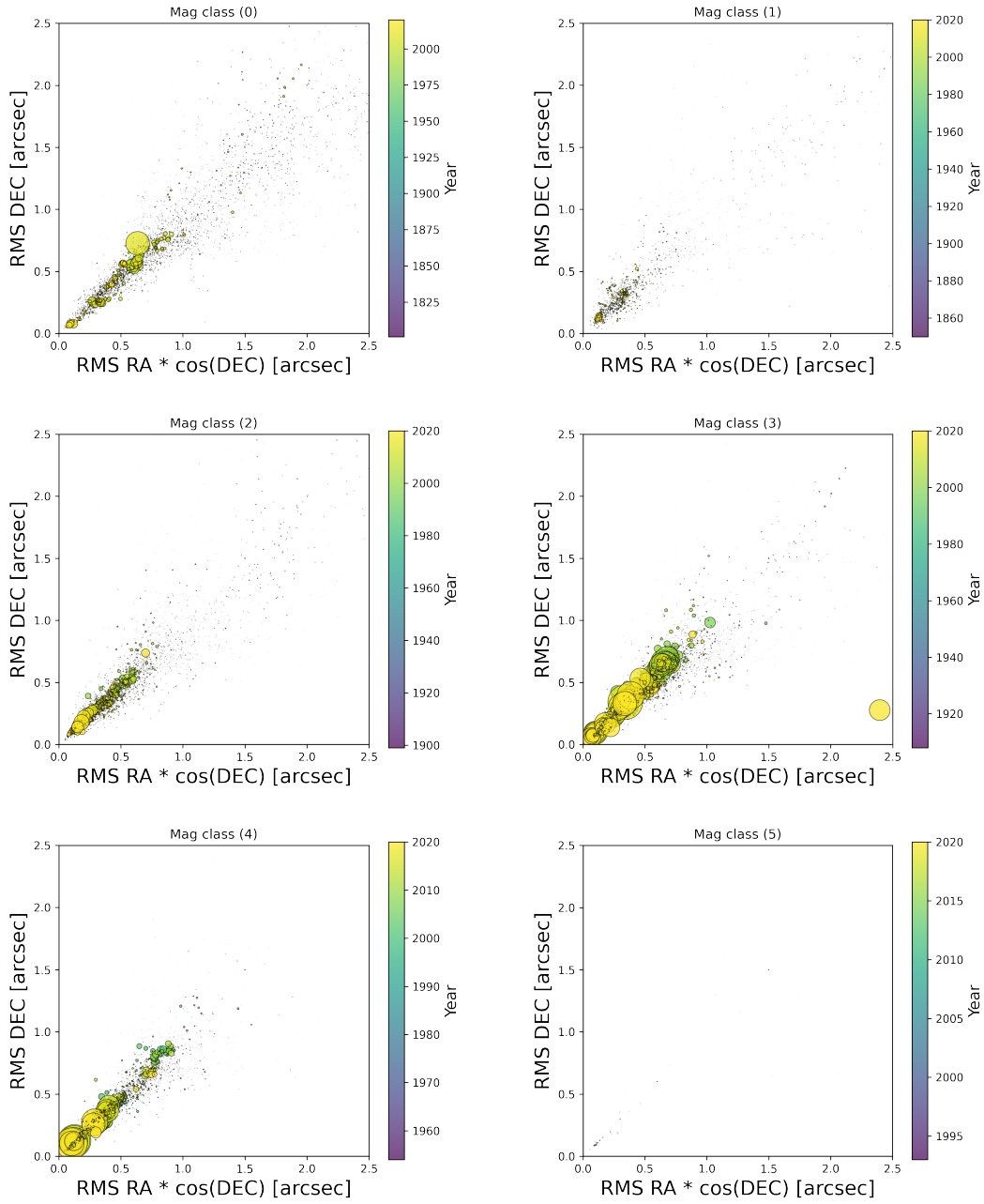


Figure 7: Residuals for all catalogs for different magnitude class. The color bar in the figure represents the year of observations.

new weighting scheme [Spoto et al. in prep. \(2024\)](#). For the asteroid (99942) Apophis, I observed two concentrated groups of astrometric observations, outside the confidence ellipses. The left group of observations originates from the 2021 observing campaign conducted by P66 - Deokheung Optical Astronomy Observatory, timed with the asteroid's close approach. The right group corresponds to another set of observations from the 2021 campaign by the Assah Observatory. The notable divergence in these observations is likely to be attributed to systematic errors inherent in these two observatories.

My final analysis involved comparing the performance of the new weighting scheme with the A2 values from JPL presented in [figure 9](#). Here, the parameter S was calculated as $S = A2_{empirical}/A2_{expected}$, where $A2_{empirical}$ is the empirical value derived from the orbital adjustment and $A2_{expected}$ is the predicted value based on the physical and orbital characteristics of the objects (see details in publications 2 and 3). The JPL A2 values are determined using manual interventions in the weighting and rejection of astrometric observations, in contrast to the automated approach of this study. Close alignment of these results signifies the efficacy of the new automatic version.

While the inclusion of this comprehensive weighting scheme extends the time required for orbit determination, the trade-off substantially increases the precision and reliability of the results. This slight delay is a justified compromise, considering the enhanced accuracy it brings to the orbital parameters of asteroids, especially in high-stakes scenarios such as predicting potential Earth impacts.

This scheme was used in [Dziadura et al. \(2023\)](#). The study's primary aim is to utilize *Gaia* DR3 asteroid astrometry to detect the Yarkovsky effect, a non-gravitational transverse acceleration (NGTA). The paper also focuses on computing the bulk densities for asteroids where the Yarkovsky effect is considered detected and robust.

I used the new version of OrbFit software, which is the recommended tool for orbit determination, particularly when working with data from the *Gaia* mission. This necessitates a nuanced understanding of the data's covariance and the proper weighting of observations, a challenge adeptly handled by my modifications to the methodology. My research utilizes a version developed in collaboration with the Minor Planet Center (MPC), tailored for the high-quality astrometry that *Gaia* offers. This version is not only optimized for current *Gaia* data but is also being prepared for future integration with data from the Vera C. Rubin Observatory.

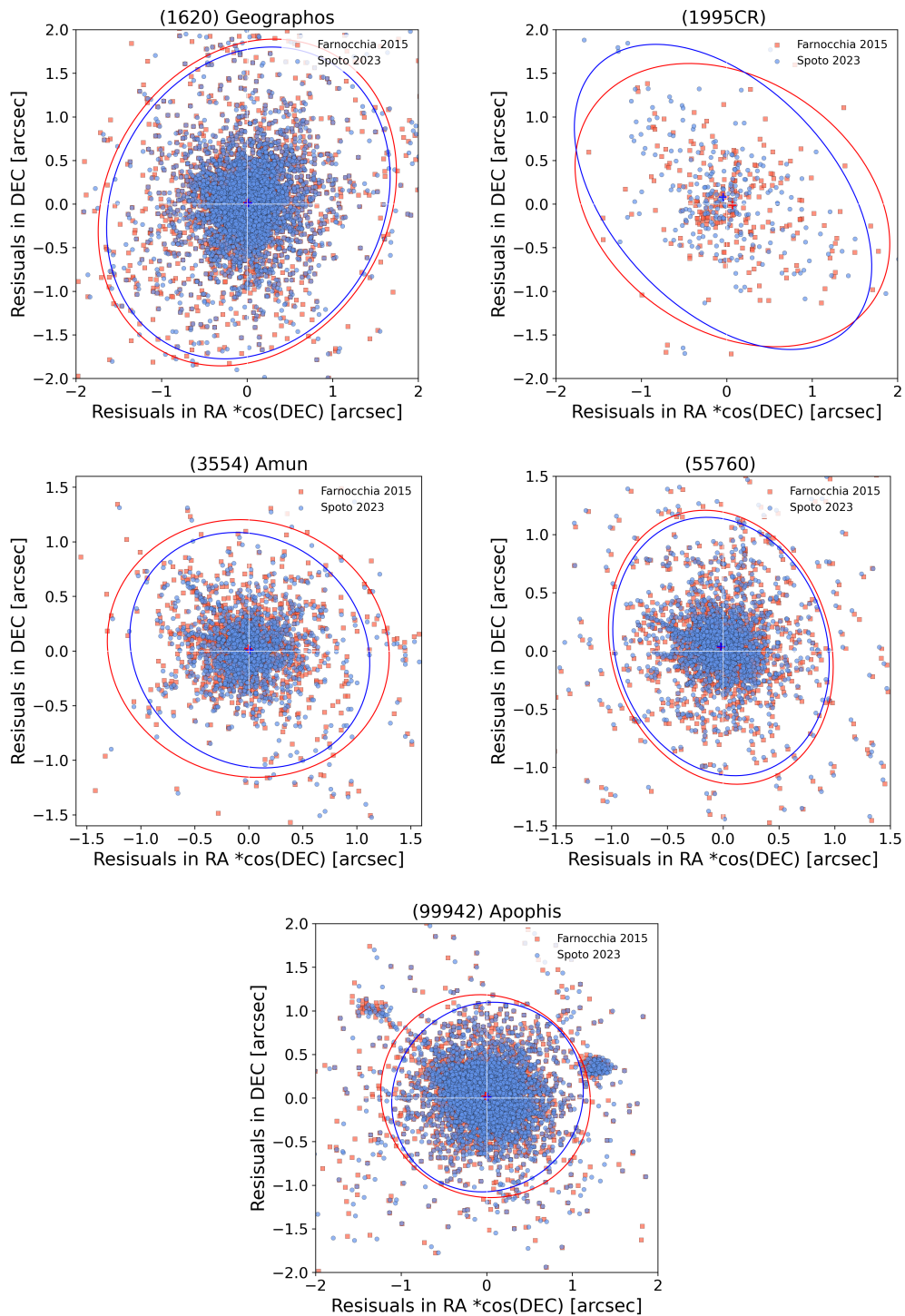


Figure 8: Observations residuals of (1620) Geographos, 1995 CR, (3554) Amun, (55760), (99942) Apophis in RA and DEC. The red squares represent the residuals when using the [Farnocchia et al. \(2015\)](#) weighing model to determine the orbit, and the red cross is the mean value. Blue dots are the residuals when using the new [Spoto et al. in prep. \(2024\)](#) weighing model, and the blue cross is its mean value. The red and blue ellipses are the covariance confidence ellipses of all data points of the residuals [Farnocchia et al. \(2015\)](#) and [Spoto et al. in prep. \(2024\)](#), respectively.

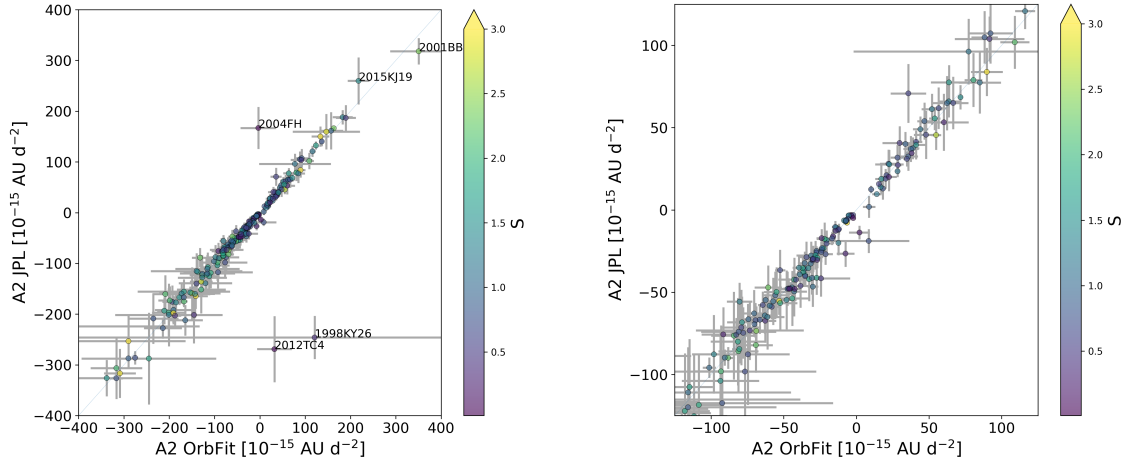


Figure 9: Comparison of the A2 parameter computed in this study using OrbFit, employing the new weighting scheme, with manually reduced results from JPL. Values deviating significantly from the fit are indicated. The S-value is computed for OrbFit values. The right panel provides a magnified view.

The study encompassed 446 Near-Earth Asteroids (NEAs) and 54,094 Inner Main Belt Asteroids (IMBAs), along with Mars Crossing asteroids. A new validation method was employed, involving the computation of the Yarkovsky effect using different observational arcs to observe the result stability.

Integration of the *Gaia* DR3 data significantly constrained orbital uncertainties, improved SNR and allowed a reliable determination of A2 values for 49 NEAs. Although substantial advances were made in the analysis of IMBAs, the study did not detect the Yarkovsky drift for any main belt asteroid. The paper highlights the effectiveness of adding *Gaia* DR3 data to improve orbit determination and the detectability of non-gravitational parameters.

The study concludes that the addition of a small amount of ultra-precise astrometry from *Gaia* DR3 significantly improves the determination of the orbit of the asteroid and enhances the detectability of non-gravitational parameters. The results are promising for the upcoming *Gaia* DR4 release, anticipating more detections for NEAs and the first new detection for IMBAs. This improvement has far-reaching implications for understanding the dynamical evolution and physical properties of asteroids.

The research underlines the importance of the Yarkovsky effect in asteroid dynamics and its potential for determining asteroid densities. The precision of the *Gaia* data combined with advanced computational techniques presents a powerful tool for future

asteroid studies. The upcoming *Gaia* releases are expected to bring even more clarity to the field, enhancing our understanding of asteroid populations and their potential impact risks.

This study represents the first of its kind in terms of its extensive scope, which covers such a large number of objects, while also including the determination of densities and incorporating data from the *Gaia* space mission. Until now, the *Gaia* data have been used either separately or for small group objects. However, this research marks the first instance in which *Gaia* DR3, combined with ground-based and satellite observations from the MPC, as well as radar data from JPL, is utilized comprehensively for calculations.

Summary and future prospects

In this thesis, specific objectives were established aimed at advancing the knowledge of the properties of asteroids observed by *Gaia*, particularly by focusing on the study of asteroid sizes, densities, orbits and the Yarkovsky effect. The main goal has been achieved successfully, including the detection of the Yarkovsky effect among *Gaia* target asteroids. The implementation of new size determination software from occultation data, advanced versions of OrbFit and a new weighting scheme was instrumental in this study. The integration of *Gaia* data with radar, satellite and ground-based observations from MPC significantly improved the accuracy of orbit determination.

Throughout this research, data from the latest *Gaia* catalogs have been integrated and analyzed. The findings and methodologies have been compiled and published in *Astronomy & Astrophysics (A&A)* and *Icarus*, underscoring the importance of continuous data integration and analysis from emerging catalogs.

Since the methodology and software are ready for the *Gaia* data, I have also recently repeated the computation for NEAs using the newest FPR catalog. This work has already been done and submitted to *Astronomy & Astrophysics* ([Dziadura et al., 2024](#)).

The next step in the field of ultra-precise astrometry is to consider photocenter-barycenter offset, a disparity between the observed position and the actual center of mass of an asteroid, impacting its astrometry. Initial results indicate the detectability of this offset in *Gaia* data, which offers a promising direction for precise orbit determination. Recognising the importance of this factor, a PRELUDIUM grant to investigate and model these offsets titled "Improving Orbits of Potentially Hazardous Asteroids" has been successfully obtained. This project delves into the nuances of the photocenter-barycenter effect, examining its variation with asteroid size, shape, distance, and phase angle. Recent advances allow for its detection, thereby refining asteroid orbit determinations significantly, impacting up to 10-20% of the asteroid's apparent diameter. By simulating asteroid images to measure this offset, and applying corrections to *Gaia* DR3 data, we significantly enhanced orbit determinations. Future work will expand on the preliminary findings, exploring the impact of this offset across various asteroid types

and observing conditions, potentially leading to more refined models and predictions for asteroid orbits ([Dziadura et al in prep.](#)).

Looking ahead, the Minor Planet Center is planning to incorporate data from the upcoming Vera C. Rubin telescope. This observatory is equipped with a wide-field camera poised to capture the entire available sky every few nights, potentially discovering around 5 million asteroids, a significant increase from the current approximately 1.3 million known asteroids. The influx of data from the Rubin telescope will enrich the MPC database. Moreover, with the asteroid sizes and masses determined by the Gaia mission, future density calculations will become feasible. The size of an asteroid also affects the photometric center, which will be more accurately determined with the enhanced observational data. This integration underscores the continuous evolution and enhancement of astrometric techniques and resources, marking a new era in the field.

Acknowledgement

I want to express my profound gratitude to my supervisors, Prof. UAM Dr Hab. Przemysław Bartczak and Dr Dagmara Oszkiewicz, for their invaluable guidance, jokes, consistent support, and for teaching me to always look for solutions, not problems that have transformed my approach not only to this research but also to my personal life. Their wisdom and insightful critiques have pushed me to finish my Ph.D. thesis, which was one of the hardest paths in my life.

I am also profoundly thankful to Adam Mickiewicz University in Poznań, especially the Astronomical Observatory Institute, for providing an intellectually stimulating environment and numerous opportunities for research travel. My heartfelt thanks go to Prof. UAM Agnieszka Kryszczyńska, the Director of the Astronomical Observatory Institute, for her empowering leadership and enthusiastic encouragement. I also extend my gratitude to the dedicated staff at the Astronomical Observatory Institute for their significant help in the settlement of my research trips. Moreover, I thank all international collaborators, especially Dr Federica Spoto, who supported my struggle with OrbFit software.

Most importantly, I extend my deepest gratitude to my family and close friends for their unwavering support during the most challenging times. Their immense encouragement and belief in me were crucial in navigating through the darker moments, and without their support, achieving this much would not have been possible.

This work has received funding from the National Science Centre, Poland, in the years 2022/2023, as a research project under PRELUDIUM, grant number 2022/45/N/ST9/01403, and from the Ministry of Science and Higher Education of Poland in the years 2018/2021, as a research project under the "Diamond Grant" program, grant number 0062/DIA/2018/47, and the Polish National Agency for Academic Exchange in the years 2022/2023, as a research project under the NAWA: Polonium – bilateral exchange between Poland and France program, grant number BPN/BFR/2021/1/00026/U/00001, and IDUB 021/13/UAM/0042, and IDUB 071/06/POB4/0029, and IDUB 080/13/UAM/0057. I was awarded a stipend for Ph.D. students by the Adam Mickiewicz University Foundation.

This work has used data from the European Space Agency (ESA) mission *Gaia*¹⁹ and was possible thanks to open source OrbFit software²⁰. This research has used data and/or services provided by the International Astronomical Union Minor Planet Center, the JPL Horizons On-Line Ephemeris System, and the *Gaia* collaboration. I thank all observers who submitted data to the Minor Planet Center.

Language corrections and enhancement of the manuscript's readability were facilitated by the use of artificial intelligence, specifically Writefull for Overleaf and ChatGPT.

¹⁹<https://www.cosmos.esa.int/gaia>

²⁰<http://adams.dm.unipi.it/orbfit/>

Bibliography

- Bottke, W. F. (2020). The evolution of small body populations: From planet migration to thermal drift forces.
- Bottke, W. F., Vokrouhlický, D., Broz, M., Nesvorný, D., and Morbidelli, A. (2001). Dynamical Spreading of Asteroid Families by the Yarkovsky Effect. *Science*, 294(5547):1693–1696.
- Bottke, W. F., Vokrouhlický, D., Rubincam, D. P., and Nesvorný, D. (2006). The yarkovsky and yorp effects: Implications for asteroid dynamics. *Annu. Rev. Earth Planet. Sci.*, 34:157–191.
- Bottke Jr, W. F., Rubincam, D. P., and Burns, J. A. (2000). Dynamical evolution of main belt meteoroids: Numerical simulations incorporating planetary perturbations and yarkovsky thermal forces. *Icarus*, 145(2):301–331.
- Braga-Ribas, F., Sicardy, B., Colas, F., Lecacheux, J., Maury, A., Ortiz, J. L., Morales, N., de, I., Jehin, E., Manfroid, J., Gillon, M., Assafin, M., Vieira-Martins, R., Camargo, J. I. B., and Harlinton, C. (2011). Stellar Occultation by Transneptunian Object (208996) 2003 AZ84. *Central Bureau Electronic Telegrams*, 2675.
- Brown, A. G., Vallenari, A., Prusti, T., De Bruijne, J., Mignard, F., Drimmel, R., Babusiaux, C., Bailer-Jones, C., Bastian, U., Biermann, M., et al. (2016). Gaia data release 1-summary of the astrometric, photometric, and survey properties. *Astronomy & Astrophysics*, 595:A2.
- Carpino, M., Milani, A., and Chesley, S. R. (2003). Error statistics of asteroid optical astrometric observations. *Icarus*, 166(2):248–270.
- Cheng, A. F., Agrusa, H. F., Barbee, B. W., Meyer, A. J., Farnham, T. L., Raducan, S. D., Richardson, D. C., Dotto, E., Zinzi, A., Della Corte, V., et al. (2023). Momentum transfer from the dart mission kinetic impact on asteroid dimorphos. *Nature*, 616(7957):457–460.
- Chesley, S., Vokrouhlický, D., Ostro, S., Benner, L., Margot, J., Matson, R., Nolan, M., and Shepard, M. (2008). Direct estimation of yarkovsky accelerations on near-earth asteroids. *LPI Contributions*, 1405(8330):37.

- Chesley, S. R. (2005). Potential impact detection for near-earth asteroids: The case of 99942 apophis (2004 mn4). *Proceedings of the International Astronomical Union*, 1(S229):215–228.
- Chesley, S. R., Baer, J., and Monet, D. G. (2010). Treatment of star catalog biases in asteroid astrometric observations. *Icarus*, 210(1):158–181.
- Chesley, S. R., Chodas, P. W., Milani, A., Valsecchi, G. B., and Yeomans, D. K. (2002). Quantifying the risk posed by potential earth impacts. *Icarus*, 159(2):423–432.
- Chesley, S. R., Farnocchia, D., Nolan, M. C., Vokrouhlický, D., Chodas, P. W., Milani, A., Spoto, F., Rozitis, B., Benner, L. A., Bottke, W. F., et al. (2014). Orbit and bulk density of the osiris-rex target asteroid (101955) bennu. *Icarus*, 235:5–22.
- Chesley, S. R., Ostro, S. J., Vokrouhlický, D., Čapek, D., Giorgini, J. D., Nolan, M. C., Margot, J.-L., Hine, A. A., Benner, L. A., and Chamberlin, A. B. (2003). Direct detection of the yarkovsky effect by radar ranging to asteroid 6489 golevka. *Science*, 302(5651):1739–1742.
- Copernicus, N. (1543). *De revolutionibus orbium coelestium*. Johannes Petreius.
- David, P., Mignard, F., Hestroffer, D., Tanga, P., Spoto, F., Berthier, J., Pauwels, T., Roux, W., Barbier, A., Cellino, A., et al. (2023). Gaia focused product release: Asteroid orbital solution-properties and assessment. *Astronomy & Astrophysics*, 680:A37.
- Del Vigna, A., Faggioli, L., Milani, A., Spoto, F., Farnocchia, D., and Carry, B. (2018). Detecting the yarkovsky effect among near-earth asteroids from astrometric data. *Astronomy & Astrophysics*, 617:A61.
- Ďurech, J., Vokrouhlický, D., Pravec, P., Hanuš, J., Farnocchia, D., Krugly, Y. N., Inasaridze, R., Ayvazian, V., Fatka, P., Chiorny, V., et al. (2018). Yorp and yarkovsky effects in asteroids (1685) toro,(2100) ra-shalom,(3103) eger, and (161989) cacus. *Astronomy & Astrophysics*, 609:A86.
- Dziadura, K., Bartczak, P., and Oszkiewicz, D. (2024). Yarkovsky effect and close approaches of the near-earth asteroids observed by the gaia space mission. *submitted to Astronomy & Astrophysics*.

- Dziadura, K., Oszkiewicz, D., and Bartczak, P. (2022). Investigating the most promising yarkovsky candidates using gaia dr2 astrometry. *Icarus*, 383:115040.
- Dziadura, K., Oszkiewicz, D., Spoto, F., Carry, B., Tanga, P., and Bartczak, P. (2023). The yarkovsky effect and bulk density of near-earth asteroids from gaia dr3. *Astronomy & Astrophysics*, 680:A77.
- Euler, L. (1744). *Methodus Inveniendi Lineas Curvas*. Unknown.
- Farnocchia, D., Chesley, S., Chamberlin, A., and Tholen, D. (2015). Star catalog position and proper motion corrections in asteroid astrometry. *Icarus*, 245:94–111.
- Farnocchia, D., Chesley, S., Vokrouhlický, D., Milani, A., Spoto, F., and Bottke, W. (2013). Near earth asteroids with measurable yarkovsky effect. *Icarus*, 224(1):1–13.
- Farnocchia, D., Chesley, S. R., Milani, A., Gronchi, G. F., and Chodas, P. W. (2015). *Orbits, Long-Term Predictions, Impact Monitoring*, pages 815–834.
- Farnocchia, D., Reddy, V., Bauer, J. M., Warner, E. M., Micheli, M., Payne, M. J., Farnham, T., Kelley, M. S., Balam, D. D., Barkov, A. P., et al. (2022). International asteroid warning network timing campaign: 2019 xs. *The Planetary Science Journal*, 3(7):156.
- Fedorets, G., Muinonen, K., Pauwels, T., Granvik, M., Tanga, P., Virtanen, J., Berthier, J., Carry, B., David, P., Dell’Oro, A., et al. (2018). Optimizing asteroid orbit computation for gaia with normal points. *Astronomy & Astrophysics*, 620:A101.
- Gaia, C., Brown, A., Vallenari, A., Prusti, T., De Bruijne, J., Babusiaux, C., Juhász, Á., Marschalkó, G., Marton, G., Molnár, L., et al. (2018). Gaia data release 2 summary of the contents and survey properties. *Astronomy & Astrophysics*, 616(1).
- Gauss, C. F. (1801). *Theoria Motus Corporum Coelestium in Sectionibus Conicis Solem Ambientium*. Perthes et Besser.
- Goossens, S., Rowlands, D. D., Mazarico, E., Liounis, A. J., Small, J. L., Highsmith, D. E., Swenson, J. C., Lyzhoft, J. R., Ashman, B. W., Getzandanner, K. M., et al. (2021). Mass and shape determination of (101955) bennu using differenced data from multiple osiris-rex mission phases. *The Planetary Science Journal*, 2(6):219.
- Goossens, S., Rowlands, D. D., Mazarico, E., Liounis, A. J., Small, J. L., Highsmith, D. E., Swenson, J. C., Lyzhoft, J. R., Ashman, B. W., Getzandanner, K. M.,

- Leonard, J. M., Geeraert, J. L., Adam, C. D., Antreasian, P. G., Barnouin, O. S., Daly, M. G., Seabrook, J. A., and Lauretta, D. S. (2021). Mass and Shape Determination of (101955) Bennu Using Differenced Data from Multiple OSIRIS-REx Mission Phases. , 2(6):219.
- Granvik, M., Morbidelli, A., Jedicke, R., Bolin, B., Bottke, W. F., Beshore, E., Vokrouhlický, D., Nesvorný, D., and Michel, P. (2018). Debiased orbit and absolute-magnitude distributions for near-earth objects. *Icarus*, 312:181–207.
- Greenberg, A. H., Margot, J.-L., Verma, A. K., Taylor, P. A., and Hodge, S. E. (2017). *Yarkovsky Drift Detections for 159 Near-Earth Asteroids*. eScholarship, University of California.
- Greenberg, A. H., Margot, J.-L., Verma, A. K., Taylor, P. A., and Hodge, S. E. (2020). Yarkovsky drift detections for 247 near-earth asteroids. *The Astronomical Journal*, 159(3):92.
- Halley, E. (1705). *A Synopsis of the Astronomy of Comets*. Printed for John Senex, London. Originally published in Philosophical Transactions of the Royal Society, Vol. 24, Mar. 1705.
- Hanuš, J., Vokrouhlický, D., Delbo, M., Farnocchia, D., Polishook, D., Pravec, P., Hornoch, K., Kučáková, H., Kušnirák, P., Stephens, R., et al. (2018). (3200) phaeon: Bulk density from yarkovsky drift detection. *Astronomy & Astrophysics*, 620:L8.
- Kepler, J. (1609). *Astronomia Nova*. Unknown Publisher.
- Kirkwood, D. (1866). On the theory of meteors. In *Proceedings of the American Association for the Advancement of Science*, volume 15, pages 8–14.
- Kristensen, L. K. (2009). Single lunation n-observation orbits. *Celestial mechanics and dynamical astronomy*, 105:275–287.
- La Spina, A., Paolicchi, P., Kryszczyńska, A., and Pravec, P. (2004). Retrograde spins of near-earth asteroids from the yarkovsky effect. *Nature*, 428(6981):400–401.
- Magnusson, P., Barucci, M. A., Drummond, J. D., Lumme, K., Ostro, S. J., Surdej, J., Taylor, R. C., and Zappalà, V. (1989). Determination of pole orientations and

- shapes of asteroids. In Binzel, R. P., Gehrels, T., and Matthews, M. S., editors, *Asteroids II*, pages 66–97.
- Marciniak, A., Bartczak, P., Müller, T., Sanabria, J., Alí-Lagoa, V., Antonini, P., Behrend, R., Bernasconi, L., Bronikowska, M., Butkiewicz-Bąk, M., et al. (2018). Photometric survey, modelling, and scaling of long-period and low-amplitude asteroids. *Astronomy & Astrophysics*, 610:A7.
- Markov, A. A. (1912). *Wahrscheinlichkeitsrechnung*. B. G. Teubner. Cornell University Library historical math monographs.
- marquis de Laplace, P. S. (1825). *Traité de mécanique céleste*, volume 5. Chez JBM Duprat, libraire pour les mathématiques, quai des Augustins.
- Marsden, B. (1985). Initial orbit determination—the pragmatist’s point of view. *Astronomical Journal (ISSN 0004-6256)*, vol. 90, Aug. 1985, p. 1541–1547., 90:1541–1547.
- Marsden, B. (1991). The computation of orbits in indeterminate and uncertain cases. *Astronomical Journal (ISSN 0004-6256)*, vol. 102, Oct. 1991, p. 1539–1552., 102:1539–1552.
- Milani, A. (1999). The asteroid identification problem: I. recovery of lost asteroids. *Icarus*, 137(2):269–292.
- Milani, A. and Gronchi, G. (2010). *Theory of orbit determination*. Cambridge University Press.
- Millis, R. L. and Dunham, D. W. (1989). Precise measurement of asteroid sizes and shapes from occultations. In Binzel, R. P., Gehrels, T., and Matthews, M. S., editors, *Asteroids II*, pages 148–170.
- Mora, A., González-Núñez, J., Baines, D., Durán, J., Gutiérrez-Sánchez, R., Racero, E., Salgado, J., and Segovia, J. C. (2017). The gaia archive. *Proceedings of the International Astronomical Union*, 12(S330):35–38.
- Morbidelli, A. (1996). The kirkwood gap at the 2/1 commensurability with jupiter: New numerical results. *Astronomical Journal v. 111*, p. 2453, 111:2453.
- Morrison, D., Chapman, C. R., Steel, D., and Binzel, R. P. (2004). Impacts and the public: communicating the nature of the impact hazard. *Mitigation of hazardous comets and asteroids*, pages 252–390.

- Mouret, S. and Mignard, F. (2011). Detecting the yarkovsky effect with the gaia mission: list of the most promising candidates. *Monthly Notices of the Royal Astronomical Society*, 413(2):741–748.
- Muononen, K. and Bowell, E. (1993). Asteroid orbit determination using bayesian probabilities. *Icarus*, 104(2):255–279.
- Nesvorný, D. and Bottke, W. F. (2004). Detection of the yarkovsky effect for main-belt asteroids. *Icarus*, 170(2):324–342.
- Newton, I. (1687). *Philosophiæ Naturalis Principia Mathematica*. Royal Society of London.
- Nugent, C., Margot, J., Chesley, S., and Vokrouhlický, D. (2012). Detection of semimajor axis drifts in 54 near-earth asteroids: New measurements of the yarkovsky effect. *The Astronomical Journal*, 144(2):60.
- Öpik, E. J. (1951). Collision probabilities with the planets and the distribution of interplanetary matter. In *Proceedings of the Royal Irish Academy. Section A: Mathematical and Physical Sciences*, volume 54, pages 165–199. JSTOR.
- Orlov, B. (1939). Determination of the preliminary orbit of a minor planet by two observations. *Pulkovo Obs. Circ*, 26:55–63.
- Ortiz, J. L., Santos-Sanz, P., Sicardy, B., Benedetti-Rossi, G., Bérard, D., Morales, N., Duffard, R., Braga-Ribas, F., Hopp, U., Ries, C., Nascimbeni, V., Marzari, F., Granata, V., Pál, A., Kiss, C., Pribulla, T., Komžík, R., Hornoch, K., Pravec, P., Bacci, P., Maestripieri, M., Nerli, L., Mazzei, L., Bachini, M., Martinelli, F., Succi, G., Ciabattari, F., Mikuz, H., Carbognani, A., Gaehrken, B., Mottola, S., Hellmich, S., Rommel, F. L., Fernández-Valenzuela, E., Campo Bagatin, A., Cikota, S., Cikota, A., Lecacheux, J., Vieira-Martins, R., Camargo, J. I. B., Assafin, M., Colas, F., Behrend, R., Desmars, J., Meza, E., Alvarez-Candal, A., Beisker, W., Gomes-Junior, A. R., Morgado, B. E., Roques, F., Vachier, F., Berthier, J., Mueller, T. G., Madio, J. M., Unsalan, O., Sonbas, E., Karaman, N., Erece, O., Koseoglu, D. T., Ozisik, T., Kalkan, S., Guney, Y., Niaei, M. S., Satir, O., Yesilyaprak, C., Puskullu, C., Kabas, A., Demircan, O., Alikakos, J., Charmandaris, V., Leto, G., Ohlert, J., Christille, J. M., Szakáts, R., Takácsné Farkas, A., Varga-Verebélyi, E., Marton, G., Marciniak, A., Bartczak, P., Santana-Ros, T., Butkiewicz-Bąk, M.,

- Dudziński, G., Alí-Lagoa, V., Gazeas, K., Tzouganatos, L., Paschalis, N., Tsamis, V., Sánchez-Lavega, A., Pérez-Hoyos, S., Hueso, R., Guirado, J. C., Peris, V., and Iglesias-Marzoa, R. (2017). The size, shape, density and ring of the dwarf planet Haumea from a stellar occultation. *Nature*, 550:219–223.
- Oszkiewicz, D., Muinonen, K., Virtanen, J., and Granvik, M. (2009). Asteroid orbital ranging using markov-chain monte carlo. *Meteoritics & Planetary Science*, 44(12):1897–1904.
- Pérez-Hernández, J. A. and Benet, L. (2022). Non-zero yarkovsky acceleration for near-earth asteroid (99942) apophis. *Communications Earth & Environment*, 3(1):1–5.
- Plackett, R. L. (1949). A historical note on the method of least squares. *Biometrika*, 36(3/4):458–460.
- Podlewska-Gaca, E., Marciniak, A., Alí-Lagoa, V., Bartczak, P., Müller, T. G., Szakáts, R., Duffard, R., Molnár, L., Pál, A., Butkiewicz-Bąk, M., et al. (2020). Physical parameters of selected gaia mass asteroids. *Astronomy & Astrophysics*, 638:A11.
- Press, W. H. (1992). *Numerical recipes in Fortran 77: the art of scientific computing*. Cambridge university press.
- Prusti, T., De Bruijne, J., Brown, A. G., Vallenari, A., Babusiaux, C., Bailer-Jones, C., Bastian, U., Biermann, M., Evans, D. W., Eyer, L., et al. (2016). The gaia mission. *Astronomy & astrophysics*, 595:A1.
- Reddy, V., Kelley, M. S., Dotson, J., Farnocchia, D., Erasmus, N., Polishook, D., Masiero, J., Benner, L. A., Bauer, J., Alarcon, M. R., et al. (2022a). Apophis planetary defense campaign. *The Planetary Science Journal*, 3(5):123.
- Reddy, V., Kelley, M. S., Dotson, J., Landis, R. R., McGraw, L. E., Micheli, M., Moskovitz, N. A., Sanchez, J. A., Taylor, P. A., Wheeler, L., et al. (2022b). Near-earth asteroid (66391) moshup (1999 kw4) observing campaign: Results from a global planetary defense characterization exercise. *Icarus*, 374:114790.
- Reddy, V., Kelley, M. S., Farnocchia, D., Ryan, W. H., Thomas, C. A., Benner, L. A., Dotson, J., Micheli, M., Brucker, M. J., Bus, S. J., et al. (2019). Near-earth asteroid 2012 tc4 observing campaign: Results from a global planetary defense exercise. *Icarus*, 326:133–150.

- Reddy, V., Kelley, M. S., and Landis, R. R. (2017). Tc4 observing campaign: An operational test of nasa planetary defense network. In *Advanced Maui Optical and Space Surveillance (AMOS) Technologies Conference*, page 111.
- Rubincam, D. P. (1988). Yarkovsky thermal drag on lageos. *Journal of Geophysical Research: Solid Earth*, 93(B11):13805–13810.
- Salgado, J., González-Núñez, J., Gutiérrez-Sánchez, R., Segovia, J. C., Durán, J., Hernández, J. L., and Arviset, C. (2017). The esa gaia archive: Data release 1. *Astronomy and Computing*, 21:22–26.
- Shor, V., Chernetenko, Y. A., Kochetova, O., and Zheleznov, N. (2012). On the impact of the yarkovsky effect on apophis’ orbit. *Solar System Research*, 46:119–129.
- Spoto, F., Tanga, P., Mignard, F., Berthier, J., Carry, B., Cellino, A., Dell’Oro, A., Hestroffer, D., Muinonen, K., Pauwels, T., et al. (2018). Gaia data release 2-observations of solar system objects. *Astronomy & astrophysics*, 616:A13.
- Spoto et al. in prep., F. (2024). in preparation.
- Tanga, P. and Delbo, M. (2007). Asteroid occultations today and tomorrow: toward the GAIA era. *A&A*, 474:1015–1022.
- Tanga, P., Pauwels, T., Mignard, F., Muinonen, K., Cellino, A., David, P., Hestroffer, D., Spoto, F., Berthier, J., Guiraud, J., et al. (2022). Gaia data release 3: the solar system survey.
- Vallenari, A., Brown, A., Prusti, T., de Bruijne, J., Arenou, F., Babusiaux, C., Biermann, M., Creevey, O., Ducourant, C., Evans, D., et al. (2023). Gaia data release 3-summary of the content and survey properties. *Astronomy & Astrophysics*, 674:A1.
- Veras, D., Leinhardt, Z. M., Eggl, S., and Gänsicke, B. T. (2015). Formation of planetary debris discs around white dwarfs–ii. shrinking extremely eccentric collisionless rings. *Monthly Notices of the Royal Astronomical Society*, 451(4):3453–3459.
- Vereš, P., Farnocchia, D., Chesley, S. R., and Chamberlin, A. B. (2017). Statistical analysis of astrometric errors for the most productive asteroid surveys. *Icarus*, 296:139–149.

- Virtanen, J., Muinonen, K., and Bowell, E. (2001). Statistical ranging of asteroid orbits. *Icarus*, 154(2):412–431.
- Vokrouhlický, D. and Farinella, P. (1998). Orbital evolution of asteroidal fragments into the ν_6 resonance via yarkovsky effects. *Astronomy and Astrophysics*, 335:351–362.
- Vokrouhlický, D., Farnocchia, D., Čapek, D., Chesley, S. R., Pravec, P., Scheirich, P., and Müller, T. G. (2015). The yarkovsky effect for 99942 apophis. *Icarus*, 252:277–283.
- Vokrouhlický, D., Milani, A., and Chesley, S. (2000). Yarkovsky effect on small near-earth asteroids: Mathematical formulation and examples. *Icarus*, 148(1):118–138.
- Yarkovsky, I. (1901). The density of luminiferous ether and the resistance it offers to motion. *Bryansk (available in the Appendix of M. Brož's thesis)*.

Part III

Publications

Publication I

Physical parameters of selected *Gaia* mass asteroids

E. Podlowska-Gaca¹, A. Marciniak¹, V. Alí-Lagoa², P. Bartczak¹, T. G. Müller², R. Szakáts³, R. Duffard⁴, L. Molnár^{3,5}, A. Pál^{3,6}, M. Butkiewicz-Bąk¹, G. Dudziński¹, K. Dziadura¹, P. Antonini⁷, V. Asenjo⁸, M. Audejean⁹, Z. Benkhaldoun¹⁰, R. Behrend¹¹, L. Bernasconi¹², J. M. Bosch¹³, A. Chapman¹⁴, B. Dintinjana²⁵, A. Farkas³, M. Ferrais¹⁵, S. Geier^{16,17}, J. Grice¹⁸, R. Hirsh¹, H. Jacquinet¹⁹, E. Jehin¹⁵, A. Jones²⁰, D. Molina²¹, N. Morales⁴, N. Parley²², R. Poncy²³, R. Roy²⁴, T. Santana-Ros^{26,27}, B. Seli³, K. Sobkowiak¹, E. Verebelyi³, and K. Żukowski¹

¹ Astronomical Observatory Institute, Faculty of Physics, Adam Mickiewicz University, Słoneczna 36, Poznań, Poland
e-mail: edypod@amu.edu.pl

² Max-Planck-Institut für extraterrestrische Physik (MPE), Giessenbachstrasse 1, 85748 Garching, Germany

³ Konkoly Observatory, Research Centre for Astronomy and Earth Sciences, Hungarian Academy of Sciences, 1121 Budapest, Konkoly Thege Miklós út 15-17, Hungary

⁴ Instituto de Astrofísica de Andalucía (CSIC), Glorieta de la Astronomía s/n, 18008 Granada, Spain

⁵ MTA CSFK Lendület Near-Field Cosmology Research Group, Budapest, Hungary

⁶ Astronomy Department, Eötvös Loránd University, Pázmány P. s. 1/A, H-1171 Budapest, Hungary

⁷ Observatoire des Hauts Patys, 84410 Bedoin, France

⁸ Asociación Astronómica Astro Henares, Centro de Recursos Asociativos El Cerro C/ Manuel Azaña, 28823 Coslada, Spain

⁹ B92 Observatoire de Chinon, Chinon, France

¹⁰ Oukaimeden Observatory, High Energy Physics and Astrophysics Laboratory, Cadi Ayyad University, Marrakech, Morocco

¹¹ Geneva Observatory, 1290 Sauverny, Switzerland

¹² Observatoire des Engarouines, 1606 chemin de Rigoy, 84570 Malemort-du-Comtat, France

¹³ B74, Avinguda de Catalunya 34, 25354 Santa Maria de Montmagastrell (Tàrraga), Spain

¹⁴ I39, Cruz del Sur Observatory, San Justo city, Buenos Aires, Argentina

¹⁵ Space Sciences, Technologies and Astrophysics Research Institute, Université de Liège, Allée du 6 Août 17, 4000 Liège, Belgium

¹⁶ Instituto de Astrofísica de Canarias, C/ Vía Lactea s/n, 38205 La Laguna, Tenerife, Spain

¹⁷ Gran Telescopio Canarias (GRANTECAN), Cuesta de San José s/n, 38712, Breña Baja, La Palma, Spain

¹⁸ School of Physical Sciences, The Open University, MK7 6AA, UK

¹⁹ Observatoire des Terres Blanches, 04110 Reillanne, France

²⁰ I64, SL6 IXE Maidenhead, UK

²¹ Anunaki Observatory, Calle de los Llanos, 28410 Manzanares el Real, Spain

²² The IEA, University of Reading, Philip Lyle Building, Whiteknights Campus, Reading, RG6 6BX, UK

²³ Rue des Ecoles 2, 34920 Le Cres, France

²⁴ Observatoire de Blauvac, 293 chemin de St Guillaume, 84570 Blauvac, France

²⁵ University of Ljubljana, Faculty of Mathematics and Physics Astronomical Observatory, Jadranska 19 1000 Ljubljana, Slovenia

²⁶ Departamento de Física, Ingeniería de Sistemas y Teoría de la Señal, Universidad de Alicante, 03080 Alicante, Spain

²⁷ Institut de Ciències del Cosmos, Universitat de Barcelona (IEEC-UB), Martí i Franqués 1, 08028 Barcelona, Spain

Received 25 July 2019 / Accepted 20 December 2019

ABSTRACT

Context. Thanks to the *Gaia* mission, it will be possible to determine the masses of approximately hundreds of large main belt asteroids with very good precision. We currently have diameter estimates for all of them that can be used to compute their volume and hence their density. However, some of those diameters are still based on simple thermal models, which can occasionally lead to volume uncertainties as high as 20–30%.

Aims. The aim of this paper is to determine the 3D shape models and compute the volumes for 13 main belt asteroids that were selected from those targets for which *Gaia* will provide the mass with an accuracy of better than 10%.

Methods. We used the genetic Shaping Asteroids with Genetic Evolution (SAGE) algorithm to fit disk-integrated, dense photometric lightcurves and obtain detailed asteroid shape models. These models were scaled by fitting them to available stellar occultation and/or thermal infrared observations.

Results. We determine the spin and shape models for 13 main belt asteroids using the SAGE algorithm. Occultation fitting enables us to confirm main shape features and the spin state, while thermophysical modeling leads to more precise diameters as well as estimates of thermal inertia values.

Conclusions. We calculated the volume of our sample of main-belt asteroids for which the *Gaia* satellite will provide precise mass determinations. From our volumes, it will then be possible to more accurately compute the bulk density, which is a fundamental physical property needed to understand the formation and evolution processes of small Solar System bodies.

Key words. minor planets, asteroids: general – techniques: photometric – radiation mechanisms: thermal

1. Introduction

Thanks to the development of asteroid modeling methods (Kaasalainen et al. 2002; Viikinkoski et al. 2015; Bartczak & Dudziński 2018), the last two decades have allowed for a better understanding of the nature of asteroids. Knowledge about their basic physical properties helps us to not only understand particular objects, but also the asteroid population as a whole. Nongravitational effects with a proven direct impact on asteroid evolution, such as the Yarkovsky-O'Keefe-Radzievskii-Paddack (YORP) and Yarkovsky effects, could not be understood without a precise knowledge about the spin state of asteroids. For instance, the sign of the orbital drift induced by the Yarkovsky effect depends on the target's sense of rotation (Rubincam 2001). Also, spin clusters have been observed among members of asteroid families (Slivan 2002) that are best explained as an outcome of the YORP effect (Vokrouhlický et al. 2003, 2015).

Precise determinations of the spin and shape of asteroids will be of the utmost significance for improving the dynamical modeling of the Solar System and also for our knowledge of the physics of asteroids. From a physical point of view, the mass and size of an asteroid yield its bulk density, which accounts for the amount of matter that makes up the body and the space occupied by its pores and fractures. For a precise density determination, we need a model of the body, which refers to its 3D shape and spin state. These models are commonly obtained from relative photometric measurements. In consequence, an estimation of the body size is required in order to scale the model. The main techniques used for size determination (for a review, see e.g., Āurech et al. 2015) are stellar occultations, radiometric techniques, or adaptive optics (AO) imaging, as well as the in situ exploration of spacecrafts for a dozen of visited asteroids.

The disk-integrated lightcurves obtained from different geometries (phase and aspect angles) can give us a lot of information about the fundamental parameters, such as rotation period, spin axis orientation, and shape. However, the shape obtained from lightcurve inversion methods is usually scale-free. Thus, we need to use other methods to express them in kilometers and calculate the volumes. The determination of asteroid masses is also not straightforward, but it is expected that *Gaia*, thanks to its precise astrometric measurements, will be able to provide masses for more than a hundred asteroids. This is possible for objects that undergo gravitational perturbations during close approaches with other minor bodies (Mouret et al. 2007).

There are already a few precise sizes that are available based on quality spin and shape models of *Gaia* mass targets, including convex inversion and All-Data Asteroid Modeling (ADAM) shapes (some based on Adaptive Optics, Vernazza et al. 2019). However, there are still many with only Near Earth Asteroid Thermal Model (NEATM) diameters. In this paper, we use the SAGE (Shaping Asteroids with Genetic Evolution) algorithm (Bartczak & Dudziński 2018) and combine it with thermophysical models (TPM) and/or occultations to determine the shape, spin, and absolute scale of a list of *Gaia* targets in order to calculate their densities. As a result, here, we present the spin solutions and 3D shape models of 13 large main belts asteroids for which they are expected to have mass measurements from the *Gaia* mission with a precision of better than 10%. For some objects, we compare our results with already existing models to test the reliability of our methods. Thanks to the increased photometric datasets produced by our project, previously existing solutions have been improved for the asteroids that were selected, and for two targets for which we determine the physical properties for the first time. We provide the scale and volume for all the

bodies that are studied with realistic error bars. These volumes combined with the masses from *Gaia* astrometry will enable precise bulk density determinations and further mineralogical studies. The selected targets are mostly asteroids with diameters larger than 100 km, which are considered to be remnants of planetesimals (Morbidelli et al. 2009). These large asteroids are assumed to only have small macroporosity, thus their bulk densities can be used for comparison purposes with spectra.

The paper is organized as follows. In Sect. 2 we present our observing campaign, give a brief description of the spin and shape modeling technique, including the quality assessment of the solution, and describe the fitting to the occultation chords and the thermophysical modeling. In Sect. 3 we show the results of our study of 13 main belt asteroids, and in Sect. 4 we summarize our findings. Appendix A presents the results of TPM modeling, while Appendix B contains fitting the SAGE shape models to stellar occultations.

2. Methodology

2.1. Observing campaign

In order to construct precise spin and shape models for asteroids, we used dense photometric disk-integrated observations. Reliable asteroid models require lightcurves from a few apparitions, that are well distributed along the ecliptic longitude. The available photometric datasets for selected *Gaia* mass targets are complemented by an observing campaign that provided data from unique geometries, which improved the existing models by probing previously unseen parts of the surface. Using the Super-WASP (Wide Angle Search for Planets) asteroid archive (Grice et al. 2017) was also very helpful, as it provided data from unique observing geometries. Moreover, in many cases new data led to updates of sidereal period values. The coordination of observations was also very useful for long period objects, for which the whole rotation could not be covered from one place during one night. We gathered our new data during the observing campaign in the framework of the H2020 project called Small Bodies Near And Far (SBNAF, Müller et al. 2018). The main observing stations were located in La Sagra (IAA CSIC, Spain), Piskéstető (Hungary), and Borowiec (Poland), and the observing campaign was additionally supported by the *Gaia*GOSA web service dedicated to amateur observers (Santana-Ros et al. 2016). For some objects, our data were complemented by data from the K2 mission of the *Kepler* space telescope (Szabó et al. 2017) and the TRAPPIST North and South telescopes (Jehin et al. 2011). Gathered photometric data went through careful analysis in order to remove any problematic issues, such as star passages, color extinction, bad pixels, or other instrumental effects. In order to exclude any unrealistic artefacts, we decided not to take into account data that were too noisy or suspect data. The most realistic spin and shape models can be reconstructed when the observations are spread evenly along the orbit; this allows one to observe all illuminated parts of the asteroid's surface. Therefore, in this study, we particularly concentrated on the observations of objects for which we could cover our targets in previously unseen geometries, which is similar to what was done for 441 Bathilde, for which data from 2018 provided a lot of valuable information. Figure 1 shows an example of the ecliptic longitude coverage for the asteroid 441 Bathilde.

2.2. Spin and shape modeling

We used the genetic algorithm, SAGE to calculate asteroid models (Bartczak & Dudziński 2018). SAGE allowed us to reproduce

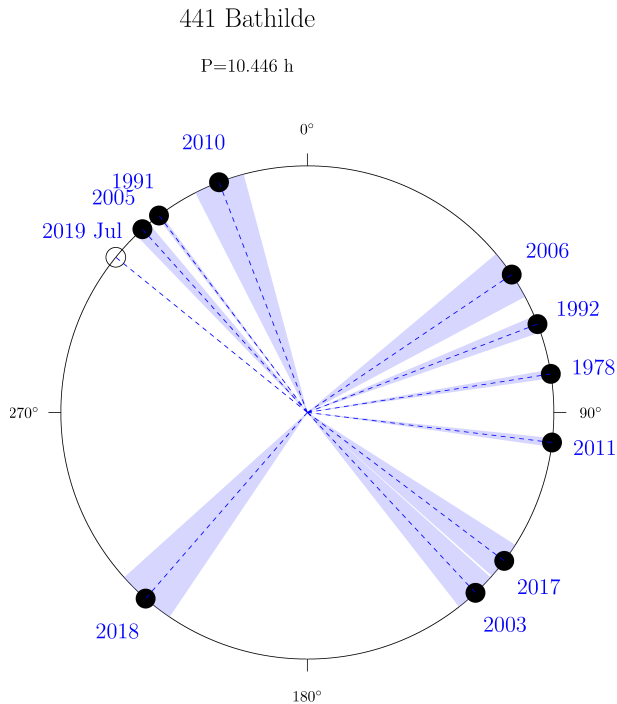


Fig. 1. Observer-centered ecliptic longitude of asteroid (441) Bathilde at apparitions with well covered lightcurves.

spin and nonconvex asteroid shapes based exclusively on photometric lightcurves. Here, we additionally introduce the recently developed quality assessment system (Bartczak & Dudziński 2019), which gives information about the reliability of the obtained models. The uncertainty of the SAGE spin and shape solutions was calculated by the multiple cloning of the final models and by randomly modifying the size and radial extent of their shape features. These clones were checked for their ability to simultaneously reproduce all the lightcurves within their uncertainties. By lightcurve uncertainty, we are referring to the uncertainty of each point. For the lightcurves with no uncertainty information, we adopted 0.01 mag. This way, the scale-free dimensions with the most extreme, but still possible shape feature modifications, were calculated and then translated to diameters in kilometers by fitting occultation chords. Some of the calculated models can be compared to the solutions obtained from other methods, which often use adaptive optics images, such as KOALA (Knitted Occultation, Adaptive-optics, and Lightcurve Analysis, Carry et al. 2010) and ADAM (Viikinkoski et al. 2015). Such models are stored in the DAMIT Database of Asteroid Models from Inversion Techniques (DAMIT) database¹ (Durech et al. 2010). Here, we show the nonconvex shapes that were determined with the SAGE method. We have only used the photometric data since they are the easiest to use and widely available data for asteroids. It should be noted, however, that some shape features, such as the depth of large craters or the height of hills, are prone to the largest uncertainty, as was shown by Bartczak & Dudziński (2019). It is also worth mentioning here that such a comparison of two methods is valuable as a test for the reliability of two independent methods and for the correctness of the existing solutions with the support of a wider set of photometric data. For a few targets from our sample, we provide more realistic, smoother shape solutions, which improve on the previously existing angular shape representations based

on limited or sparse datasets. For two targets, (145) Adeona and (308) Polyxo, the spin and shape solutions were obtained here for the first time.

2.3. Scaling the models by stellar occultations

The calculated spin and shape models are usually scale-free. By using two independent methods, the stellar occultation fitting and thermophysical modeling, we were able to provide an absolute scale for our shape models. The great advantage of the occultation technique is that the dimensions of the asteroid shadow seen on Earth can be treated as a real dimension of the object. Thus, if enough chords are observed, we can express the size of the object in kilometers. Moreover, with the use of multichord events, the major shape features can be recovered from the contours. To scale our shape models, we used the occultation timings stored in the Planetary Data System (PDS) database (Dunham et al. 2016). Only the records with at least three internally consistent chords were taken into account. The fitting of shape contours to events with fewer chords is burdened with uncertainties that are too large.

Three chords also do not guarantee precise size determinations because of substantial uncertainties in the timing of some events or the unfortunate spatial grouping of chords. We used the procedure implemented in Durech et al. (2011) to compare our shape models with available occultation chords. We fit the three parameters ξ , η (the fundamental plane here is defined the same as in Durech et al. 2011), and c , which was scaled in order to determine the size. The shape models' orientations were overlaid on the measured occultation chords and scaled to minimize χ^2 value. The difference with respect to the procedure described in Durech et al. (2011) is that we fit the projection silhouette to each occultation event separately, and we took the confidence level of the nominal solution into account as it was described in Bartczak & Dudziński (2019). We also did not optimize offsets of the occultations. Shape models fitting to stellar occultations with accompanying errors are presented in Figs. C.1–C.10. The final uncertainty in the volume comes from the effects of shape and occultation timing uncertainties and it is usually larger than in TPM since thermal data are very sensitive to the size of the body and various shape features play a lesser role there. On the other hand, precise knowledge of the sidereal period and spin axis position is of vital importance for the proper phasing of the shape models in both TPM and in occultation fitting. So, if a good fit is obtained by both methods, we consider it to be a robust confirmation for the spin parameters.

2.4. Thermophysical modeling (TPM)

The TPM implementation we used is based on Delbo & Harris (2002) and Alf-Lagoa et al. (2014). We already described our approach in Marciniak et al. (2018, 2019), which give details about the modeling of each target. So in this section, we simply provide a brief summary of the technique and approximations we make. In Appendix A, we include all the plots that are relevant to the modeling of each target and we provide some additional comments.

The TPM takes the shape model as input, and its main goal is to model the temperature on any given surface element (facet) at each epoch at which we have thermal IR (infrared) observations, so that the observed flux can be modeled. To account for heat conduction toward the subsurface, we solved the 1D heat diffusion equation for each facet and we used the Lagerros

¹ <http://astro.troja.mff.cuni.cz/projects/asteroids3D>

approximation for roughness (Lagerros 1996, 1998; Müller & Lagerros 1998; Müller 2002). We also consider the spectral emissivity to be 0.9 regardless of the wavelength (see, e.g., Delbo et al. 2015). We explored different roughness parametrizations by varying the opening angle of hemispherical craters covering 0.6 of the area of the facets (following Lagerros 1996). For each target, we estimated the Bond albedo that was used in the TPM as the average value that was obtained from the different radiometric diameters available from AKARI and/or WISE (Wright et al. 2010; Usui et al. 2011; Alf-Lagoa et al. 2018; Mainzer et al. 2016), and all available $H-G$, $H-G_{12}$, and $H-G_1-G_2$ values from the Minor Planet Center (Oszkiewicz et al. 2011, or Veres et al. 2015).

This approach leaves us with two free parameters, the scale of the shape (interchangeably called the diameter, D), and the thermal inertia (Γ). The diameters, which were calculated as volume-equivalent diameters, and other relevant information related to the TPM analyses of our targets are provided in Table A.1. Whenever there are not enough data to provide realistic error bar estimates, we report the best-fitting diameter so that the models can be scaled and compared to the scaling given by the occultations. On the other hand, if we have multiple good-quality thermal data, with absolute calibration errors below 10%, then this typically translates to a size accuracy of around 5% as long as the shape is not too extreme and the spin vector is reasonably well established. This general rule certainly works for large main belt asteroids, that is, the *Gaia* mass targets. We do not consider the errors that are introduced by the pole orientation uncertainties or the shapes (see Hanuš et al. 2016 and Bartzak & Dudziński 2019); therefore, our TPM error bars are lower estimates of the true error bars. The previously mentioned general rule or expectation is based on the fact that the flux is proportional to the square of the projected area, so fitting a high-quality shape and spin model to fluxes with 10% absolute error bars should produce a $\sim 5\%$ accurate size. This is verified by the large asteroids that were used as calibrators (Müller 2002; Harris & Lagerros 2002; Müller et al. 2014).

Nonetheless, we would still argue that generally speaking, scaling 3D shapes, which were only determined via indirect means (such as pure LC inversion) by modeling thermal IR data that were only observed close to pole-on, could potentially result in a biased TPM size if the shape has an over- or underestimated z -dimension (e.g., Bartzak & Dudziński 2019). This also happens with at least some radar models (e.g., Rozitis & Green 2014).

3. Results

The following subsections describe our results for each target, whereas Tables 1, 2, and A.1 provide the pole solutions, the results from the occultation fitting, and the results from TPM, respectively. The fit of the models to the observed lightcurves can be found for each object on the ISAM² (Interactive Service for Asteroid Models) web-service (Marciniak et al. 2012). On ISAM, we also show the fit of available occultation records for all objects studied in this paper. For comparison purposes, a few examples are given for SAGE shape models and previously existing solutions, which are shown in Figs. 2–6, as well as for previous period determinations and pole solutions, which are given in Table A.2. For targets without previously available spin and shape models, we determined the model based on the simple lightcurve inversion method (see Kaasalainen et al. 2002), such

as in Marciniak et al. (2018), and we compared the results with those from the SAGE method.

3.1. (3) Juno

We used observations from 11 apparitions to model Juno's shape. All lightcurves display amplitude variations from 0.12 to 0.22 mag, which indicates the body has a small elongation. Juno was already investigated with the ADAM method by Viikinkoski et al. (2015), which was based on ALMA (Atacama Large Millimeter Array) and adaptive optics data in addition to lightcurves. The rotation period and spin axis position of both models, ADAM and SAGE, are in good agreement. However, the shapes look different from some perspectives. The shape contours of the SAGE model are smoother and the main features, such as polar craters, were reproduced in both methods. We compared our SAGE model with AO data and the results from ADAM modeling by Viikinkoski et al. (2015) in Fig. 2. The fit is good, but not perfect.

A rich dataset of 112 thermal infrared measurements is available for (3) Juno, including unpublished *Herschel* PACS data (Müller et al. 2005). The complete PACS catalog of small-body data will be added to the SBNF infrared database once additional SBNF articles are published. For instance, the full TPM analysis of Juno will be included in an accompanying paper that features the rest of the PACS main-belt targets (Alf-Lagoa et al., in prep.). Here, we include Juno in order to compare the scales we obtained from TPM and occultations.

TPM leads to a size of 254 ± 4 km (see Tables 2 and A.1), which is in agreement with the ADAM solution (248 km) within the error bars. The stellar occultations from the years 1979, 2000, and 2014 also fit well (see Fig. C.1 for details). The 1979 event, which had the most dense coverage (15 chords), leads to a diameter of 260^{+13}_{-12} km.

3.2. (14) Irene

For (14) Irene, we gathered the lightcurves from 14 apparitions, but from very limited viewing geometries. The lightcurve shapes were very asymmetric, changing character from bimodal to monomodal in some apparitions, which indicates large aspect angle changes caused by low spin axis inclination to the orbital plane of the body. The amplitudes varied from 0.03 to 0.16 mag. The obtained SAGE model fits very well to the lightcurves; the agreement is close to the noise level. The spin solution is presented in Table 1. The SAGE model is in very good agreement with the ADAM model, which displays the same major shape features (see Fig. 3). This agreement can be checked for all available models by generating their sky projections at the same moment on the ISAM and DAMIT³ webpages.

The only three existing occultation chords seem to point to the slightly preferred SAGE solution from two possible mirror solutions (Fig. C.2), and it led to a size of 145^{+12}_{-12} km for the pole 1 solution. The TPM fit resulted in a compatible size of 155 km, which is in good agreement within the error bars. We note, however, that the six thermal IR data available are not substantial enough to give realistic TPM error bars (the data are fit with an artificially low minimum that was reduced to $\chi^2 \sim 0.1$), but nonetheless both of our size determinations here also agree with the size of the ADAM shape model based on the following adaptive optics imaging: $153 \text{ km} \pm 6 \text{ km}$ (Viikinkoski et al. 2017).

² <http://isam.astro.amu.edu.pl>

³ <http://astro.troja.mff.cuni.cz/projects/asteroids3D>

Table 1. Spin parameters of asteroid models obtained in this work, with their uncertainty values.

Sidereal period [h]	Pole 1		Pole 2		rmsd [mag]	Observing span (years)	N_{app}	N_{lc}
	λ_p [°]	β_p [°]	λ_p [°]	β_p [°]				
(3) Juno 7.209533 ^{+0.000009} _{-0.000013}	105 ⁺⁹ ₋₉	22 ⁺¹² ₋₂₂	–	–	0.015	1954–2015	11	28
(14) Irene 15.029892 ^{+0.000023} _{-0.000028}	91 ⁺¹ ₋₄	-14 ⁺⁹ ₋₂	267 ⁺⁵ ₋₂	-10 ⁺¹⁴ ₋₁	0.019	1953–2017	14	99
(20) Massalia 8.097587 ^{+0.000003} _{-0.000001}	111 ⁺¹⁶ ₋₁₅	77 ⁺¹⁷ ₋₇	293 ⁺¹⁷ ₋₁₇	76 ⁺²⁰ ₋₁₀	0.019	1955–2017	13	111
(64) Angelina 8.751708 ^{+0.000003} _{-0.000003}	135 ⁺⁴ ₋₁	12 ⁺¹² ₋₁₄	313 ⁺³ ₋₁	13 ⁺⁸ ₋₁₁	0.020	1981–2017	10	81
(68) Leto 14.845449 ^{+0.000004} _{-0.000003}	125 ⁺⁸ ₋₆	61 ⁺⁷ ₋₁₇	308 ⁺⁴ ₋₂	46 ⁺⁴ ₋₉	0.030	1978–2018	5	38
(89) Julia 11.388331 ^{+0.000007} _{-0.000005}	125 ⁺⁸ ₋₆	-23 ⁺⁸ ₋₆	–	–	0.012	1968–2017	4	37
(114) Kassandra 10.743552 ^{+0.000013} _{-0.000009}	189 ⁺⁴ ₋₅	-64 ⁺¹⁵ ₋₆	343 ⁺⁶ ₋₃	-69 ⁺¹³ ₋₁₁	0.019	1979–2018	8	43
(145) Adeona 15.070964 ^{+0.000038} _{-0.000044}	95 ⁺² ₋₂	46 ⁺¹ ₋₄	–	–	0.12	1977–2018	9	78
(297) Caecilia 4.151390 ^{+0.000005} _{-0.000003}	53 ⁺⁶ ₋₁	-36 ⁺¹¹ ₋₅	227 ⁺⁶ ₋₃	-51 ⁺¹¹ ₋₄	0.016	2004–2018	9	35
(308) Polyxo 12.029587 ^{+0.000006} _{-0.000007}	115 ⁺² ₋₂	26 ⁺⁵ ₋₂	295 ⁺¹ ₋₂	39 ⁺⁴ ₋₂	0.013	1978–2018	6	37
(381) Myrrha 6.571953 ^{+0.000003} _{-0.000004}	237 ⁺³ ₋₅	82 ⁺³ ₋₁₃	–	–	0.013	1987–2018	7	38
(441) Bathilde 10.443130 ^{+0.000009} _{-0.000005}	125 ⁺⁹ ₋₇	39 ⁺²⁴ ₋₂₆	287 ⁺⁸ ₋₁₅	52 ⁺²³ ₋₁₃	0.015	1978–2018	10	85
(721) Tabora 7.981234 ^{+0.000010} _{-0.000011}	173 ⁺⁴ ₋₅	-49 ⁺¹⁸ ₋₂₀	340 ⁺⁶ ₋₉	34 ⁺²⁰ ₋₂₆	0.042	1984–2018	5	62

Notes. The first column gives the sidereal period of rotation, next there are two sets of pole longitude and latitude. The sixth column gives the rms deviations of the model lightcurves from the data, and the photometric dataset parameters follow after (observing span, number of apparitions, and number of individual lightcurve fragments).

3.3. (20) Massalia

Data from 13 apparitions were at our disposal to model (20) Massalia, although some of them were grouped close together in ecliptic longitudes. Massalia displayed regular, bimodal lightcurve shapes with amplitudes from 0.17 to 0.27 mag. New data gathered within the SBNF and *Gaia*GOSA projects significantly improved the preliminary convex solution that exists in DAMIT (Kaasalainen et al. 2002), which has a much lower pole inclination and a sidereal period of 0.002 hours shorter. If we consider the long span (60 yr) of available photometric data and the shortness of the rotation period, such a mismatch causes a large shift in rotational phase after a large number of rotations.

The two SAGE mirror solutions have a smooth shape with a top shape appearance. Their fit to the occultation record from 2012 led to two differing size solutions of 106^{+6}_{-3} and 113^{+6}_{-10} km (Fig. C.3); both are smaller and outside the combined error bars of the 145 ± 2 km solution that was obtained from the TPM. The full TPM details and the PACS data will be presented in Ali-Lagoa et al. (in prep.). The SAGE shapes fit the thermal data much better than the sphere, which we consider as an indication that the model adequately captures the relevant shape details. We note that (20) Massalia is one of the objects for which the stellar occultation data are rather poor. This provides rough size determinations and underestimated uncertainties.

Table 2. Results from the occultation fitting of SAGE models.

Number	Name	Pole	Year of occultation	Diameter (km)	$+\sigma D$ (km)	$-\sigma D$ (km)
3	Juno		1979-12-11	260.0	13.0	-12.0
			2000-05-24	236.0	20.0	-17.0
			2014-11-20	250.0	12.0	-11.0
14	Irene	1	2013-08-02	145.8	12.0	-11.5
		2	2013-08-02	145.2	91.5	-18.1
20	Massalia	1	2012-10-09	106.5	4.8	-2.8
		2	2012-10-09	113.5	6.2	-9.9
64	Angelina	1	2004-07-03	48.9	3.8	-2.3
		2	2004-07-03	50.7	2.1	-3.0
68	Leto	1	1999-05-23	152.0	20.8	-18.3
		2	1999-05-23	132.8	8.4	-8.0
89	Julia		2005-08-13	138.7	14.2	-6.4
			2006-12-04	137.3	2.1	-4.5
145	Adeona		2005-02-02	145	4.3	-2.7
308	Polyxo	1	2000-01-10	133.5	5.8	-6.3
			2004-11-16	125.4	11.1	-8.6
			2010-06-02	128.8	3.0	-2.8
		2	2000-01-10	131.2	5.0	-2.9
			2004-11-16	125.3	10.7	-8.1
			2010-06-02	127.8	3.5	-4.3
381	Myrrha		1991-01-13	134.8	45.3	-12.8
441	Bathilde	1	2003-01-11	75.3	74.6	-10.0
		2	2003-01-11	76.8	15.9	-9.1

Notes. Mirror pole solutions are labeled “pole 1” and “pole 2”. Scaled sizes are given in kilometers as the diameters of the equivalent volume spheres.

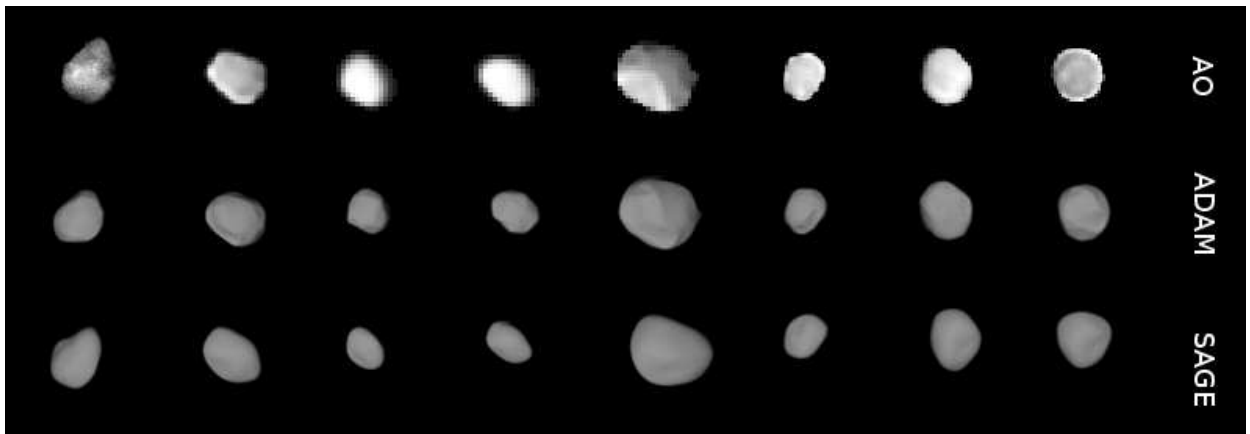


Fig. 2. Adaptive optics images of asteroid (3) Juno (*top*), the ADAM model sky projection by Viikinkoski et al. (2015) (*middle*), and the SAGE model (*bottom*) presented for the same epochs.

3.4. (64) Angelina

The lightcurves of (64) Angelina display asymmetric and variable behavior, with amplitudes ranging from 0.04 mag to 0.42 mag, which indicates a spin axis obliquity around 90 degrees. Data from ten apparitions were used to calculate the SAGE model. The synthetic lightcurves that were generated from the shape are in good agreement with the observed ones. Although the low value of the pole’s latitude of 12° is consistent

with the previous solution by Āurech et al. (2011) (see Table A.2 for reference), the difference of 0.0015 hours in the period is substantial. We favor our solution given our updated, richer dataset since Āurech et al. (2011) only had dense lightcurves from three apparitions that were complemented by sparse data with uncertainties of 0.1–0.2 mag (i.e., the level of lightcurve amplitude of this target). Also, the level of the occultation fit (Fig. C.4) and the TPM support our model. The thermal data were well reproduced

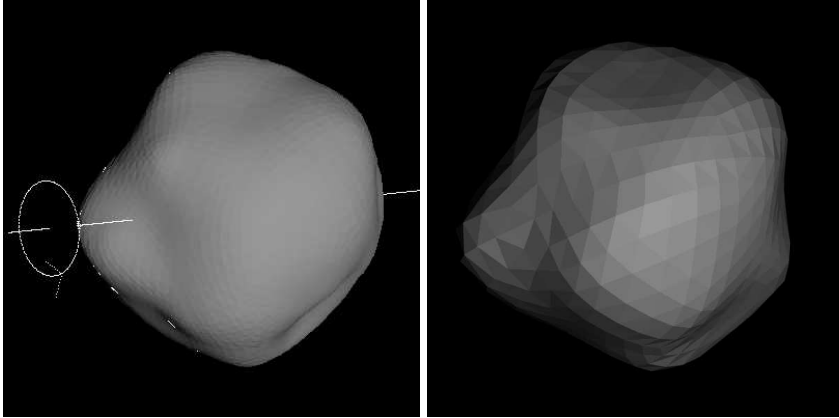


Fig. 3. Sky projections for the same epoch of SAGE (*left*) and ADAM (*right*) shape models of asteroid (14) Irene. Both shapes are in very good agreement.

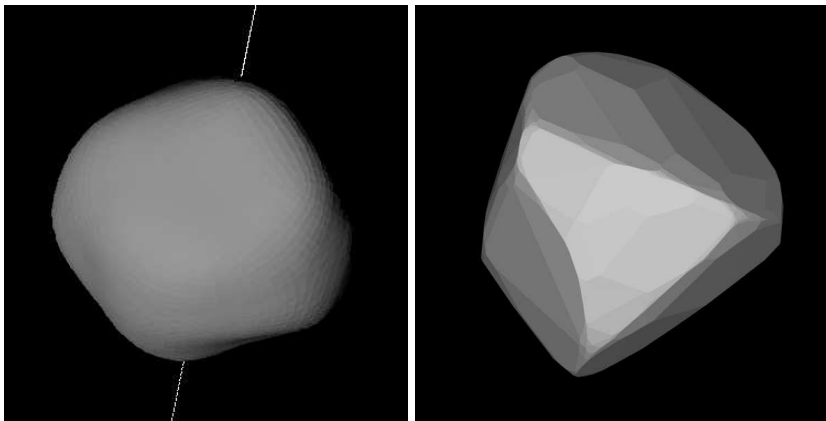


Fig. 4. Sky projections for the same epoch of the SAGE (*left*) and convex inversion (*right*) shape models of asteroid (68) Leto. SAGE provided a largely different and much smoother shape solution.

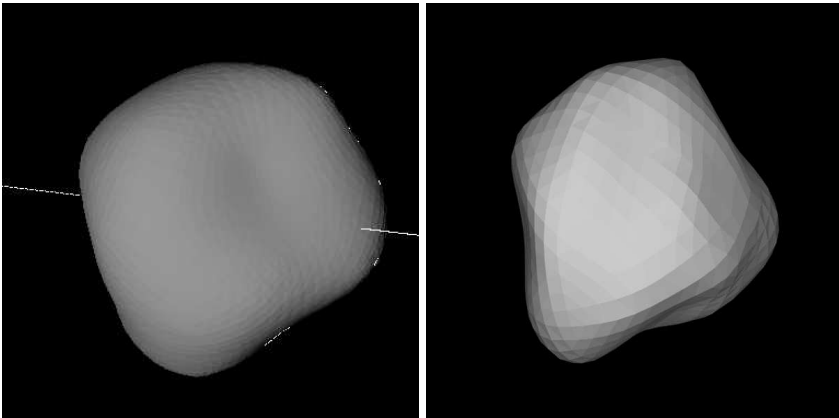


Fig. 5. Sky projections for the same epoch of SAGE (*left*) and ADAM (*right*) shape models of asteroid (89) Julia. A similar crater on the southern pole was reproduced by both methods.

with sizes that are slightly larger but consistent with the ones from the occultation fitting (54 versus 50 km, see Tables 2 and A.1), and they slightly favor the same pole solution.

3.5. (68) Leto

For Leto, data from six different apparitions consisted of somewhat asymmetric lightcurves with unequally spaced minima. Amplitudes ranged from 0.10 to 0.28 mag. The angular convex shape model published previously by Hanuš et al. (2013), which was mainly based on sparse data, is compared here with a much smoother SAGE model. Their on-sky projections on the same epoch can be seen in Fig. 4. The TPM analysis did not favor any of the poles. There was only one three-chords occultation, which the models did not fit perfectly, although pole 2 was fit better

this time (see Fig. C.5). Also, the occultation size of the pole 1 solution is 30 km larger than the radiometric one (152_{-18}^{+21} versus 121 km), with similarly large error bars, whereas the 133_{-8}^{+8} km size of the pole 2 solution is more consistent with the TPM and it has smaller error bars (see Table 2 and A.1).

3.6. (89) Julia

This target was shared with the VLT large program 199.C-0074 (PI: Pierre Vernazza), which obtained a rich set of well-resolved adaptive optics images using VLT/SPHERE instrument. Vernazza et al. (2018) produced a spin and shape model of (89) Julia using the ADAM algorithm on lightcurves and AO images, which enabled them to reproduce major nonconvex shape features. They identified a large impact crater that is possibly the

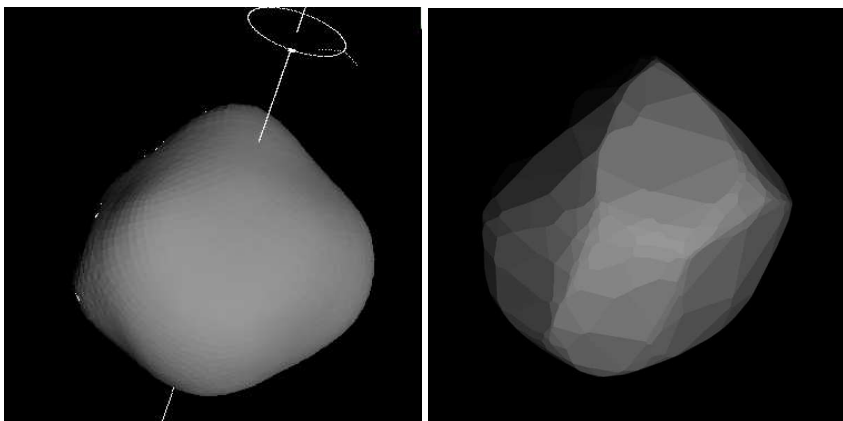


Fig. 6. Sky projections for the same epoch of SAGE (*left*) and convex inversion (*right*) shape models of asteroid (381) Myrrha. SAGE model is similar to the one from convex inversion, but it is less angular.

source region of the asteroids of the Julia collisional family. The SAGE model, which is based solely on disk-integrated photometry, also reproduced the biggest crater and some of the hills present in the ADAM model (Fig. 5). Spin parameters are in very good agreement. Interestingly, lightcurve data from only four apparitions were used for both models. However, one of them spanned five months, covering a large range of phase angles that highlighted the surface features due to various levels of shadowing. Both models fit them well, but the SAGE model does slightly worse. In the occultation fitting of two multichord events from the years 2005 and 2006, some of the SAGE shape features seem too small and others seem too large, but overall we obtain a size (138 km) that is almost identical to the ADAM model size (139 ± 3 km). The TPM requires a larger size (150 ± 10 km) for this model, but it is still consistent within the error bars.

3.7. (114) *Kassandra*

The lightcurves of *Kassandra* from nine apparitions (although only six have distinct geometries) showed sharp minima of uneven depths and had amplitudes from 0.15 to 0.25 mag. The SAGE shape model looks quite irregular, with a deep polar crater. It does not resemble the convex model by Āurech et al. (2018b), which is provided with a warning of its wrong inertia tensor. Nevertheless, the spin parameters of both solutions roughly agree. The SAGE model fits the lightcurves well, except for three cases involving the same ones that the convex model also failed to fit. This might indicate that they are burdened with some instrumental or other systematic errors. Unfortunately, no well-covered stellar occultations are available for *Kassandra*, so the only size determination could be done here by TPM (see Table A.1). Despite the substantial irregularity of the SAGE shape model, the spherical shape gives a similarly good fit to the thermal data.

3.8. (145) *Adeona*

Despite the fact that the available set of lightcurves came from nine apparitions, their unfortunate grouping resulted in only five distinct viewing aspects of this body. The small amplitudes (0.04–0.15 mag) displayed by this target were an additional hindering factor. Therefore, there was initially a controversy as to whether its period is close to 8.3 or 15 h. It was resolved by good quality data obtained by Pilcher (2010), which is in favor of the latter. SAGE model fit most of the lightcurves well, but it had problems with some where visible deviations are apparent.

This is the first model of this target, so there is not a previous model with which to compare it. The SAGE model looks almost spherical without notable shape features, so, as expected, the spherical shape provided a similarly good fit to the thermal data. The model fits the only available stellar occultation very well, which has the volume equivalent diameter of $145^{+4.3}_{-2.7}$ km.

3.9. (297) *Caecilia*

There were data from nine apparitions available for *Caecilia*, which were well spread in ecliptic longitude. The lightcurves displayed mostly regular, bimodal character of 0.15–0.28 mag amplitudes. The previous model by Hanuš et al. (2013) was created on a much more limited data set, with dense lightcurves covering only 1/3 of the orbit, which was supplemented by sparse data. So, as expected, that shape model is rather crude compared to the SAGE model. Nonetheless, the period and pole orientation is in good agreement between the two models, and there were similar problems with both shapes when fitting some of the lightcurves.

No stellar occultations by *Caecilia* are available with a sufficient number of chords, so the SAGE model was only scaled here by TPM (see Table A.1). However, the diameter provided here is merely the best-fitting value since the number of thermal IR data is too low to provide a realistic uncertainty estimate.

3.10. (308) *Polyxo*

The available lightcurve data set has been very limited for *Polyxo*, so no model could have been previously constructed. However, thanks to an extensive SBNAF observing campaign and the observations collected through *Gaia*GOSA, we now have data from six apparitions, covering five different aspects. The lightcurves were very irregular and had a small amplitude (0.08–0.22 mag), often displaying three maxima per period. To check the reliability of our solution, we determined the model based on the simple lightcurve inversion method. Then, we compared the results with those from the SAGE method. All the parameters are in agreement within the error bars between the convex and SAGE models. Still, the SAGE shape model looks rather smooth, with only small irregularities, and it fits the visible lightcurves reasonably well. There were three multichord occultations for *Polyxo* in PDS obtained in 2000, 2004, and 2010. Both pole solutions fit them at a good level (see Fig. C.8 for details) and produced mutually consistent diameters derived from each of the events separately (125–133 km, see Table 2). The TPM diameter (139 km) is slightly larger though. However,

in this case, there are not enough thermal data to provide a realistic estimate of the error bars.

3.11. (381) Myrrha

In the case of Myrrha, there were data from seven apparitions, but only five different viewing aspects. The lightcurves displayed a regular shape with a large amplitude from 0.3 to 0.36 mag. Thanks to the observing campaign that was conducted in the framework of the SBNAF project and the *Gaia*GOSA observers, we were able to determine the shape and spin state. Without the new data, the previous set of viewing geometries would have been limited to only 1/3 of the Myrrha orbit, and the earlier model by Hanuš et al. (2016) was constructed on dense lightcurves supplemented with sparse data. As a consequence, the previous model looks somewhat angular (cf. both shapes in Fig. 6). Due to a very high inclination of the pole to the ecliptic plane (high value of $|\beta|$), two potential mirror pole solutions were very close to each other. As a result, an unambiguous solution for the pole position was found. A very densely covered stellar occultation was available, although some of the 25 chords are mutually inconsistent and burdened with large uncertainties (see Fig. C.9). In the thermal IR, the SAGE model of Myrrha fits the rich data set better than the sphere with the same pole, giving a larger diameter. The obtained diameter has a small estimated error bar (131 ± 4 km) and it is in close agreement with the size derived from the occultation fitting of timing chords (135^{+45}_{-13} km).

3.12. (441) Bathilde

Seven different viewing geometries from ten apparitions were available for Bathilde. The amplitude of the lightcurves varied from 0.08 to 0.22 mag. Similarly, as in a few previously described cases, a previous model of this target based on sparse and dense data was available (Hanus et al. 2013). The new SAGE shape fit additional data and it has a smoother shape.

Shapes for both pole solutions fit the only available occultation well, and the resulting size (around 76 km) is in agreement with the size from TPM (72 ± 2 km). Interestingly, the second solution for the pole seems to be rejected by TPM, and the favored one fits thermal data much better than in the corresponding sphere. The resulting diameter is larger than the one obtained from AKARI, SIMPS, and WISE (see Tables 2, A.1 and A.2 for comparison).

3.13. (721) Tabora

Together with new observations that were gathered by the SBNAF observing campaign, we have data from five apparitions for Tabora. Amplitudes ranged from 0.19 to 0.50 mag, and the lightcurves were sometimes strongly asymmetric, with extrema at different levels. A model of Tabora has been published recently and it is based on joining sparse data in the visible with WISE thermal data (bands W3 and W4, Āurech et al. 2018a), but it does not have an assigned scale. The resulting shape model is somewhat angular, but it is in agreement with the SAGE model with respect to spin parameters. Stellar occultations are also lacking for Tabora, and the TPM only gave a marginally acceptable fit ($\chi^2 = 1.4$ for pole 1) to the thermal data, which is nonetheless much better than the sphere. Thus, the diameter error bar, in this case, is not optimal ($\sim 6\%$) and additional IR data and/or occultations would be required to provide a better constrained volume.

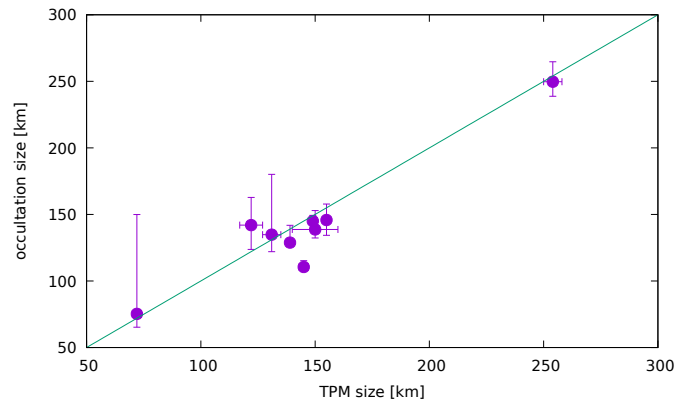


Fig. 7. Set of average occultation diameters vs. diameters from TPM. The straight line is $y = x$.

4. Conclusions

Here, we derived spin and shape models of 13 asteroids that were selected from *Gaia* mass targets, using only photometric lightcurves. It is generally possible to recover major shape features of main belt asteroids, but other techniques, such as direct images or adaptive optics, should be used to confirm the main features. We scaled our shape models by using stellar occultation records and TPM. The results obtained from both techniques are usually in good agreement, what can be seen in Fig. 7. In many ways, the stellar occultation fitting and thermophysical modeling are complementary to each other. In most cases, occultation chords match the silhouette within the error bars and rough diameters are provided. Also, thermophysical modeling resulted in more precise size determinations, thus additionally constraining the following thermal parameters: thermal inertia and surface roughness (see Table A.1). The diameters based on occultation fitting of complex shape models, inaccurate as they may seem here when compared to those from TPM, still reflect the dimensions of real bodies better than the commonly used elliptical approximation of the shape projection. The biggest advantage of scaling 3D shape models by occultations is that this procedure provides volumes of these bodies, unlike the fitting of 2D elliptical shape approximations, which only provides the lower limit for the size of the projection ellipse.

Resulting volumes, especially those with relatively small uncertainty, are going to be a valuable input for the density determinations of these targets once the mass values from the *Gaia* astrometry become available. In the cases where only convex solutions were previously available, nonconvex solutions created here will lead to more precise volumes, and consequently better constrained densities. In a few cases, our solutions are the first in the literature. The shape models, spin parameters, diameters, volumes, and corresponding uncertainties derived here are already available on the ISAM webpage.

Acknowledgements. The research leading to these results has received funding from the European Union's Horizon 2020 Research and Innovation Programme, under Grant Agreement no 687378 (SBNAF). Funding for the *Kepler* and K2 missions is provided by the NASA Science Mission directorate. L.M. was supported by the Premium Postdoctoral Research Program of the Hungarian Academy of Sciences. The research leading to these results has received funding from the LP2012-31 and LP2018-7 Lendület grants of the Hungarian Academy of Sciences. This project has been supported by the Lendület grant LP2012-31 of the Hungarian Academy of Sciences and by the GINOP-2.3.2-15-2016-00003 grant of the Hungarian National Research, Development and Innovation Office (NKFIH). TRAPPIST-South is a project funded by the Belgian Fonds de la Recherche Scientifique (F.R.S.-FNRS) under grant FRFC 2.5.594.09.F. TRAPPIST-North is a project funded by the University of Liège, and performed

in collaboration with Cadi Ayyad University of Marrakesh. E.J. is a FNRS Senior Research Associate. “The Joan Oró Telescope (TJO) of the Montsec Astronomical Observatory (OAdM) is owned by the Catalan Government and operated by the Institute for Space Studies of Catalonia (IEEC).” “This article is based on observations made with the SARA telescopes (Southeastern Association for Research in Astronomy), whose node is located at the Kitt Peak National Observatory (NOAO).” “This project uses data from the SuperWASP archive. The WASP project is currently funded and operated by Warwick University and Keele University, and was originally set up by Queen’s University Belfast, the Universities of Keele, St. Andrews, and Leicester, the Open University, the Isaac Newton Group, the Instituto de Astrofísica de Canarias, the South African Astronomical Observatory, and by STFC.” “This publication makes use of data products from the Wide-field Infrared Survey Explorer, which is a joint project of the University of California, Los Angeles, and the Jet Propulsion Laboratory/California Institute of Technology, funded by the National Aeronautics and Space Administration.” The work of TSR was carried out through grant APOSTD/2019/046 by Generalitat Valenciana (Spain)

References

- Alf-Lagoa, V., Lionni, L., Delbo, M., et al. 2014, *A&A*, **561**, A45
- Alf-Lagoa, V., Müller, T. G., Usui, F., Hasegawa, S. 2018, *A&A*, **612**, A85
- Bartczak, P., & Dudziński, G. 2018, *MNRAS*, **473**, 5050
- Bartczak, P., & Dudziński, G. 2019, *MNRAS*, **485**, 2431
- Carry, B. 2012, *Planet. Space Sci.*, **73**, 98
- Carry, B., Merline, W. J., Kaasalainen, M., et al. 2010, *BAAS*, **42**, 1050
- Delbo, M., & Harris, A. W. 2002, *Meteorit. Planet. Sci.*, **37**, 1929
- Delbo, M., Mueller, M., Emery, J. P., Rozitis, B., & Capria, M. T. 2015, *Asteroids IV*, eds. P. Michel, F. E. DeMeo, & W. F. Bottke (Tucson: University of Arizona Press), 107
- Dunham, D. W., Herald, D., Frappa, E., et al. 2016, NASA Planetary Data System, 243, EAR
- Đurech, J., Sidorin, V., Kaasalainen, M. 2010, *A&A*, **513**, A46
- Đurech, J., Kaasalainen, M., Herald, D., et al. 2011, *Icarus*, **214**, 652
- Đurech, J., Carry, B., Delbo, M., Kaasalainen, M., Viikinkoski, M. 2015, *Asteroids IV*, eds. P. Michel, F. E. DeMeo, & W. F. Bottke (Tucson: University of Arizona Press), 183
- Đurech, J., Hanuš, J., Alf-Lagoa, V., et al. 2018a *A&A*, **617**, A57
- Đurech, J., Hanuš, J., Broz, M., et al. 2018b, *Icarus*, **304**, 101
- Grice, J., Snodgrass, C., Green, S., Parley, N., & Carry, B. 2017, in *Asteroids, Comets, meteors: ACM 2017*
- Hanus, J., Durech, J., Broz, M., et al. 2013, *A&A*, **551**, A67
- Hanus, J., Durech, J., Oszkiewicz, D. A., et al. 2016, *A&A*, **586**, A108
- Harris, A. W.; Lagerros, J. S. V. 2002, *Asteroids III*, eds. W. F. Bottke Jr., A. Cellino, P. Paolicchi, & R. P. Binzel (Tucson: University of Arizona Press), 205
- Jehin, E., Gillon, M., Queloz, D., et al. 2011, *The Messenger*, **145**, 2
- Kaasalainen, M., Torppa, J., & Piironen, J. 2002, *Icarus*, **159**, 369
- Lagerros, J. S. V. 1996, *A&A*, **310**, 1011
- Lagerros, J. S. V. 1998, *A&A*, **332**, 1123
- Mainzer, A. K., Bauer, J. M., Cutri, R. M., et al. 2016, NASA Planetary Data System, id. EAR-A-COMPIL-5-NEOWISEDIAM-V1.0
- Marciniak, A., Bartczak, P., Santana-Ros, T., et al. 2012, *A&A*, **545**, A131
- Marciniak, A., Bartczak, P., Müller, T. G., et al. 2018, *A&A*, **610**, A7
- Marciniak, A., Alf-Lagoa, V., Müller, T. G., et al. 2019, *A&A*, **625**, A139
- Marsset, M., Carry, B., Dumas, C., et al. 2017, *A&A*, **604**, A64
- Michałowski, T., Velichko, F. P., Di Martino, M., et al. 1995, *Icarus*, **118**, 292
- Morbidelli, A., Bottke, W. F., Nesvorný, D., Levison, H. F. 2009, *Icarus*, **204**, 558
- Mouret, S., Hestroffer, D., & Mignard, F., 2007, *A&A*, **472**, 1017
- Müller, T. G. 2002, *Meteorit. Planet. Sci.*, **37**, 1919
- Müller, T. G., & Lagerros, J. S. V. 1998, *A&A*, **338**, 340
- Müller, T. G., Herschel Calibration Steering Group, & ASTRO-F Calibration Team 2005, ESA report
- Müller, T., Balog, Z., Nielbock, M., et al. 2014, *Exp. Astron.*, **37**, 253
- Müller, T. G., Marciniak, A., Kiss, Cs, et al. 2018, *Adv. Space Res.*, **62**, 2326
- Oszkiewicz, D. A., Muinonen, K., Bowell, E., et al. 2011, *J. Quant. Spectr. Rad. Transf.*, **112**, 1919
- Pilcher, F. 2010, *Minor Planet Bull.*, **37**, 148
- Rozitis, B., & Green, S. F. 2014, *A&A*, **568**, A43
- Rozitis, B., Green, S. F., MacLennan, E., et al. 2018, *MNRAS*, **477**, 1782
- Rubincam, D. P. 2001, *Icarus*, **148**, 2
- Santana-Ros, T., Marciniak, A., & Bartczak, P. 2016, *Minor Planet Bull.*, **43**, 205
- Scott, E. R. D., Keil, K., Goldstein, J. I., et al. 2015, *Asteroids IV*, eds. F. E. DeMeo, & W. F. Bottke (Tucson: University of Arizona Press), 573
- Slivan, S. M. 2002, *Nature*, **419**, 6902
- Szabó, Gy. M., Pál, A., Kiss, Cs., et al. 2017, *A&A*, **599**, A44
- Tedesco, E. F., Cellino, A., & Zappalà, V. 2005, *AJ*, **129**, 2869
- Usui, F., Kuroda, S., Müller, T. G., et al. 2011, *PASJ*, **63**, 1117
- Veres, P., Jedicke, R., Fitzsimmons, A., et al. 2015, *Icarus*, **261**, 34
- Vernazza, P., Broz, M., Drouard, A., et al. 2018, *A&A*, **618**, A154
- Vernazza, P., Jorda, L., Ševeček, P., et al. 2019, *Nat. Astron.*, **477V**
- Viikinkoski, M., Kaasalainen, M., Durech, J., et al. 2016 *A&A*, **581**, L3
- Viikinkoski, M., Hanus, J., Kaasalainen, M., Marchis, F., & Durech, J. 2017, *A&A*, **607**, A117
- Vokrouhlický, D., Nesvorný, D., & Bottke, W. F. 2003, *Nature*, **425**, 6954
- Vokrouhlický, D., Bottke, W. F., Chesley, S. R., et al. 2015, *Asteroids IV*, eds. P. Michel, F. E. DeMeo, & W. F. Bottke, (Tucson: University of Arizona Press), 895, 509
- Wright, E. L., Eisenhardt, P. R. M., Mainzer, A. K., et al. 2010, *AJ*, **140**, 1868

Appendix A: Additional tables**Table A.1.** Summary of TPM results, including the minimum reduced chi-squared ($\bar{\chi}_m^2$), the best-fitting diameter (D) and corresponding 1σ statistical error bars, and the number of IR data that were modeled (N_{IR}).

Target [pole]	N_{IR}	TLC	$\bar{\chi}_m^2$	$D \pm \sigma D$ (km)	$\bar{\chi}_m^2$ for sphere	Γ [SI units]	Roughness	Comments
(3) Juno	112	No	1.3	254 ± 4	1.0	70^{+30}_{-40}	≥ 1.00	Borderline acceptable fit. Sphere does better
(14) Irene 1	6	No	0.1	155	0.4	70	0.80	Very few data to provide realistic error bars
(14) Irene 2	6	No	0.2	154	0.2	70	0.80	Idem
(20) Massalia 1,2	72	No	0.5	145 ± 2	1.6	35^{+25}_{-10}	≤ 0.20	Mirror solutions provide virtually same fit
(64) Angelina 1	23	Yes	0.8	54 ± 2	1.10	35^{+25}_{-20}	0.20	Did not model MSX data
(64) Angelina 2	23	Yes	1.16	54 ± 2	1.24	20^{+25}_{-10}	0.25	Idem
(68) Leto 1	55	Yes	0.6	121 ± 5	0.83	40^{+25}_{-20}	0.50	Small offset between mirror solutions (not stat. significant)
(68) Leto 2	55	Yes	0.7	123 ± 5	0.87	35^{+45}_{-25}	0.45	Idem
(89) Julia	27	No	1.0	150 ± 10	1.5	100^{+150}_{-50}	≥ 0.90	Only northern aspect angles covered ($A < 70^\circ$) in the IR. Unexpectedly high thermal inertia fits better probably because the phase angle coverage is not well balanced (only 3 measurements with $\alpha > 0$)
(114) Cassandra 1,2	46	Yes	0.6	98 ± 3	0.70	20^{+30}_{-20}	0.55	Quite irregular but spheres provide similar fit
(145) Adeona	17	No	0.47	149 ± 10	0.23	70^{+130}_{-70}	0.60	Phase angle coverage is not well balanced between pre- and post-opposition
(297) Caecilia	13	No	0.9	41	0.9	10	0.35	Too few data to give realistic error bars
(308) Polyxo 1,2	13	No	0.4	139	0.35	50	0.45	Too few data to give realistic error bars
(381) Myrrha	73	Yes	0.40	131 ± 4	1.6	80^{+40}_{-40}	≥ 1.00	Good fit but some small waviness in residuals vs. rot. phase plot
(441) Bathilde 1	26	Yes	0.7	72 ± 2	1.7	180^{+20}_{-60}	≥ 0.90	Very high thermal inertia
(441) Bathilde 2	26	Yes	1.6	–	> 2	–	–	Bad fit
(721) Tabora 1	40	Yes	1.4	78 ± 5	> 5	6^{+14}_{-6}	0.65	Borderline acceptable fit, still better than sphere
(721) Tabora 2	40	Yes	2.1	–	> 5	–	–	Bad fit

Notes. TLC (Yes/No) refers to the availability of at least one thermal lightcurve with eight or more points sampling the rotation period. The $\bar{\chi}_m^2$ obtained for a spherical model with the same spin properties is shown. We also provide the value of thermal inertia Γ and surface roughness. Whenever the two mirror solutions provided different optimum diameters, we show them in different lines. Acceptable solutions, and preferred ones whenever it applies to mirror models, are highlighted in bold face.

Table A.2. Results from the previous solutions available in the literature.

Sidereal period [h]	Pole 1		Pole 2		D km	Reference
	λ_p	β_p	λ_p	β_p		
(3) Juno 7.20953	105°	21°	–	–	248 ± 5	Viikinkoski et al. (2015)
(14) Irene 15.02987	91°	–15°	–	–	153 ± 6	Viikinkoski et al. (2017)
(20) Massalia 8.09902	179°	39°	360°	40°	131.56/145.5/– ^(*)	Kaasalainen et al. (2002)
(64) Angelina 8.75033	138°	14°	317°	17°	52 ± 10	Đurech et al. (2011)
(68) Leto 14.84547	103°	43°	290°	23°	112 ± 14	Hanuš et al. (2013)
(89) Julia 11.388332	14°	–24°	–	–	140 ± 3	Vernazza et al. (2018)
(114) Cassandra 10.74358	196°	–55°	4°	–58°	93.91/99.65/100 ^(*)	Đurech et al. (2018b)
(145) Adeona –	–	–	–	–	141.39/151.14/151 ^(*)	
(297) Caecilia 4.151388	47°	–33°	223°	–53°	42.28/39.48/– ^(*)	Hanuš et al. (2013)
(308) Polyxo –	–	–	–	–	135.25/140.69/144.4 ^(*)	
(381) Myrrha 6.57198	3°	48°	160°	77°	117.12/120.58/129 ^(*)	Hanuš et al. (2016)
(441) Bathilde 10.44313	122°	43°	285°	55°	59.42/70.32/70.81 ^(*)	Hanuš et al. (2013)
(721) Tabora 7.98121	172°	53°	343°	38°	81.95/76.07/86.309 ^(*)	Đurech et al. (2018a)

Notes. Mirror pole solutions are labeled “pole 1” and “pole 2”. Scaled sizes are given in kilometers as the diameters of the equivalent volume spheres. For objects marked with ^(*) we have taken the sizes from the AKARI, SIMPS, and WISE (Usui et al. 2011; Tedesco et al. 2005; Mainzer et al. 2016) missions, respectively, for which the sizes were often calculated with an STM approximation of the spherical shape, and often without a known pole solution.

Appendix B: TPM plots and comments

The data we used was collected in the SBNAF infrared database⁴. In this section, we provide observation-to-model ratio (OMR) plots produced for the TPM analysis. Whenever there was a thermal lightcurve available within the data set of a target, this was also plotted (see Table A.1). In general, IRAS data have larger error bars, carry lower weights, and, therefore, their OMRs tend to present larger deviations from one. On a few occasions, some or all of them were even removed from the χ^2 optimization, as indicated in the corresponding figure caption. To save space, we only include the plots for one of the mirror solutions either because the TPM clearly rejected the other one or because the differences were so small that the other set of plots are redundant. Either way, that information is given in Table A.1. Table B.1 links each target to its corresponding plots in this section.

Table B.1. Targets and references to the relevant figures.

Target	OMR plots	Thermal lightcurve
(3) Juno	Fig. B.4	–
(14) Irene	Fig. B.5	–
(20) Massalia	Fig. B.6	–
(64) Angelina	Fig. B.7	Fig. B.1 (left)
(68) Leto	Fig. B.8	Fig. B.1 (right)
(89) Julia	Fig. B.9	–
(114) Cassandra	Fig. B.10	Fig. B.2 (left)
(145) Adeona	Fig. B.11	–
(308) Polyxo	Fig. B.13	–
(381) Myrrha	Fig. B.14	Fig. B.2 (right)
(441) Bathilde	Fig. B.15	Fig. B.3 (left)
(721) Tabora	Fig. B.16	Fig. B.3 (right)

⁴ <https://ird.konkoly.hu/>

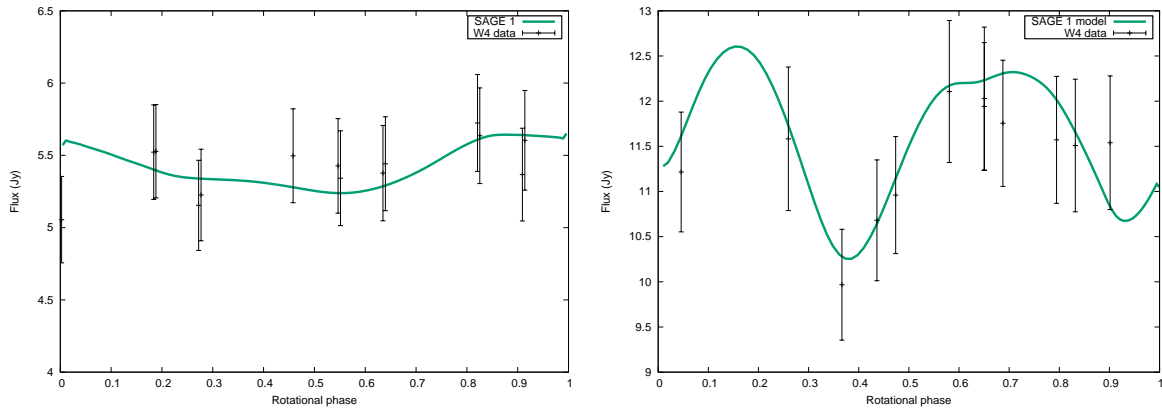


Fig. B.1. W4 data and model of thermal lightcurves that were generated with the best-fitting thermal parameters and size. *Left:* (64) Angelina's SAGE pole 1 model. *Right:* (68) Leto, also Pole 1.

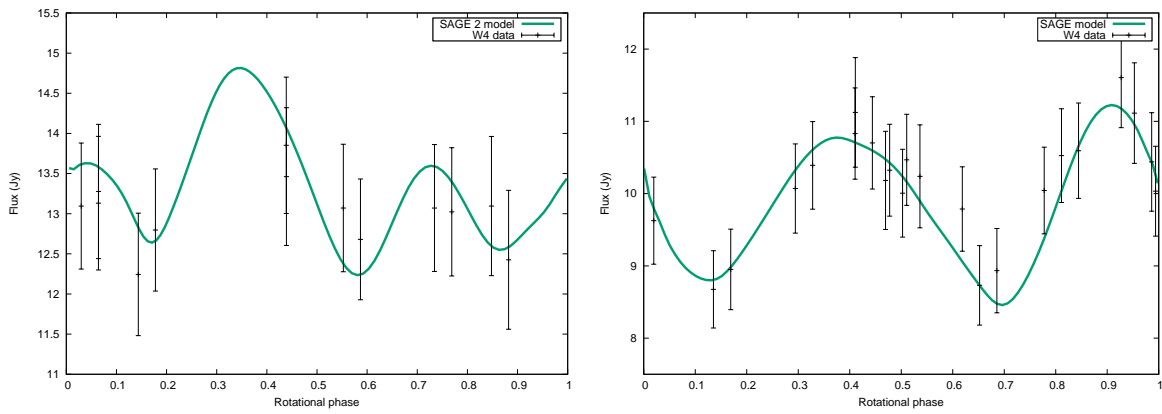


Fig. B.2. *Left:* (114) Kassandra. *Right:* (381) Myrrha.

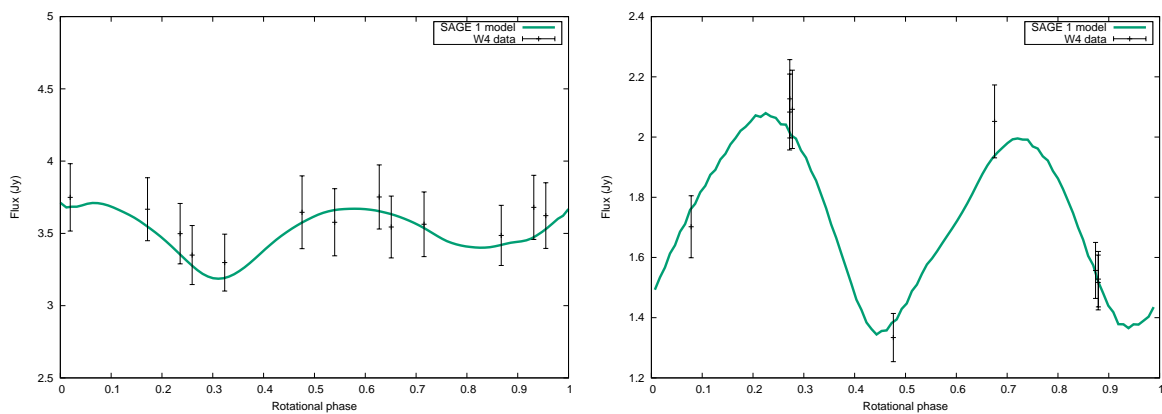


Fig. B.3. *Left:* (441) Bathilde. *Right:* (721) Tabora.

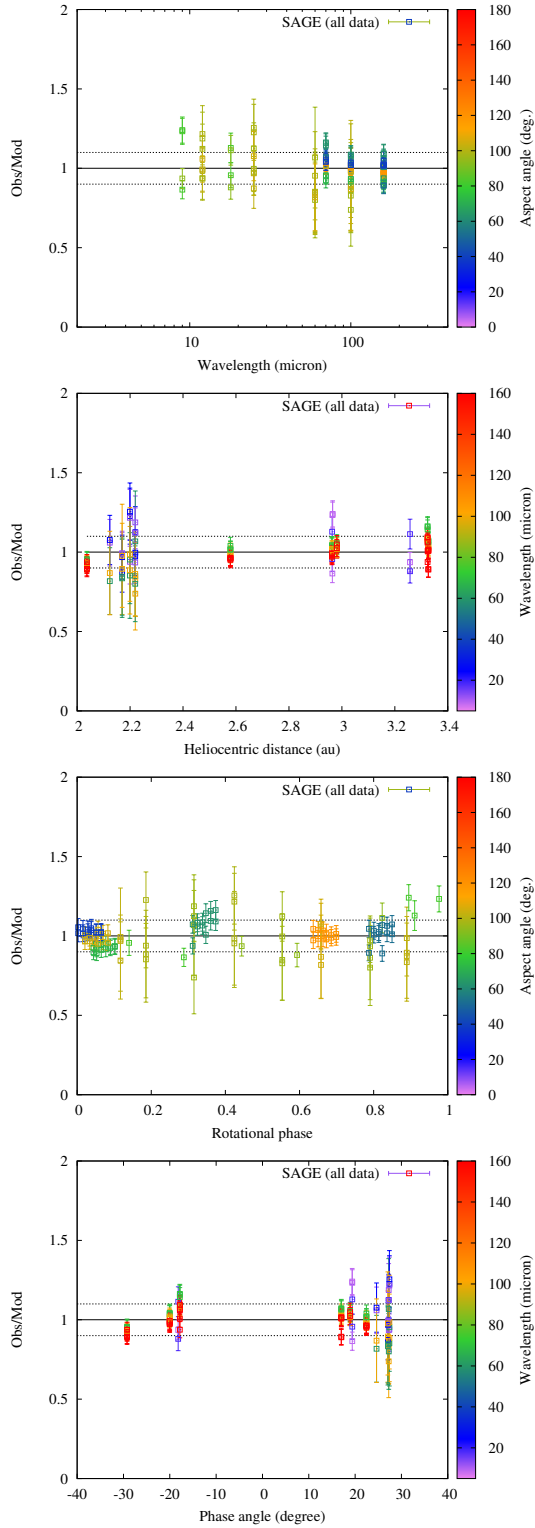


Fig. B.4. (3) Juno (from top to bottom): observation-to-model ratios versus wavelength, heliocentric distance, rotational phase, and phase angle. The color bar either corresponds to the aspect angle or to the wavelength at which each observation was taken. There are some systematics in the rotational phase plot, which indicate there could be some small artifacts in the shape.

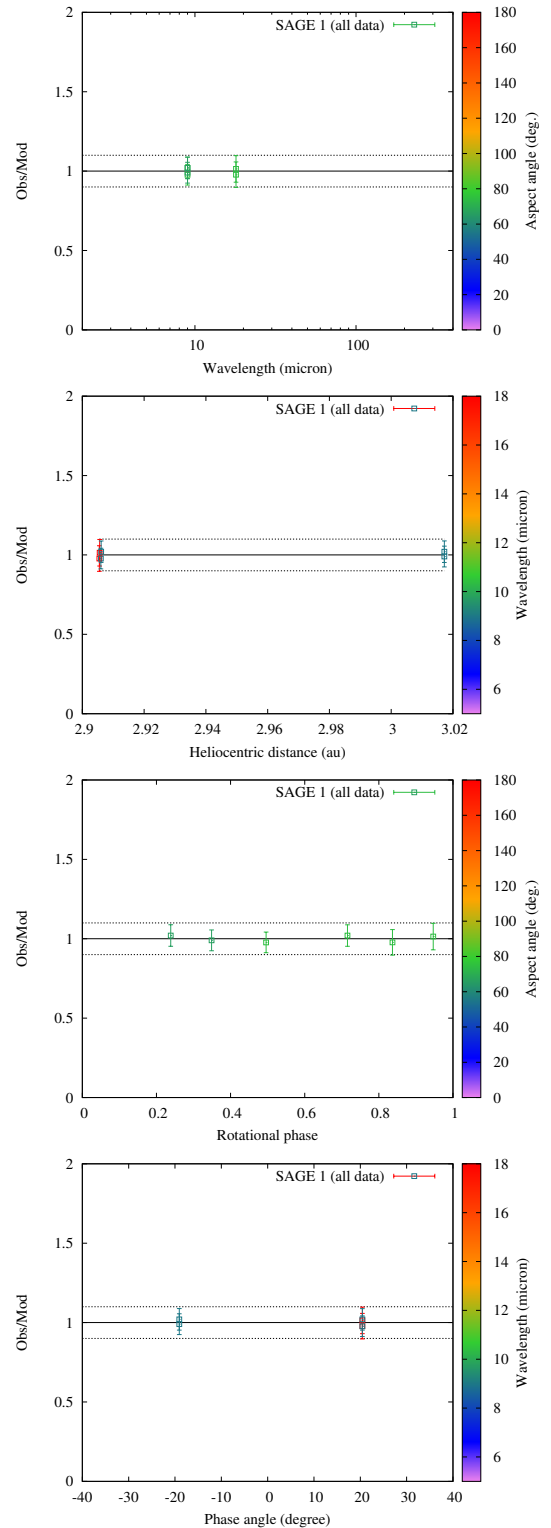


Fig. B.5. (14) Irene (from top to bottom): observation-to-model ratios versus wavelength, heliocentric distance, rotational phase, and phase angle. The plots that correspond to the pole 2 solution are very similar.

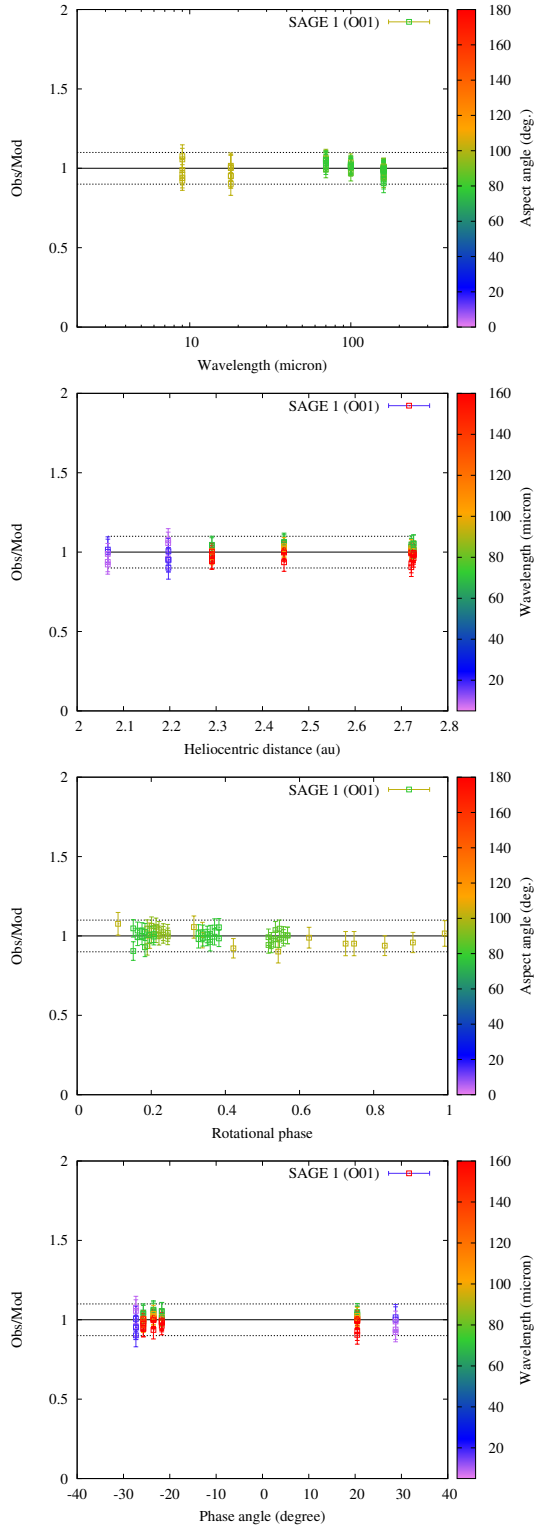


Fig. B.6. (20) Massalia. The O01 label indicates that the IRAS data were removed from the analysis, in this case because their quality was too poor.

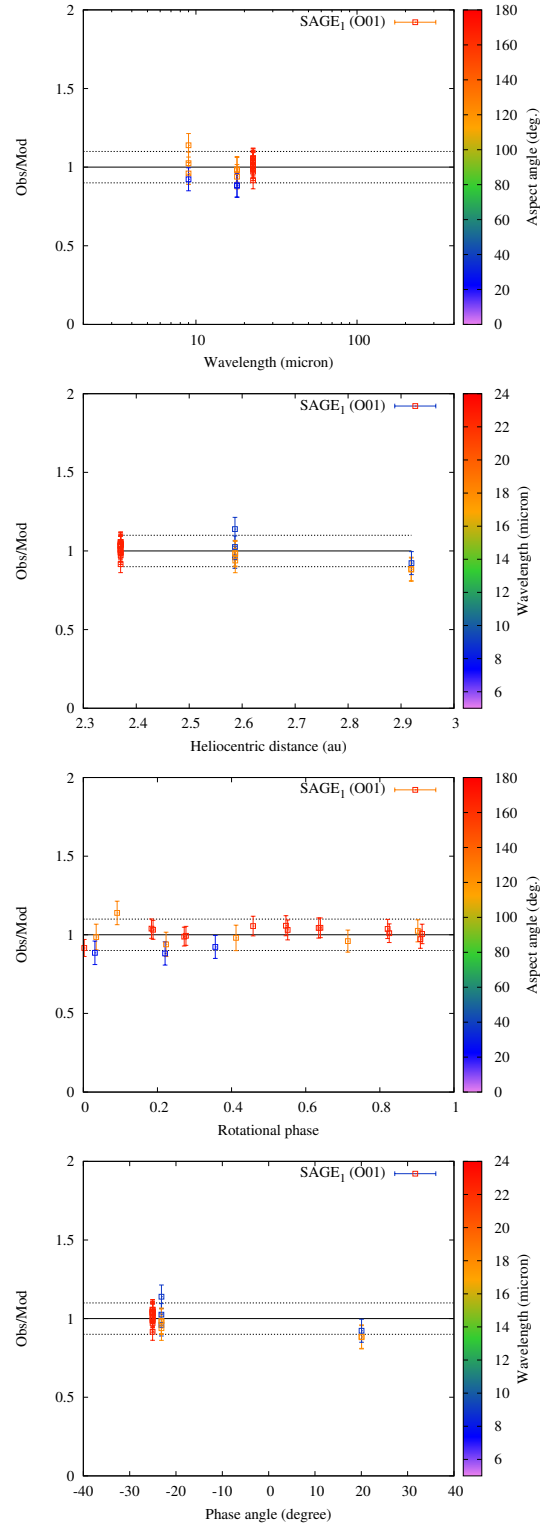


Fig. B.7. (64) Angelina. Pole 1 was favored in this case because it provided a significantly lower minimum χ^2 . The O01 label indicates that the very few MSX were clear outliers and were removed from the analysis.

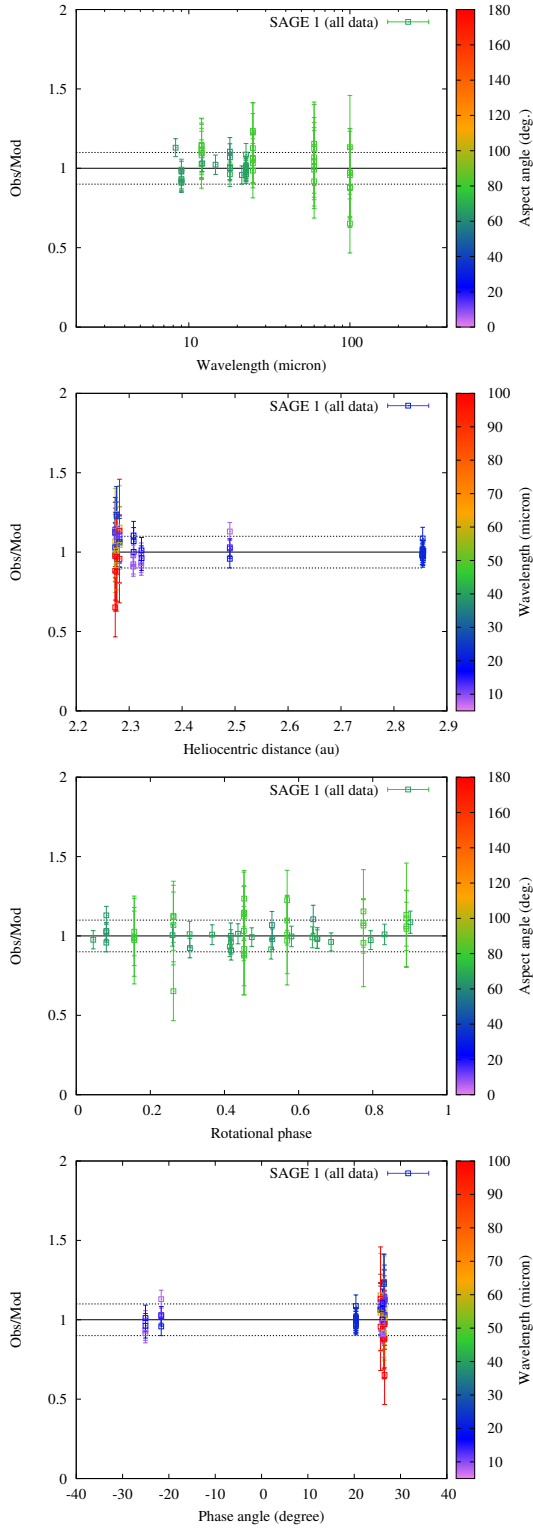


Fig. B.8. (68) Leto. The two mirror solutions fitted the data statistically equally well.

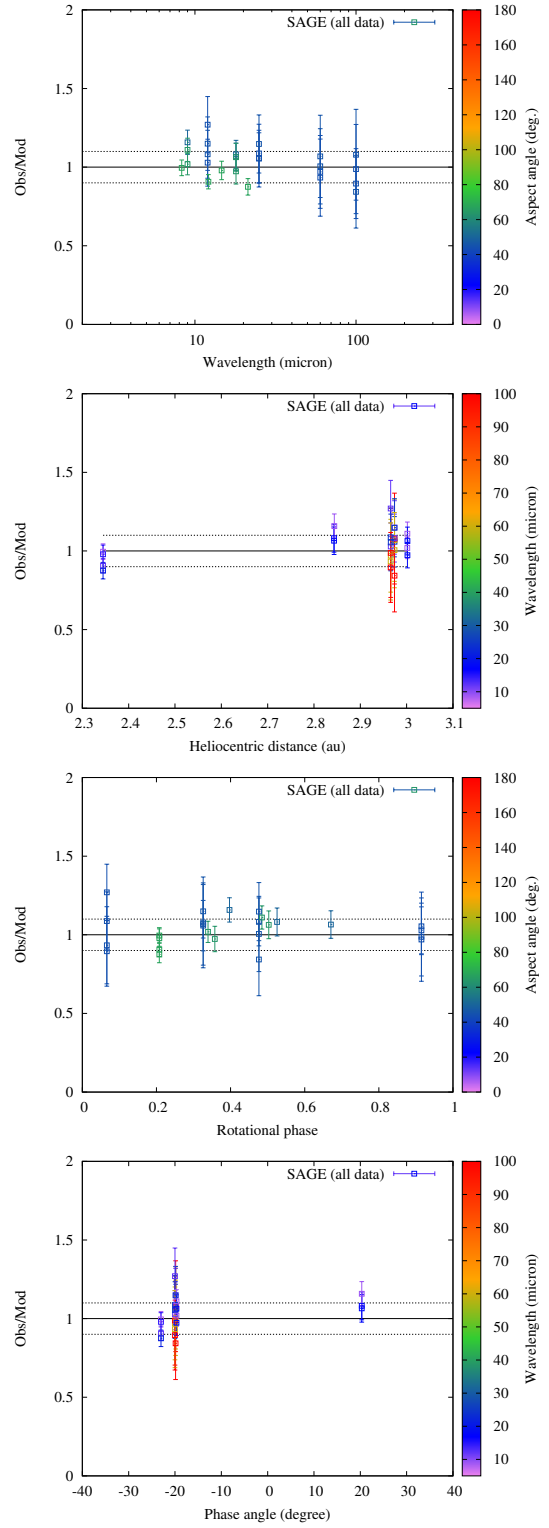


Fig. B.9. (89) Julia. The SAGE model provided a formally acceptable fit to the data (see Table A.1) but the optimum thermal inertia (150 SI units) is higher than expected for such a large main-belt asteroid. It is probably an artefact and manifests itself in the strong slope in the wavelength plot. The bias could be caused by two possible factors: We did not consider the dependence of thermal inertia with temperature (see e.g., Marsset et al. 2017; Rozitis et al. 2018) and the data were taken over a wide range of heliocentric distances; the thermal inertia is not well constrained because we have very few observations at positive phase angles.

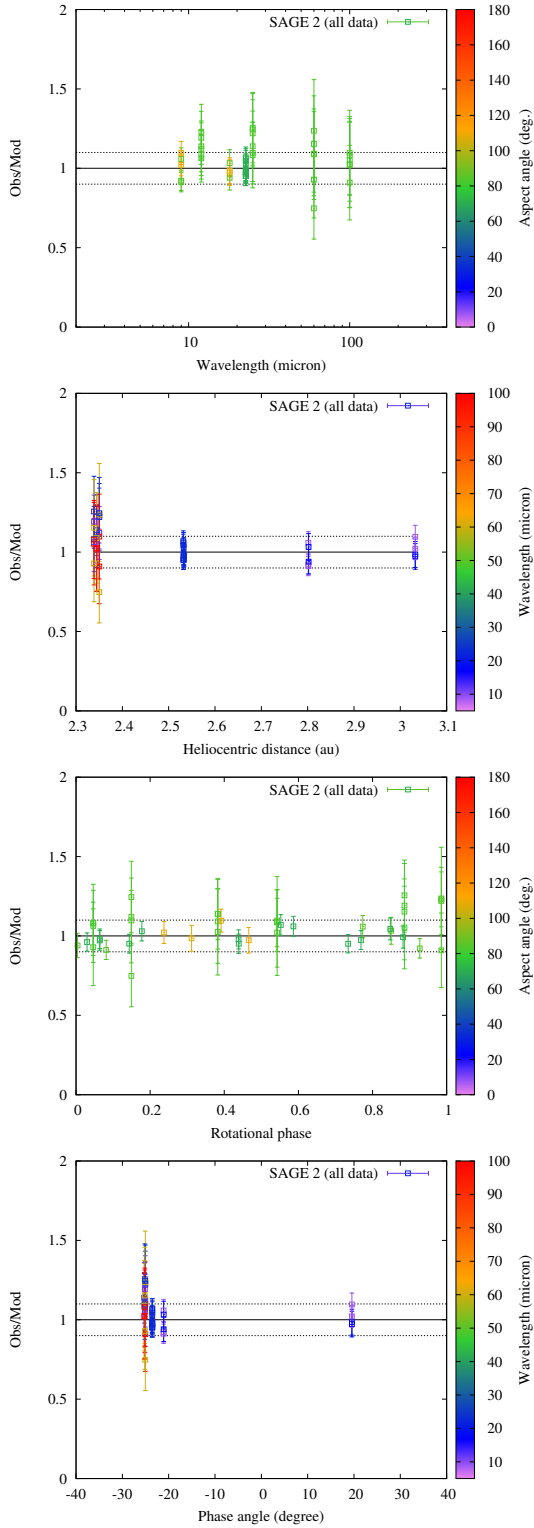


Fig. B.10. (114) Cassandra.

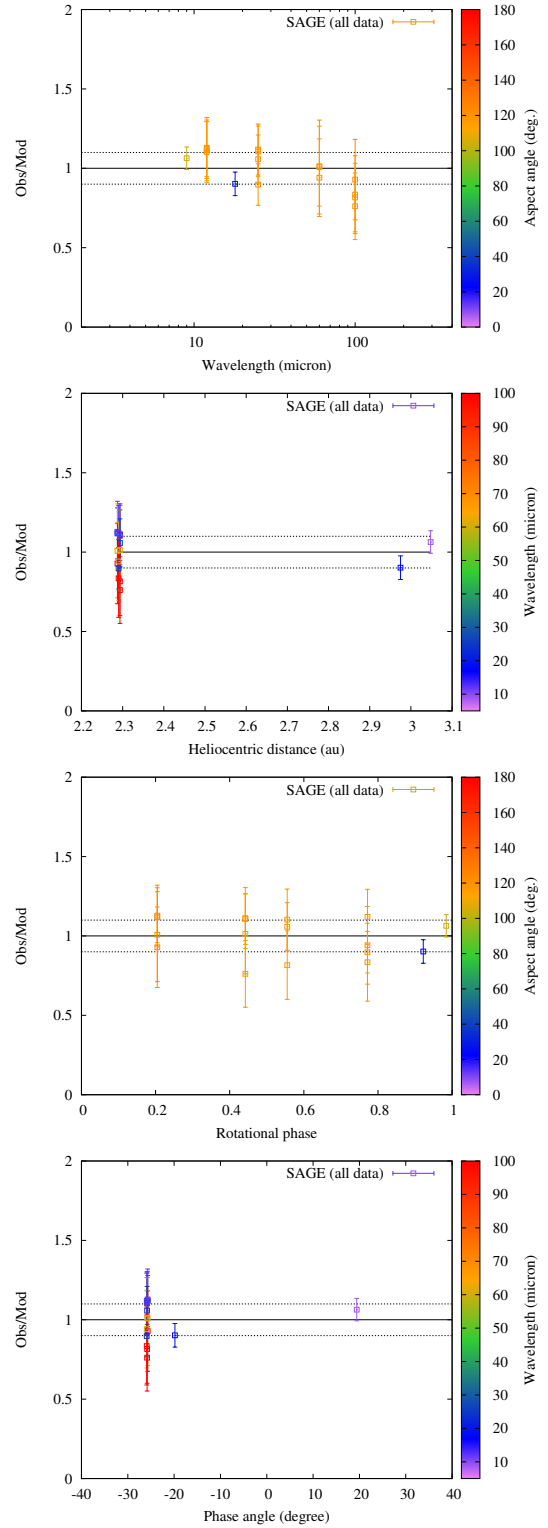


Fig. B.11. (145) Adeona.

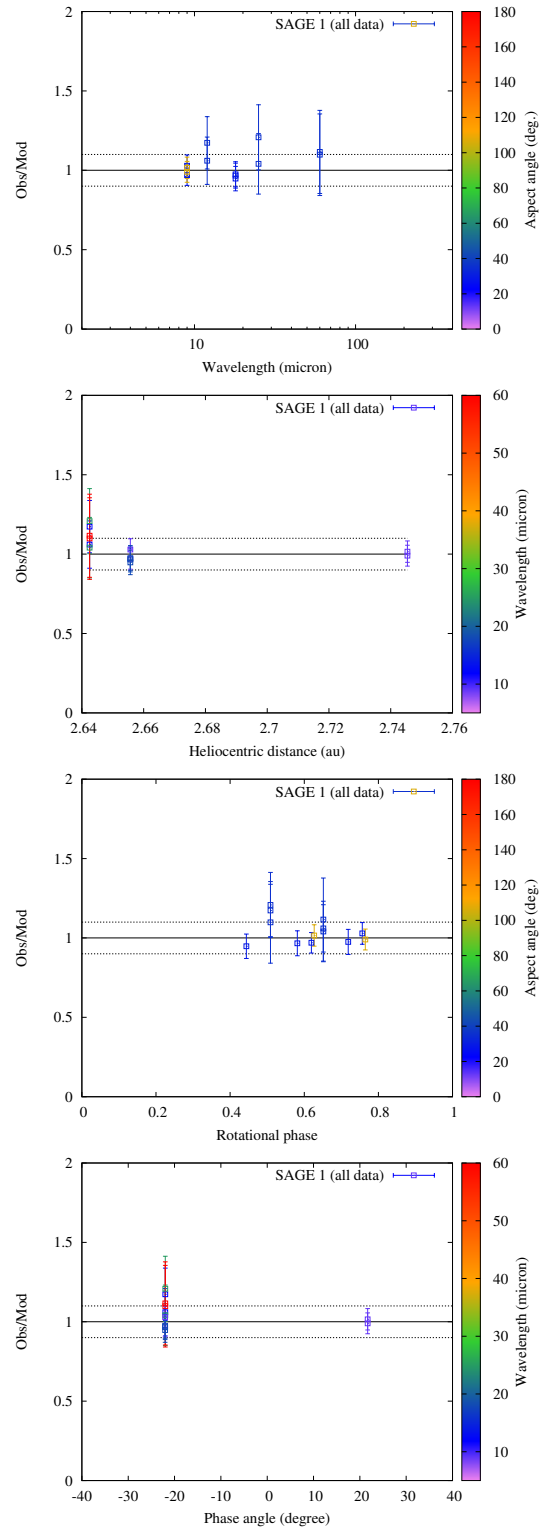
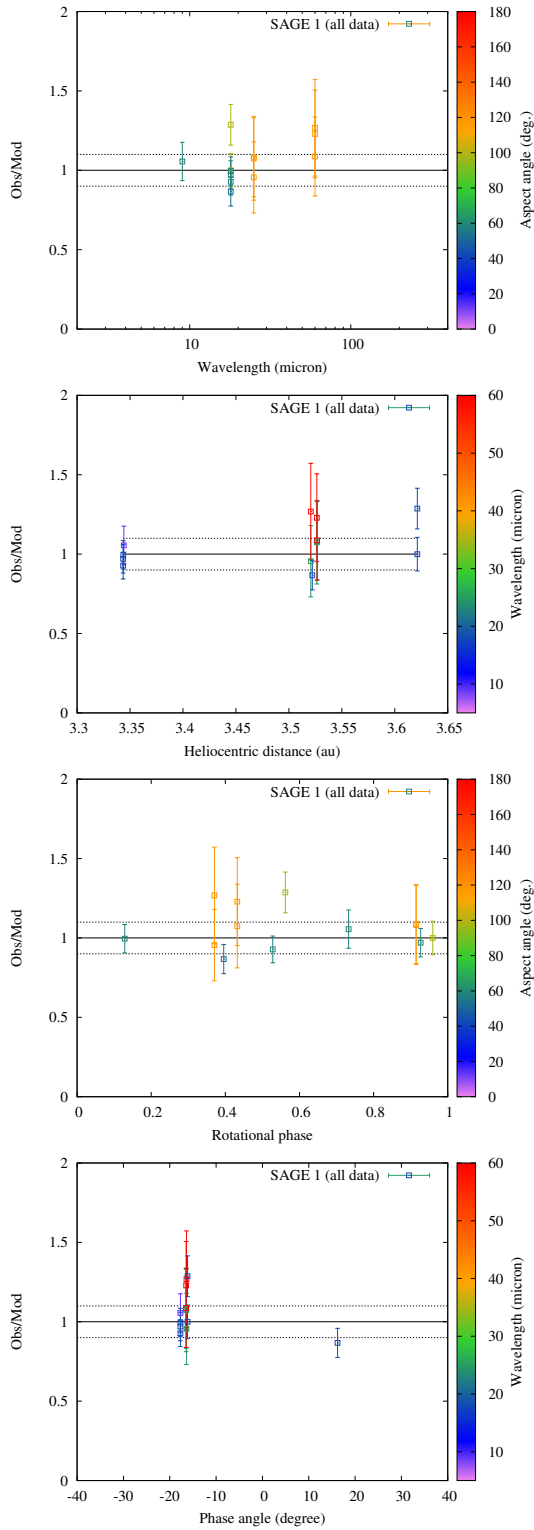


Fig. B.12. (297) Caecilia. There is not good phase angle coverage. There were not enough data to provide realistic error bars for the size. More thermal IR data are clearly needed.

Fig. B.13. (308) Polyxo.

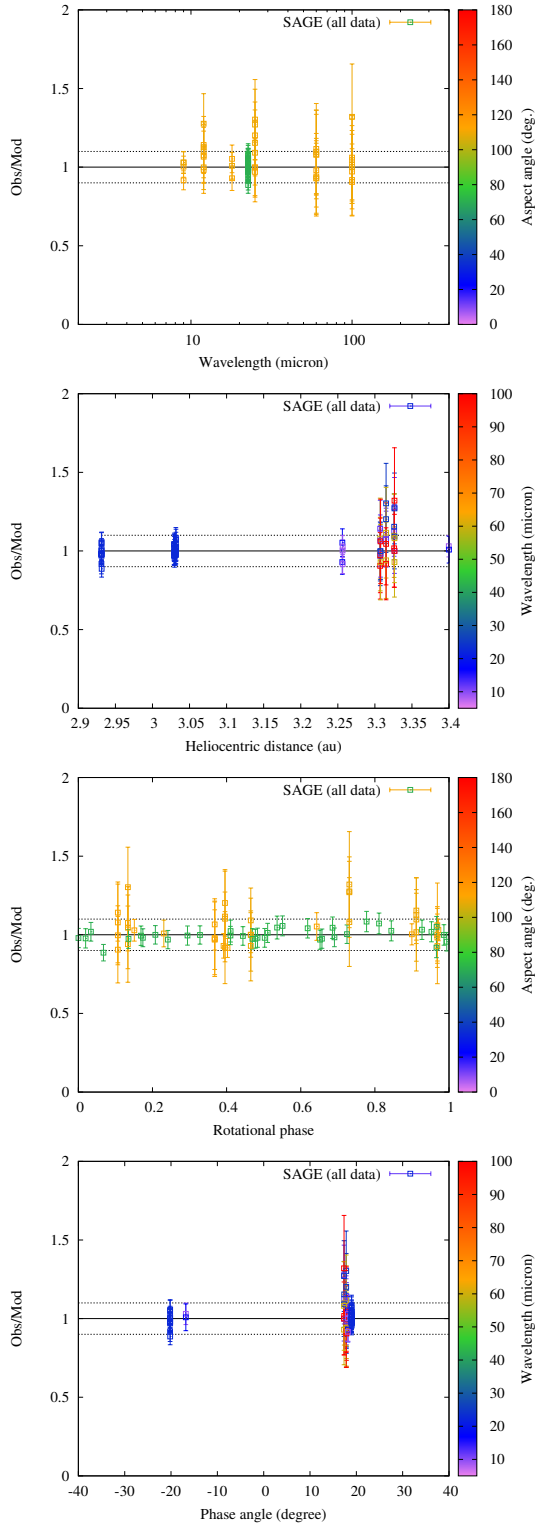


Fig. B.14. (381) Myrrha. There are some waves in the rotational phase plot that suggest small shape issues (see also Fig. B.2), but overall, the fit has a low χ^2 and is much better than the sphere with the same spin axis.

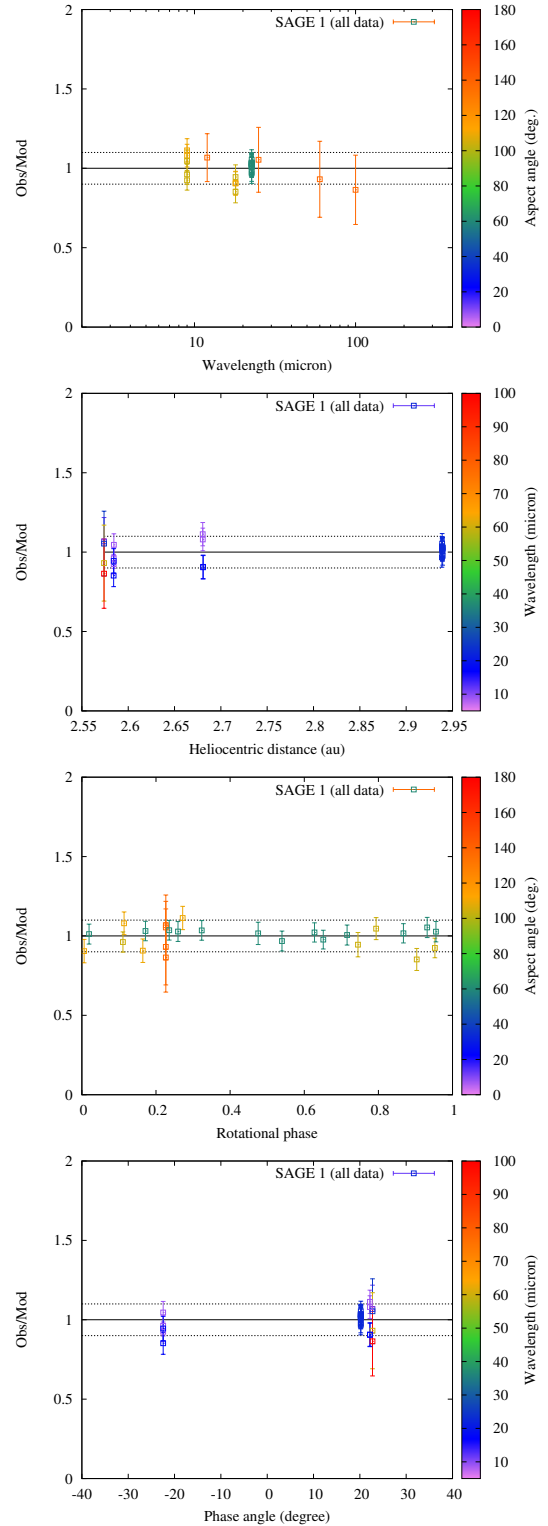


Fig. B.15. (441) Bathilde.

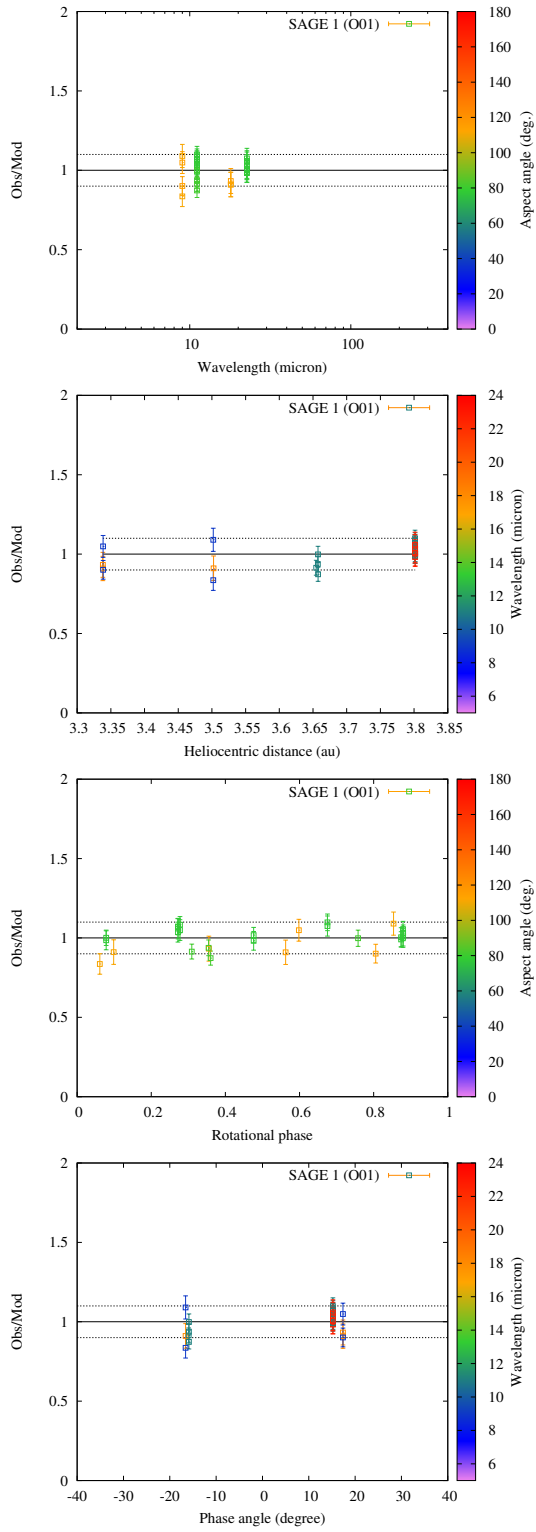


Fig. B.16. (721) Tabora.

Appendix C: Stellar occultation records fitting

In this section we present the model fit to stellar occultation chords.

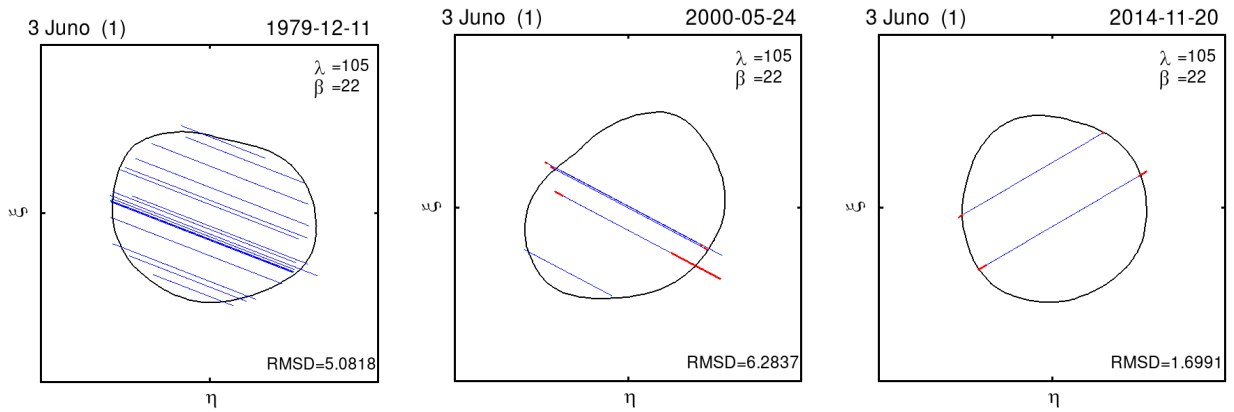


Fig. C.1. Shape model fitting to stellar occultations by 3 Juno.

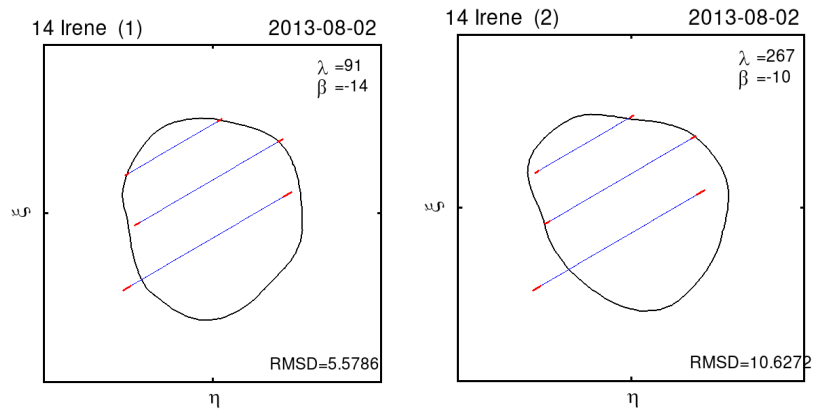


Fig. C.2. Shape model fitting to stellar occultations by 14 Irene.

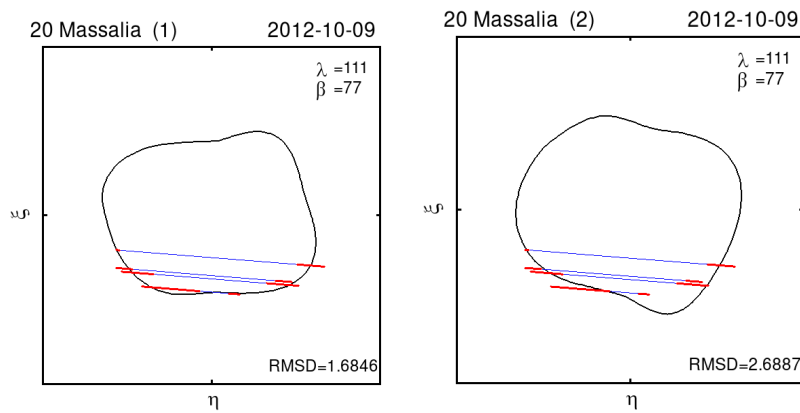


Fig. C.3. Shape model fitting to stellar occultations by 20 Massalia.

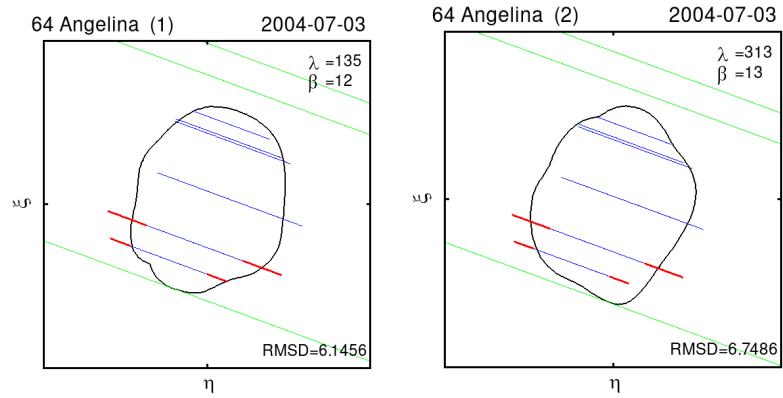


Fig. C.4. Shape model fitting to stellar occultations by 64 Angelina.

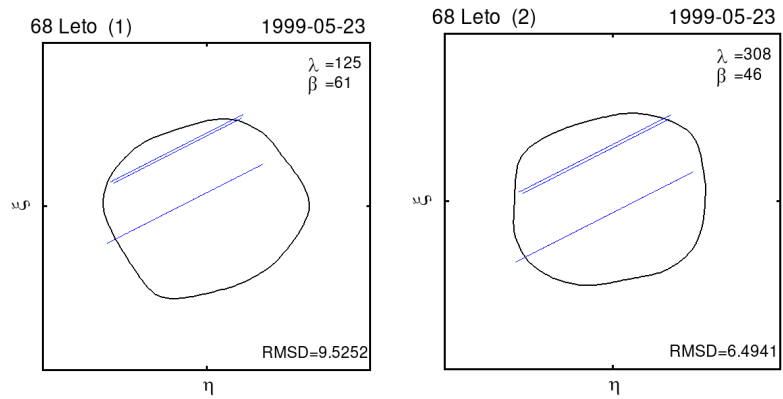


Fig. C.5. Shape model fitting to stellar occultations by 68 Leto.

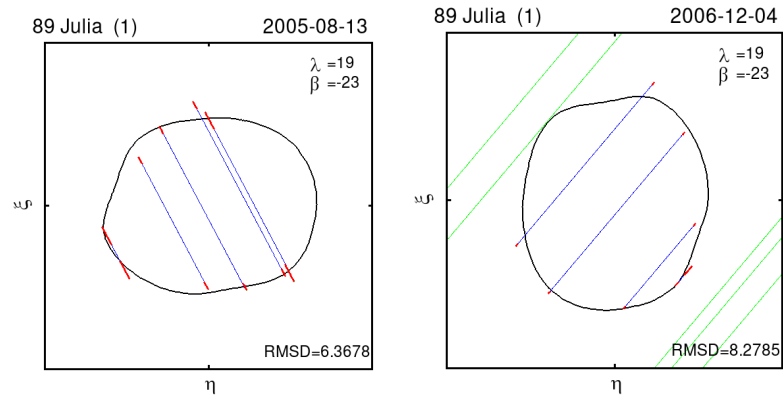


Fig. C.6. Shape model fitting to stellar occultations by 89 Julia.

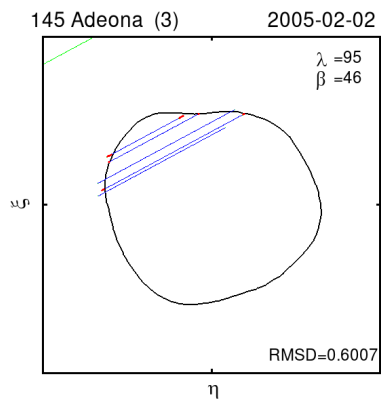


Fig. C.7. Shape model fitting to stellar occultations by 145 Adeona.

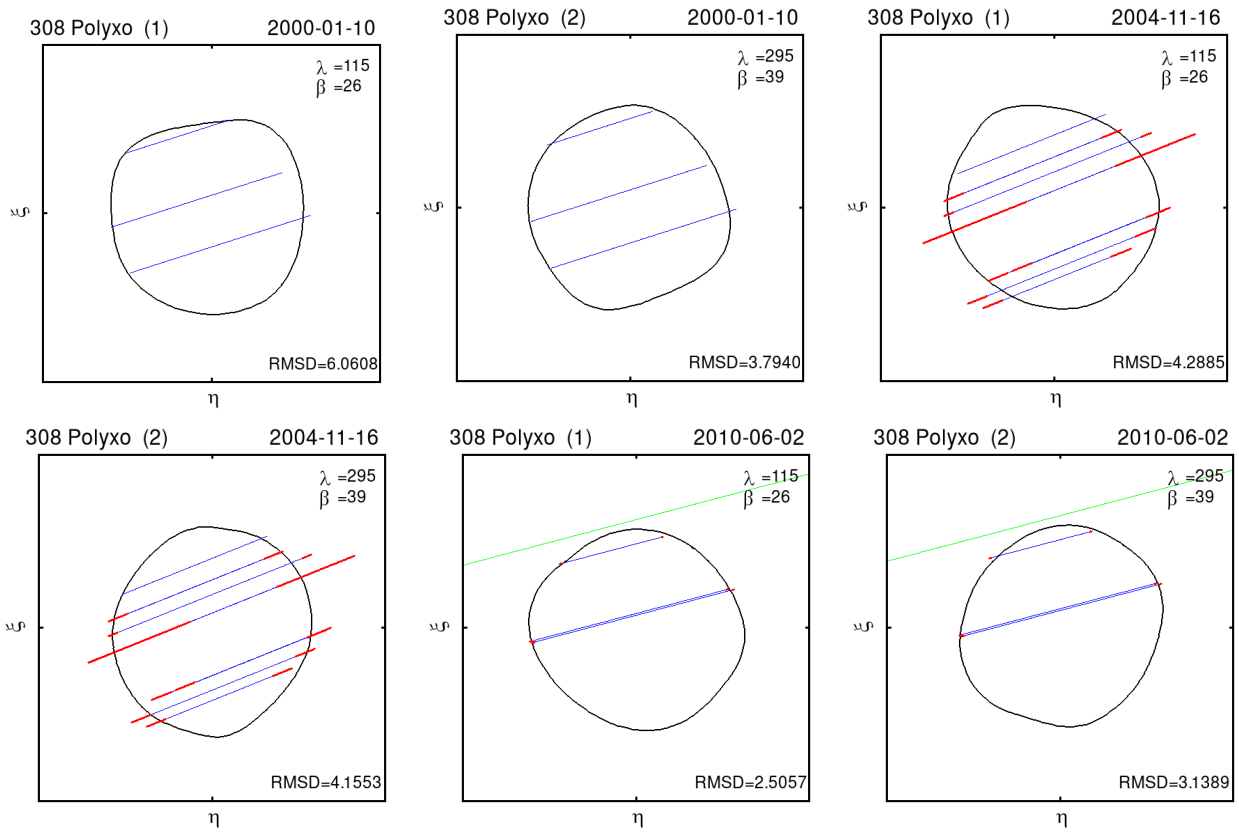


Fig. C.8. Shape model fitting to stellar occultations by 308 Polyxo.

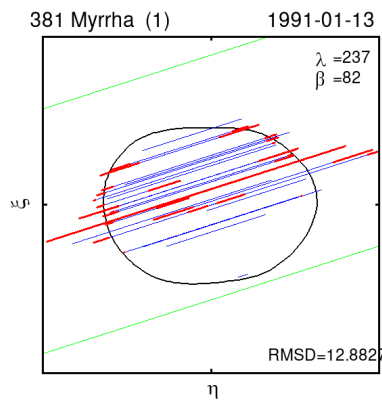


Fig. C.9. Shape model fitting to stellar occultations by 381 Myrrha.

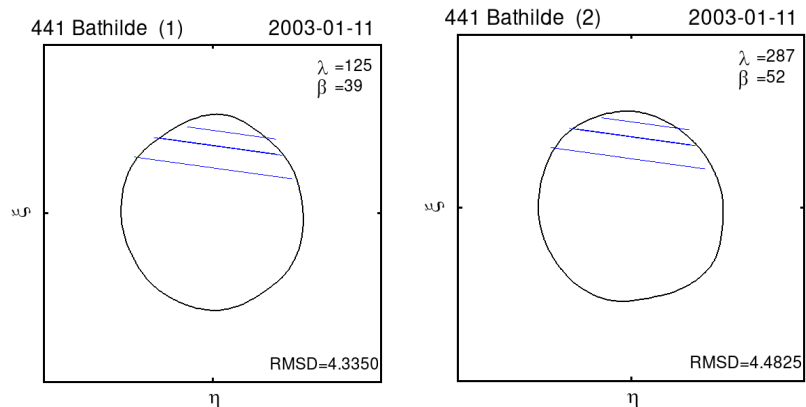
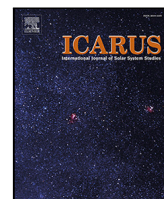


Fig. C.10. Shape model fitting to stellar occultations by 441 Bathilde.

Publication II



Research Paper

Investigating the most promising Yarkovsky candidates using Gaia DR2 astrometry[☆]

Karolina Dziadura^{*}, Dagmara Oszkiewicz, Przemysław Bartczak

Astronomical Observatory Institute, Faculty of Physics, A. Mickiewicz University, Stoleczna 36, 60-286 Poznań, Poland



ARTICLE INFO

Keywords:

Asteroids
Astrometry
Yarkovsky effect
Gaia
Dynamics
Celestial mechanics
Orbit determination

ABSTRACT

The Yarkovsky drift is a major factor driving the orbital evolution of asteroids. To date, the effect has been detected for a few hundred asteroids, mainly near-Earth objects. Before the start of the European Space Agency Gaia mission, the expectation was to recognize many other asteroids manifesting the Yarkovsky drift through the high precision and accuracy of the Gaia astrometry. In this work, we investigated the most promising Yarkovsky candidates indexed before the start of the mission. We found a reliable detection with signal-to-noise (SNR) ratio > 3 of the Yarkovsky effect (A2) for 12 asteroids. When compared to analytical theory from the literature using known (or assumed) orbital and physical parameters, we find that 7–10 (depending on the cutoff value) out of 12 asteroids with SNR > 3 are consistent with the estimated analytical drift values. In 17 cases, the resulting A2-parameter signal-to-noise was increased with the usage of the Gaia DR2 catalogue data, but no reliable detection can yet be claimed. We are certain that subsequent releases of the Gaia data will lead to numerous other detections. The Yarkovsky drift detection potential of the Gaia data is highlighted for asteroids such as (66391) Moshup (with a previously detected Yarkovsky drift) for which we noted a sizeable increase of the A2 signal-to-noise ratio from ~ 2.5 to ~ 13 when using the DR2 data compared to when using only the Minor Planet Center astrometry.

1. Introduction

The Yarkovsky effect was first proposed by Ivan Osipovich Yarkovsky in 1901 (Yarkovsky, 1901) and then the idea was popularized by Ernst Öpik (Öpik, 1951). The Yarkovsky effect causes secular changes in semi-major axis (a) over time (da/dt) caused by the reemission of heat, previously received from the Sun. The effect strongly depends on the distance to the Sun, albedo, size, and density of the object, out of which the density parameter is usually the most uncertain. Asteroid (6489) Golevka was the first object with empirical detection of the Yarkovsky effect (Chesley et al., 2003). Since then, the Yarkovsky effect has been discovered for various objects (Greenberg et al., 2020; Del Vigna et al., 2018; Farnocchia et al., 2013; Nugent et al., 2012; Chesley et al., 2008), however, it still remains difficult to detect for a large group of asteroids because of the need for accurate and precise astrometry over long arcs and multiple oppositions.

It has already been confirmed that this subtle nongravitational effect is crucial for understanding the dynamical evolution of the

Solar System. The Yarkovsky effect plays an important role in explaining meteorite delivery to Earth (Bottke Jr. et al., 2006), NEAs delivery (Vokrouhlický et al., 2000), distribution of asteroids in families (Nesvorný and Bottke, 2004), and impact monitoring (Farnocchia et al., 2015). For example asteroid 99942 Apophis was recently removed from the NASA Sentry Earth Impact Monitoring list,¹ as a result of refined orbit and the Yarkovsky effect ($A2 = 28.99 \pm 0.2510^{-15}$ AU d^{-2} Pérez-Hernández and Benet, 2022) determined based on new observations.^{2,3}

The Gaia mission's precise astrometry of asteroids was expected to improve the Yarkovsky effect detection and estimation for a large number of objects. Before the start of the mission, Mouret and Mignard (2011) indicated 74 most promising Yarkovsky candidates. In this work, we verify the detectability of the effect of those candidates with the most recent Gaia data release 2 (Gaia DR2) catalogue. From the 64 NEAs and 10 non-NEA objects listed in Mouret and Mignard (2011) as most promising Yarkovsky candidates, 42 had Gaia observations published in Gaia DR2. We estimate the empirical A2 (non-gravitational

[☆] This document is the result of the research project funded by the Ministry of Science and Higher Education, Poland.

^{*} Corresponding author.

E-mail address: karolinadziadura36@gmail.com (K. Dziadura).

¹ <https://cneos.jpl.nasa.gov/sentry/>.

² https://www.cosmos.esa.int/web/gaia/iow_20210329.

³ https://www.esa.int/Safety_Security/Planetary_Defence/Apophis_impact_ruled_out_for_the_first_time.

Table 1

Summary of observations used for orbit determination. The columns denote: asteroid number and name, date of the first and last observation, number of all observations, number of MPC records (satellite and ground based observations), number of radar observations and number of Gaia measurements. Column spec is SMASSII spectral taxonomic classification. Spectral type marked with * was taken from Tholen spectral type. Diameters and geometric albedos (p_V) were downloaded from the JPL Small Body Database. Assumed geometric albedos are denoted with a. Albedo marked with * was taken from Thomas et al. (2011). Diameters marked with C are determined from absolute magnitude and geometric albedo. Potentially Hazardous Asteroids are marked with the letter P. Binary systems are marked with the letter B.

Number	Name	First obs.	Last obs.	N_{total}	N_{MPC}	N_{radar}	N_{Gaia}	Diameter [km]	p_V	Spec
244	Sita	1885-01-09	2021-10-04	3840	3698	...	142	11.077 ± 0.022	0.256	Sa
1036	Ganymed	1924-10-23	2021-12-12	7367	7209	1	157	37.675 ± 0.399	0.238	S
1103	Sequoia	1928-11-09	2021-08-18	2914	2802	...	112	6.692 ± 0.078	0.384	Xk
1139 ^B	Atami	1929-12-01	2021-12-02	3144	3039	...	105	10.09^C	0.154^a	S
1620 ^P	Geographos	1951-08-31	2021-12-13	5144	5055	7	82	2.56 ± 0.15	0.290	S
1685 ^P	Toro	1948-07-17	2021-08-04	3781	3670	9	102	3.4	0.31	S
1747	Wright	1947-07-14	2021-11-30	2567	2434	...	133	6.35 ± 0.6	0.2005	Sl
1864	Daedalus	1971-03-24	2021-11-16	2683	2600	1	82	3.7	0.273	Sr
1866	Sisyphus	1955-01-26	2021-08-22	5217	5175	1	41	8.48	0.15	S
1943	Anteros	1968-06-03	2021-12-09	4611	4475	...	136	2.3	0.17	S*
2062	Aten	1955-12-17	2019-11-10	1059	983	7	69	1.1	0.26	Sr
2063	Bacchus	1977-04-24	2021-12-02	821	787	12	22	1.024 ± 0.020	0.203	Sq
2100	Ra-Shalom	1975-10-03	2021-12-02	2073	2030	10	33	2.3 ± 0.2	0.13	Xc
2629	Rudra	1954-01-05	2021-12-02	1909	1746	...	163	4.747 ± 1.056	0.066	B
3103	Eger	1982-01-20	2021-12-12	4004	3935	4	65	1.5	0.64	Xe
3200 ^P	Phaethon	1983-10-11	2021-12-13	6271	6145	8	118	6.25 ± 0.15	0.1066	B
3554	Amun	1986-03-04	2018-12-20	1729	1660	...	69	3.341 ± 0.021	0.074	
3753	Cruithne	1973-10-17	2021-11-08	1126	1085	...	41	2.071 ± 0.106	0.365	Q
3800	Karayusuf	1975-12-03	2021-11-25	4119	3964	...	155	1.624 ± 0.128	0.657	S
4769 ^P	Castalia	1989-08-01	2021-07-07	439	307	15	117	1.4	0.092	
4953 ^P		1974-07-21	2021-08-28	1075	1001	2	72	3.36^C	0.154^a	
5381 ^B	Sekhmet	1991-05-14	2017-03-16	480	383	1	96	0.935 ± 0.038	0.507	
5427	Jensmartin	1949-11-23	2021-11-28	2648	2539	...	109	3.158 ± 0.057	0.788	
6618	Jimsimons	1936-09-16	2021-12-03	2476	2396	...	80	11.506 ± 0.106	0.070	
7889		1977-08-10	2021-09-10	2124	2075	4	45	1.680 ± 0.070	0.452	V
10563	Izhdubar	1991-11-13	2021-07-02	648	614	...	34	1.53^C	0.2*	Q
12711	Tukmit	1991-01-12	2021-12-13	1651	1611	3	37	2.24^C	0.154^a	Sr
66146		1982-12-04	2021-12-11	1625	1557	...	68	2.864 ± 1.165	0.224	
66391 ^{PB}	Moshup	1998-05-29	2021-08-22	4289	4228	37	24	1.317 ± 0.040	0.154^a	S:
68216 ^P		1995-05-28	2021-12-05	2245	2216	5	24	0.994 ± 0.042	0.449	
85818		1993-05-24	2021-10-23	870	791	...	79	2.028 ± 0.018	0.168	S
86667		1988-05-11	2020-06-17	1636	1585	...	51	0.745 ± 0.023	0.349	
87684 ^P		1977-10-07	2021-11-13	1565	1405	...	160	2.05^C	0.154^a	
88710 ^B		1954-11-27	2016-01-04	1115	1007	...	108	0.760 ± 0.200	0.281	
96590		1992-01-01	2019-11-12	2491	2461	15	15	0.882 ± 0.217	0.489	S:
105140		1952-09-17	2021-12-12	2436	2387	...	49	1.946 ± 0.059	0.223	
137805		1999-12-28	2021-12-12	1501	1462	...	39	2.243 ± 0.026	0.027	X
137925		1953-12-07	2021-11-09	1729	1600	...	129	1.372 ± 0.068	0.373	Q
154555		2003-03-07	2021-12-12	1150	1007	...	143	1.59^C	0.154^a	
163693 ^B	Atira	2003-02-11	2021-03-09	662	639	2	21	1.87^C	0.154^a	
163899 ^P		2000-01-06	2021-12-05	1385	1324	15	46	0.791 ± 0.025	0.340	
164121 ^{PB}		1982-11-19	2019-06-25	1180	1118	8	54	1.717 ± 0.550	0.198	

acceleration) parameter for all 42 asteroids and discuss its reliability. Moreover, for the comparison with the literature, we derived da/dt values from A2.

In Section 2, we discuss the data used in this study. In Section 3, we describe the methodology of orbit and Yarkovsky determination including the influence of various weighting schemes. In Section 4, we present our results obtained using 3 different methods. Additionally, we compared the da/dt values determined in this work, based on astrometry, with the literature and with the expected values determined from asteroid properties. In Section 5, we summarize the results.

2. Data

We have used all optical, radar and Gaia data available on 15 December 2021. In Table 1, we summarize the data utilized for each asteroid.

First, we have downloaded all measurements available in the Minor Planet Center (MPC) for the studied objects. The typical accuracy of the majority of ground-based astrometry is considered around 0.5–1.0 arcseconds (Farnocchia et al., 2015), while for Gaia the along-scan (AL) uncertainties are of the order of 1 mas and the across-scan (AC) uncertainties are of the order of 600 mas (Spoto et al., 2018). Individual uncertainties are included in least-squares weight matrix.

The MPC data also contains some radar measurements (round-trip time in microseconds and Doppler shift in Hz). Additional radar measurements were extracted from the Jet Propulsion Laboratory (JPL) database.⁴ The MPC data is provided in the MPC 1992 80-column format,⁵ which does not include, for example, information on random and systematic uncertainties of right ascension (RA) or declination (Dec). Therefore, in July 2018 Minor Planet Center announced ADES (Astrometry Data Exchange Standard⁶) as the preferred format for astrometric observations. This new format was previously ratified by IAU Commission 20 at the IAU General Assembly held in Hawaii (USA) in August 2015. We have performed computations using both formats.

Furthermore, we have supplemented the MPC data with observations obtained from the Gaia DR2. The DR2 measurements are provided in an independent format⁷ that we have translated into both the 80-column and ADES formats. The translation into the 80-column format is straightforward, with one exception — due to the fact that

⁴ <https://ssd.jpl.nasa.gov/sb/radar.html>.

⁵ <https://www.minorplanetcenter.net/iau/info/OpticalObs.html>.

⁶ <https://www.minorplanetcenter.net/iau/info/ADES.html>.

⁷ https://gea.esac.esa.int/archive/documentation/GDR2/Gaia_archive/chap_datamodel/sec_dm_sso_tables/ssec_dm_sso_observation.html#sso_observation-solution_id.

Table 2

Relation of the DR2 keywords to the ADES format keywords. The rmsRA, rmsDec rmsCorr values are derived from the sum of random and systematic covariance matrices.

Gaia DR2	ADES
number_mp	permID
epoch_utc [day]	obsTime [iso 8601 format]
ra [deg]	ra [deg]
dec [deg]	dec [deg]
ra_error_random [mas], ra_error_systematic [mas]	rmsRA [arcsec]
dec_error_random [mas], dec_error_systematic [mas]	rmsDec [arcsec]
ra_dec_correlation_random, ra_dec_correlation_systematic	rmsCorr

the Gaia catalogue provides only barycentric ICRS Gaia positions, we have transformed it into geocentric Gaia positions (as required in the 80-column format) using the barycentric Earth position applying ephemeris DE431. In the 80-column format, it is not possible to include astrometric uncertainties and more general error covariance matrices. Thus, following the error model of Farnocchia et al. (2015) uncertainties of 0.01 arc second in both RA and Dec are assumed for Gaia observations. Those uncertainties are assumed uncorrelated. Therefore, the orbit computation based on this format assumes larger error ellipses for the astrometric measurements than those that would result from the actual covariance matrices in DR2. Thus, orbit computation based on this format does not take full advantage of the Gaia precision and accuracy.

To translate the data into the ADES format, we have first used the MPC-recommended software available on Github.⁸ Next, we used our own software to translate the DR2 data into ADES format and merged the data. The rmsRA, rmsDec, and rmsCorr values are computed from the sum of random and systematic covariance matrices of the Gaia data to include both types of errors. Systematic errors are usually 2 orders of magnitude smaller than the random ones. Relation of the DR2 keywords to the ADES format keywords is provided in Table 2. The description of the other keywords used for Gaia observations is presented in the Table 3.

The Gaia along scan (AL) position of an asteroid is taken from the astrometric field CCD of Gaia and the across scan (AC) position only from the sky mapper CCD. Since Gaia was designed for stellar astrometry, there is no tracking of asteroids, which in contrast to stars, can also move vertically in the astrometric field of Gaia. Asteroid AC positions are not measured in that field, thus growing uncertainty of the AC position during transit. The uncertainty of asteroid astrometry can be represented by an ellipse that is extremely stretched in the across scan direction. This is demonstrated in Fig. 1 where we present the AL and AC residuals for the asteroid (5427) Jansmartin. Those residuals were obtained using a rotation from the plane of the sky-plane residuals to the plane of the residuals in the Gaia coordinate system (by a position angle minus 90°). Following the AL and AC positional correlation, the uncertainties of Gaia RA, and Dec measurements for asteroids are also highly correlated. In Fig. 2 we show the RA and Dec residuals for the same asteroid. Each transit is marked with different symbols and colors. Residuals of observations taken at the beginning of the transit are closer to the origin of the plot than those taken later in the transit. This is due to the growing uncertainty in the AC direction that is translated into the RA, Dec uncertainty. Due to the high correlation, it is highly recommended to use a full covariance matrix of the Gaia measurements (Spoto et al., 2018). Processing data in the ADES format allows to take full advantage of the Gaia accuracy by utilizing the full observational covariance matrix (the systematic and random error of RA and Dec, and correlation between them).

⁸ https://github.com/IAU-ADES/ADES-Master/blob/master/ades_master.pdf.

Table 3

ADES keywords values.

ADES	Description
mode	CCD
stn	258 (Gaia)
sys	ICRF_AU
ctr	399 (geocenter)
pos1,pos2,pos3	Rectangular coordinates of Gaia

3. Methods

We have used the empirical approach to detect the Yarkovsky effect, which has been validated before in the literature (Farnocchia et al., 2013; Del Vigna et al., 2018; Greenberg et al., 2020). In particular, to the available astrometric, radar and Gaia observations, we fit a least-square orbit with an additional parameter (6 orbital elements plus the non-gravitational A2 parameter) using the Orbit software (Milani and Gronchi, 2010).⁹ The corresponding transverse acceleration $\mathbf{a}_t = A_2 g(r) \hat{\mathbf{t}}$ is assumed to be directly related to the secular drift in semi-major axis caused by the Yarkovsky effect and $g(r)$ is a function of r heliocentric distance of the asteroid. Following Farnocchia et al. (2013), we use $g(r) = r^{-2}$ for all asteroids. As $\mathbf{a}_t = A_2 g(r) \hat{\mathbf{t}}$ is the transverse acceleration, the corresponding secular drift in semi-major axis da/dt can be estimated from Gauss variational equations as derived by Farnocchia et al. (2013). The force model includes gravitational acceleration from the Sun, eight planets, the Moon (according to the JPL planetary ephemeris DE431), 16 most massive asteroids, and Pluto. The relativistic effects from the Sun, the planets, and the Moon are included.

We used the debiasing and weighting scheme developed by Farnocchia et al. (2015) for all objects. That debiasing and weighting scheme resolves the issue of systematic errors caused by inaccurate stellar positions and proper motions in stellar catalogues used for calibrating asteroid astrometry. Furthermore, weighting rules are derived based on the catalogue used for astrometry, date and type (CCD, photographic, satellite, etc.) of the observation, and the observatories where the observation was conducted. Generally, the debiasing and weighting procedure is twofold. First, the influence of the stellar catalogue biases is removed by simply subtracting the corrections in RA and Dec depending on the stellar catalogue and sky position. Second, the weights derived by Farnocchia et al. (2015) for different observatories, observation types, stellar catalogue, date range are directly utilized in the weight matrix during the weighted least-squares optimization. Overall, three weighting models are available directly in the current version of OrFit. The model of Vereš et al. (2017) is optimized for newly discovered NEOs with short observing arcs. Two others developed by Farnocchia et al. (2015) and Chesley et al. (2010) were created for well-observed asteroids. The scheme of Farnocchia et al. (2015) is based on the solutions from Chesley et al. (2010) with a few modifications. In contrast to Chesley et al. (2010), the work of Farnocchia et al. (2015) also considered proper motion errors, used the PPMXL catalogue as a reference (a more accurate subset of the 2MASS catalogue), had a larger sample size and included more stellar catalogues. Thus, finally, we decided to use the weighting scheme of Farnocchia et al. (2015). Nonetheless, we have assessed the influence of the three weighting models (Vereš et al., 2017; Farnocchia et al., 2015; Chesley et al., 2010) on the computed A2 values. To test the weighting models, we applied each model to the astrometry for four asteroids (Golevka, Bennu, Bacchus, and 1992 BF) with a known, well determined Yarkovsky drift and concluded that the resulting A2 values are similar (typically within 1- σ uncertainties) for all weighting schemes available in OrFit. Furthermore, for the four considered asteroids, the results were stable,

⁹ <http://adams.dm.unipi.it/orbit/>.

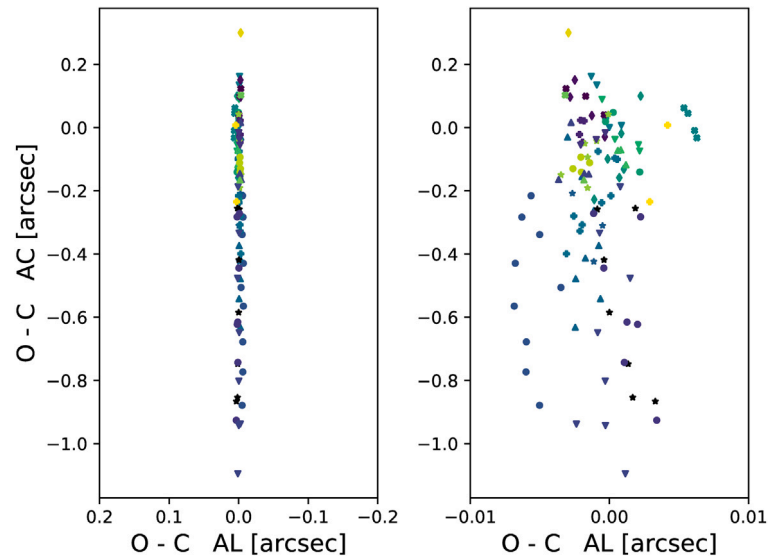


Fig. 1. Post-fit residuals in the AL, AC-scan directions for asteroid (5427) Jansmartin. Colored markers denote different Gaia transits. The right panel is a zoom-in of the residuals. (For interpretation of the references to color in this figure legend, the reader is referred to the web version of this article.)

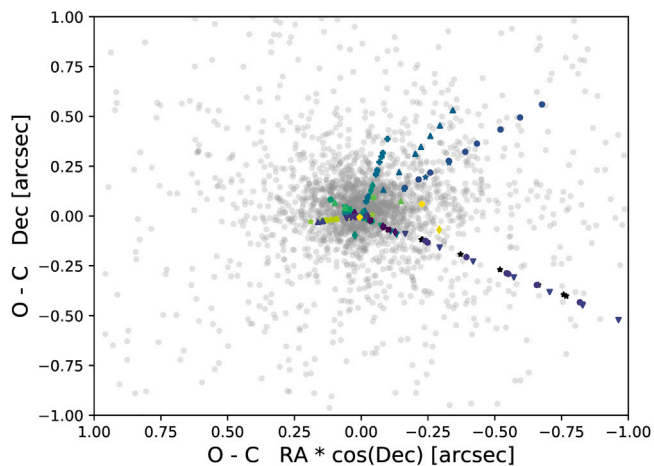


Fig. 2. Post-fit residuals in RA, Dec for asteroid (5427) Jansmartin. Colored markers denote different Gaia transits and the gray dots are the residuals of the MPC observations. (For interpretation of the references to color in this figure legend, the reader is referred to the web version of this article.)

independent of whether outlier rejection was used. OrbFit has an automatic rejection algorithm. During each iteration of the differential corrections, all observations with $\text{Chi} > \sqrt{10}$ are rejected, but then they can be recovered in the next fit iteration if $\text{Chi} < \sqrt{9.21}$.

4. Results

We estimated the A_2 parameter for 42 candidates from [Mouret and Mignard \(2011\)](#) with Gaia DR2 astrometry. The results are listed in [Table 4](#). The three segments of columns represent the A_2 estimation and its corresponding signal-to-noise (SNR) based on various data and format types. The results in the first segment were obtained using MPC astrometry only, the subsequent two segments are based on the MPC and Gaia DR2 astrometry (using 80-column and ADES formats respectively). The ADES format includes the observational covariance matrix, thus taking full advantage of the Gaia precision and accuracy. The secular drift in semi-major axis da/dt in the last column is derived from the A_2 (ADES+DR2) parameter as in [Farnocchia et al. \(2013\)](#).

For 12 out of the 42 asteroids, the SNR_{A_2} value (defined as the A_2 value divided by its uncertainty) is higher than 3, which we consider the detection limit. Almost no Gaia observations were rejected when using a full covariance matrix of Gaia observations ([Table 4](#)).

For comparison, we listed the da/dt parameters from the literature, if available in [Table 4](#) and presented it in [Fig. 3](#). Our results are consistent with the literature except for (10563) Izhdubar. Thus, we investigated the A_2 value for the asteroid (10563) Izhdubar using the same observations as in [Greenberg et al. \(2020\)](#) and [Nugent et al. \(2012\)](#) and found a positive value as in the literature. However, when using all observations available up to date, we obtain $da/dt = -7.36 \pm 2.3110^{-4}$ AU My $^{-1}$ and $\text{SNR}_{A_2} > 3$ while the literature is $\text{SNR}_{A_2} \sim 2.2$. Since the publication of [Greenberg et al. \(2020\)](#) the observational arc for that object has increased over 2 years. Overall, we conclude that our estimation is more reliable.

We found a few asteroids for which we see a significant improvement in the SNR_{A_2} up to > 3 when using Gaia data. A good example is (10563) Izhdubar, for which we found an SNR_{A_2} improvement from 2.02 to 3.51 after adding only 34 Gaia observations. For (105140) and (1620) Geographos, we also see an SNR_{A_2} improvement after adding the Gaia data from ~ 2.5 to ~ 3.5 . Another great example is the asteroid (66391) Moshup, which is a Potentially Hazardous and binary object. Without the Gaia data, we obtain $A_2 = -5.31 \pm 2.04 \cdot 10^{-15}$ AU d $^{-2}$ where $\text{SNR}_{A_2} = 2.6$, similar to the literature. However, when we derive the A_2 value including ground-based and Gaia observations, we note a major decrease in the uncertainty, therefore, an increase of $\text{SNR}_{A_2} = -4.83 \pm 0.36 \cdot 10^{-15}$ AU d $^{-2}$, $\text{SNR}_{A_2} = 13.42$. This is the highest SNR_{A_2} in this work. Detecting the Yarkovsky effect for those 4 objects with $\text{SNR}_{A_2} > 3$ would not be possible without the Gaia data.

For all objects with $\text{SNR}_{A_2} > 3$, we detected a negative A_2 value which correspond to the number of retrograde rotators N_r . Most of the presented objects in this work are implied to be retrograde rotators, in agreement with the expected preponderance of retrograde rotators (N_r) over prograde rotators (N_p) in the literature ($N_r/N_p = 2.7$ [Greenberg et al., 2020](#), $N_r/N_p = 2 - 0.7 +1$ [La Spina et al., 2004](#) $N_r/N_p = 2.9 \pm 0.7$ [Greenberg et al., 2017a](#) $N_r/N_p = 2.5 \pm 0.1$ [Nugent et al., 2012](#) $N_r/N_p = 4$ [Farnocchia et al., 2013](#)).

We compared our empirical estimations of the Yarkovsky effect with the expected values based on the physical and orbital properties of the studied objects using the formulas derived by [Greenberg et al. \(2020\)](#), [Spoto et al. \(2015\)](#) and [Del Vigna et al. \(2018\)](#). [Greenberg et al. \(2020\)](#) derived orbit-averaged da/dt values based on a force model

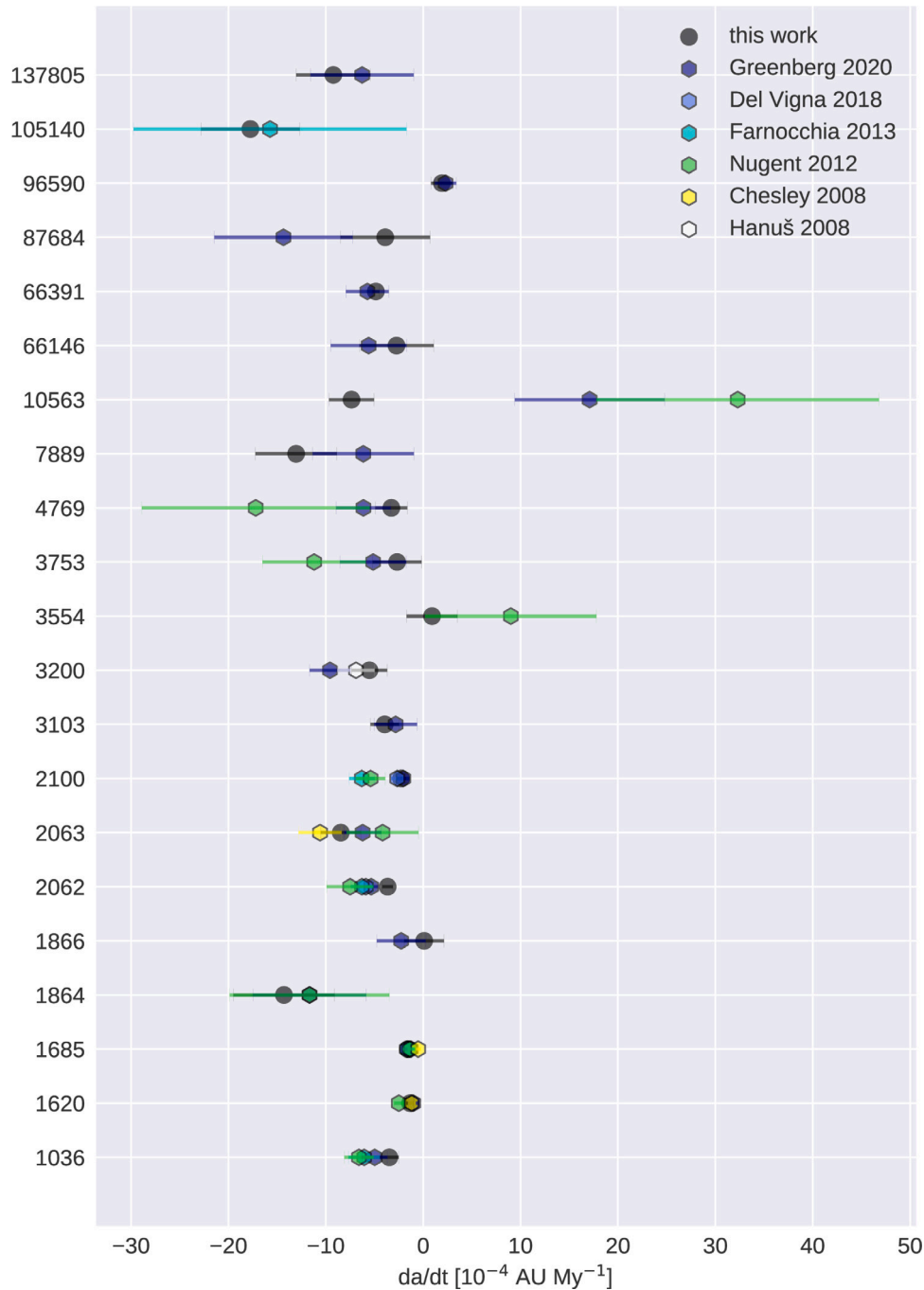


Fig. 3. A comparison of our Yarkovsky detections (black — this work) and those determined by Greenberg et al. (2020), Del Vigna et al. (2018), Farnocchia et al. (2013), Nugent et al. (2012), Chesley et al. (2008) and Hanuš et al. (2018). Note that we determined da/dt value using different data sets described in Section 2.

described in Greenberg et al. (2017b). Spoto et al. (2015) and Del Vigna et al. (2018) calibrated the expected drift value in relation to that of the asteroid (101955) Bennu, which has the best and most reliable Yarkovsky detection. We quote the equations below for convenience.

The expected Yarkovsky drift as estimated by Greenberg et al. (2020):

$$\langle da/dt \rangle_{\text{exp}} = \pm 14.4 \left(\frac{\xi}{0.1} \right) \left(\frac{1 \text{AU}}{a} \right)^{\frac{1}{2}} \left(\frac{1}{1-e^2} \right) \left(\frac{1 \text{km}}{D} \right) \left(\frac{1000 \text{ kg m}^{-3}}{\rho} \right) \times \frac{10^{-4} \text{AU}}{\text{My}} \quad (1)$$

and Spoto et al. (2015) and Del Vigna et al. (2018):

$$\langle da/dt \rangle_{\text{exp}} = (da/dt)_B \times \left(\frac{\sqrt{a_B(1-e_B^2)}}{\sqrt{a}(1-e^2)} \right) \left(\frac{D_B}{D} \right) \left(\frac{\rho_B}{\rho} \right) \left(\frac{\cos \phi}{\cos \phi_B} \right) \times \left(\frac{1-A}{1-A_B} \right). \quad (2)$$

Where ξ is the efficiency of the Yarkovsky effect, a is the orbit semi-major axis, e is eccentricity, D is diameter, ρ is density, ϕ is obliquity, A is Bond albedo and the values denoted with B are (101955) Bennu properties (Table 5).

Both of those equations depend on the object's density, which is typically not known. We assumed density values as in Carry (2012) based on the object spectral type, presented in Table 6. Additionally, for

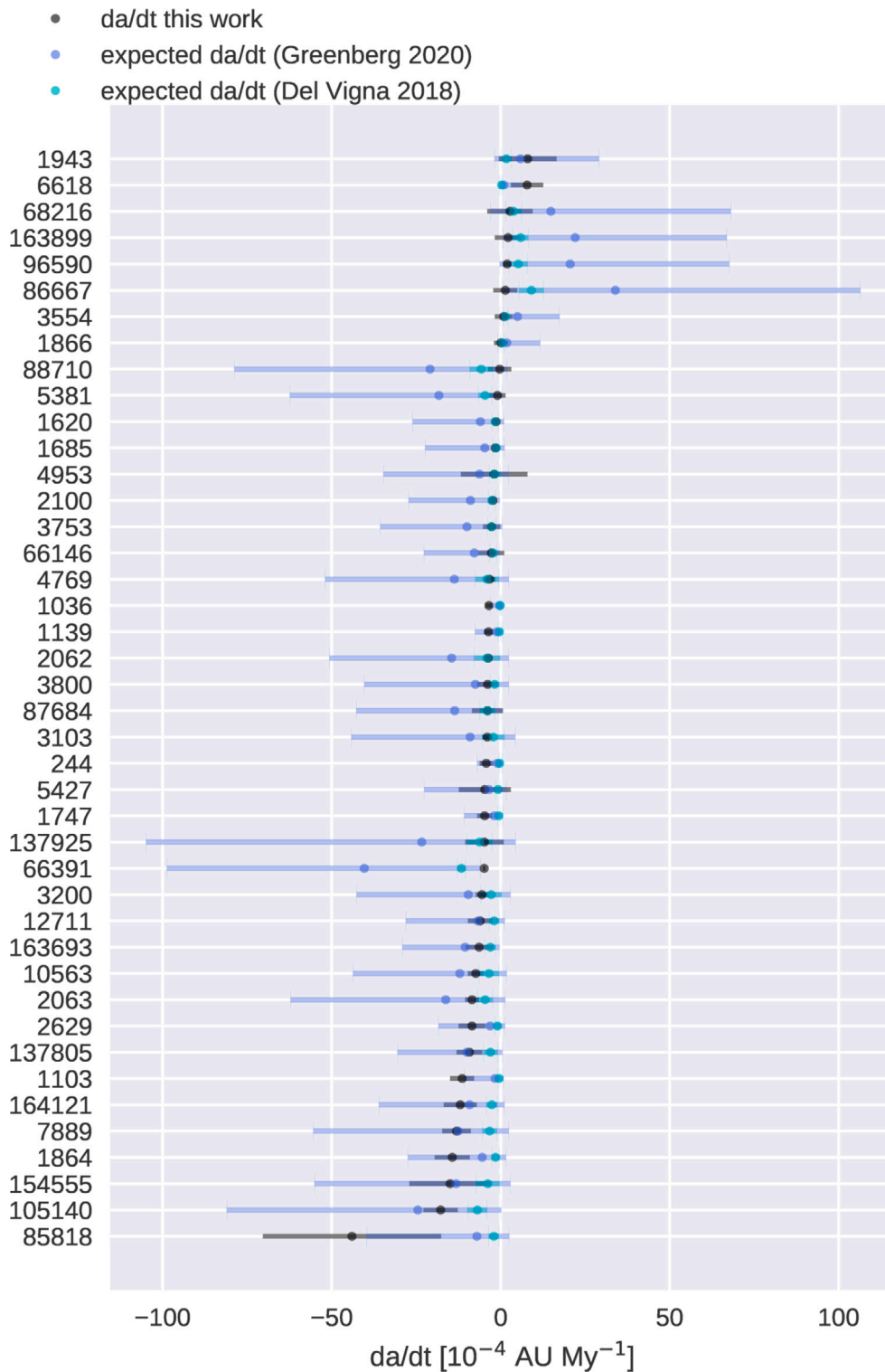


Fig. 4. Yarkovsky parameter results for all 42 asteroids presented in this work in comparison to expected values. Black — this work, dark blue — expected value of da/dt with uncertainties determined as in Greenberg et al. (2020) where the circle is at the value for efficiency $\xi = 0.12$, light blue — expected value of da/dt with uncertainties determined as in Spoto et al. (2015) and Del Vigna et al. (2018). Objects are ranked from the most positive to the most negative Yarkovsky drift rate. (For interpretation of the references to color in this figure legend, the reader is referred to the web version of this article.)

asteroid (66391) Moshup we used $\rho = 1.80 \pm 0.29$ [g/cm³] (Carry, 2012) and for (1620) Geographos we used $\rho = 2.10^{+0.55}_{-0.45}$ [g/cm³] (Rozitis and Green, 2014). As Q type asteroids are considered space-weathered Sq/S type we assumed the same density as in S type (Binzel et al., 2010). Most of NEAs are S types (Binzel et al., 2019), so if the spectral type was not available for the objects, density for S type was assumed. If

the diameter of a studied object was not available in JPL Small Body Database, we derived it from the absolute magnitude and geometric albedo (Greenberg et al., 2020, Eq. 13). Diameters and albedos are presented in Table 1. For objects with unknown geometric albedo parameter, we assumed $p_V = 0.154$ (Del Vigna et al., 2018).

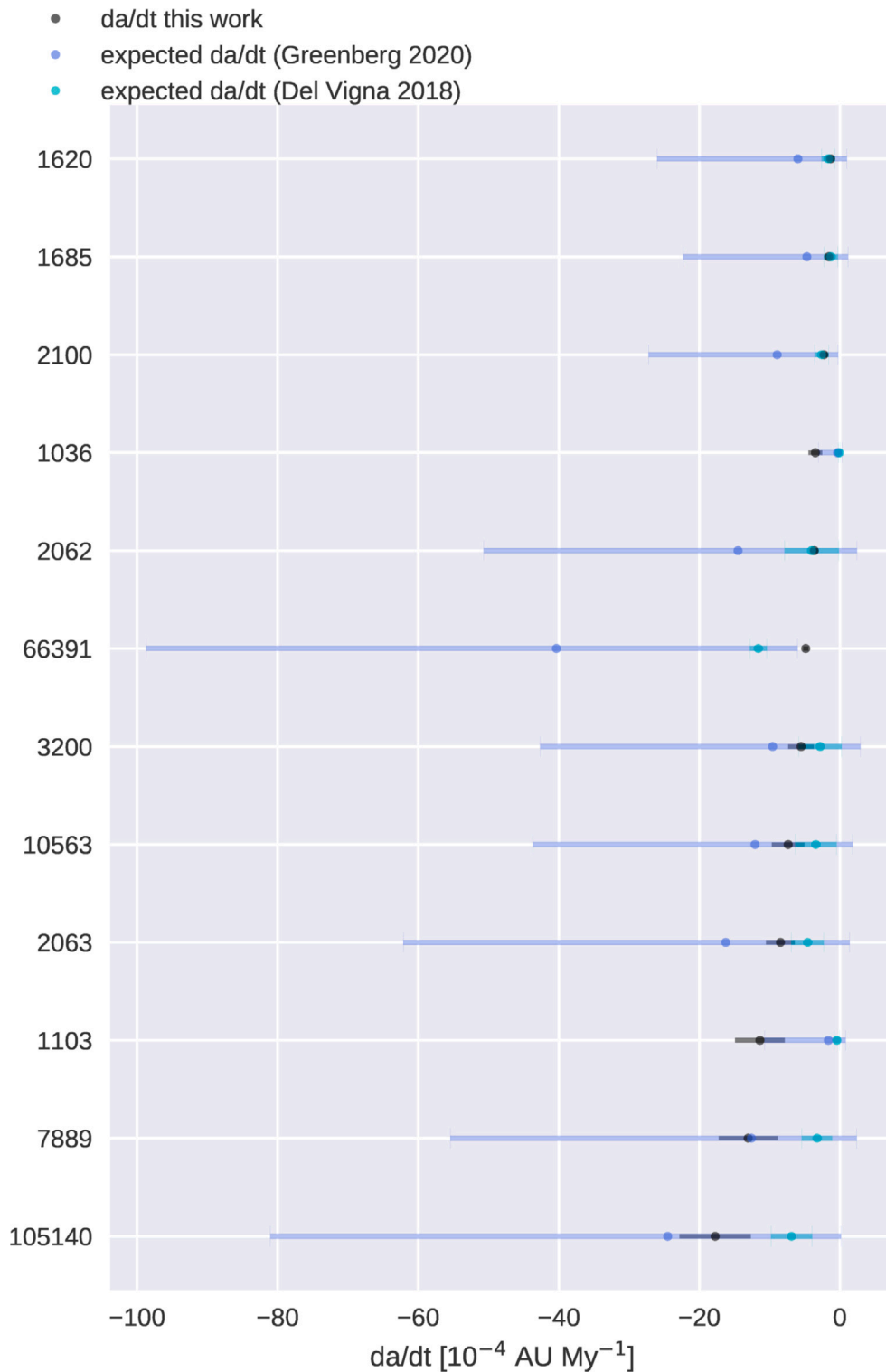


Fig. 5. Yarkovsky parameter results for asteroids with $SNR_{A_2} > 3$ in comparison to expected values. Black — this work, dark blue — expected value of da/dt with uncertainties determined as in Greenberg et al. (2020) where the circle is at the value for efficiency $\xi = 0.12$, light blue — expected value of da/dt with uncertainties determined as in Spoto et al. (2015) and Del Vigna et al. (2018). Objects are ranked from the most positive to the most negative Yarkovsky drift rate. (For interpretation of the references to color in this figure legend, the reader is referred to the web version of this article.)

We present the expected da/dt values and their uncertainties, which have been determined with the two methods (Spoto et al., 2015; Del Vigna et al., 2018; Greenberg et al., 2020) as compared to the empirical values derived in this work in Figs. 4, 5. Fig. 5 is for objects with $SNR_{A_2} > 3$. For all objects, the estimated da/dt is within the

possible expected values (assuming Yarkovsky drift efficiency ξ from 0 to 1).

In Figs. 6, 7, we present a comparison of the empirically derived da/dt values to those of the expected theoretical Yarkovsky drift values for all the 42 objects. We compute the ratio $S = \left| \frac{(da/dt)_{\text{this work}}}{(da/dt)_{\text{exp}}} \right|$ as

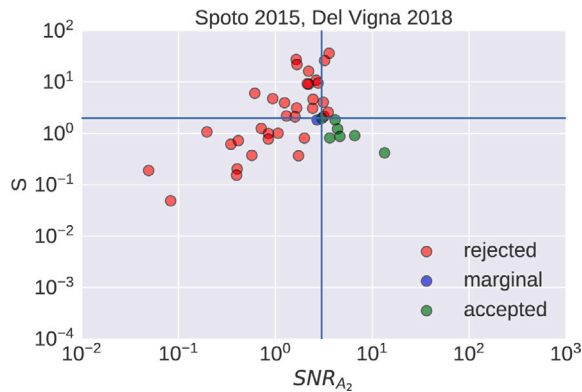


Fig. 6. S parameter as a function of signal to noise ratio SNR_{A2} . Green circles represents accepted values ($SNR_{A2} > 3$ and $S < 2$) - consistent with expected value determined as in Spoto et al. (2015) and Del Vigna et al. (2018), blue circles are marginal cases with $2.5 < SNR_{A2} < 3$ and $S < 2$, and red are values with $SNR_{A2} > 3$ or $S > 2.5$. Horizontal line represents $S = 2$. Vertical line represents $SNR_{A2} = 3$. (For interpretation of the references to color in this figure legend, the reader is referred to the web version of this article.)

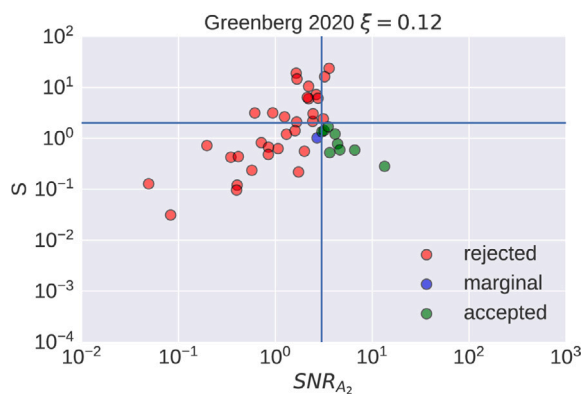


Fig. 7. S parameter as a function of signal to noise ratio SNR_{A2} . Green circles represents accepted values ($SNR_{A2} > 3$ and $S < 2$) - consistent with expected value determined as in Greenberg et al. (2020) with efficiency $\xi = 0.12$, blue circles are marginal cases with $2.5 < SNR_{A2} < 3$ and $S < 2$, and red are values with $SNR_{A2} > 3$ or $S > 2.5$. Horizontal line represents $S = 2$. Vertical line represents $SNR_{A2} = 3$. (For interpretation of the references to color in this figure legend, the reader is referred to the web version of this article.)

in Del Vigna et al. (2018) and accept objects for which $SNR_{A2} > 3$ and $S < 2$. Objects for which $SNR_{A2} < 2.5$ or $S > 2$ are rejected. Objects with $S < 2$ and SNR_{A2} is in the range from 2.5 to 3.0 are considered marginal detection.

For 7 objects (1620, 1685, 2062, 2063, 2100, 3200, 66391) with $SNR_{A2} > 3$, the estimated da/dt value is consistent with a conservative approach based on Spoto et al. (2015) and Del Vigna et al. (2018) (Fig. 6). For 9 objects (1620, 1685, 2062, 2063, 2100, 3200, 10563, 66391, 105140) with $SNR_{A2} > 3$, the estimated da/dt value is consistent with the expected value computed as in Greenberg et al. (2020) and assuming median efficiency of $\xi = 0.12$ (Fig. 7). An efficiency equal to the median value plus uncertainty $\xi = 0.28$ adds the asteroid (7889) 1994 LX to the group of asteroids consistent with the expected value. Two asteroids having $SNR_{A2} > 3$ and $S > 2$ are (1036) Ganymed and (1103) Sequoia. For the first one, the da/dt value estimated in this work is consistent with the literature (detection was made by multiple authors) (Greenberg et al., 2020; Farnocchia et al., 2013; Nugent et al., 2012) For asteroid 1103 Sequoia the Yarkovsky drift has never been published before. Both of those are relatively big asteroids with diameters $D = 37.675 \pm 0.399$ km and $D = 6.692 \pm 0.078$ km respectively, thus the expected da/dt_{exp} is small. The detected empirical

drift thus is unreliable ($S > 2$), not explicable by the Yarkovsky effect and may be due to the possible systematic errors and uncertainties in the measurements.

Retrograde rotators have negative Yarkovsky drift and prograde positive, thus we decided to check the sense of rotation of the studied asteroids. We extracted the spin and shape models from the DAMIT database.¹⁰ There were models available for 10 of our targeted objects (Table 4). One of them - (1747) Wright, had an inconsistent sign of the spin axis ecliptic latitude ($\beta = 31^\circ$, which corresponds to the positive value of the obliquity $\phi = 28^\circ$ - the angle between the spin pole vector and the orbit normal vector) with the estimated Yarkovsky drift direction. However, for that object $SNR_{A2} < 3$, thus, we do not consider it a detection at this point.

As the last point, we verified various orbit computation algorithms. Since Gaia mission was designed for stellar astrometry, it is not optimized for moving objects, such as asteroids and NEOs. To avoid problems with transit-specific systematic errors, Hanuš et al. (2018) proposed to use only the first astrometric observation from each transit, following Fedorets et al. (2018) who used so-called normal points derived for each transit. The work of Fedorets et al. (2018) focuses on objects with short observing arcs that are handled in the Gaia's short-term processing pipeline. Astrometry arriving from that pipeline is burdened with larger systematic uncertainties than those in the data releases (such as DR2). Gaia altitude is iteratively improved in the long-term processing pipeline, which results in smaller systematic uncertainties. Fedorets et al. (2018) noted high correlations (approaching unity) of RA, Dec for the short-arc objects, which led to ill-conditioned covariance matrices. This problem is not apparent for asteroids in our sample. For well-observed objects and data arriving from DR2, there is no need to reduce the number of measurements. In Table 7 we present the $A2$ parameter together with SNR_{A2} estimated based on the full dataset and the dataset reduced to one observation from each transit. Differences are negligible, thus we recommend the use of all observations.

5. Summary and future work

We have estimated the secular drift in semi-major axis da/dt for 42 Yarkovsky drift candidates from Mouret and Mignard (2011) and compared those to the expected values determined as in Spoto et al. (2015), Del Vigna et al. (2018) and Greenberg et al. (2020). For 12 objects we obtained $SNR > 3$. Most of those match the average expected analytical da/dt values estimated based on physical parameters.

For some objects, the derived da/dt drift in the semi-major axis is higher than theoretically expected. Two of those objects have large diameters, thus the detected change may be due to other reasons (e.g. systematic measurements uncertainties and model errors such as incorrect assumptions of physical properties etc.). For other objects, either the efficiency of the Yarkovsky effect may be larger than assumed or the uncertain or assumed physical parameters may also play a significant role in the estimation of the theoretical value. We follow the approach of Del Vigna et al. (2018) to finally accept only detections which strongly agree with the expected theoretical values. This is not to claim detection that may be later disputed.

Seven objects are consistent with the expected values estimated as in Spoto et al. (2015) and Del Vigna et al. (2018) and 9–10 estimated as in Greenberg et al. (2020). Most of the estimated drifts are negative, which is consistent with the preponderance of retrograde rotators in the literature.

In 20 out of 42 cases, the addition of the Gaia astrometry led to an improvement in the SNR_{A2} . The best example of that is 66391 Moshup for which the SNR_{A2} increased from 2.6 to 13.42, while $A2$ remained of the same order of magnitude. Overall, the Gaia DR2 astrometry led

¹⁰ <https://astro.troja.mff.cuni.cz/projects/damit/>.

Table 4

The A2 parameter was determined using various data sets (MPC data, MPC and DR2 data in the 80-column format, MPC and DR2 data in the ADES format. References: (1) Greenberg et al. (2020) (2) Del Vigna et al. (2018), (3) Farnocchia et al. (2013), (4) Nugent et al. (2012), (5) Chesley et al. (2008), (6) Hanuš et al. (2018). Parameter β is ecliptic latitude of a spin axis. Potentially hazardous asteroids are marked with the letter P. Binary systems are marked with the letter B. da/dt value in column 10 is transformed from A2(ADES+DR2) in column 7.

Ast.	A2 (MPC) [10^{-15} AU d $^{-2}$]	SNR	A2 (MPC+DR2) [10^{-15} AU d $^{-2}$]	SNR	Gaia rej.	A2 (ADES+DR2) [10^{-15} AU d $^{-2}$]	SNR	Gaia rej.	da/dt [10^{-4} AU My $^{-1}$]	Lit. [10^{-4} AU My $^{-1}$]	β [deg]
244	-15.43 ± 6.64	2.32	-24.59 ± 6.6	3.73	3/142	-14.47 ± 6.57	2.2	0/142	-4.25 ± 1.93		-80, -74
1036	-14.62 ± 3.02	4.84	-13.37 ± 2.97	4.5	0/157	-9.58 ± 2.67	3.59	0/157	-3.48 ± 0.97	-4.98 ± 1.3(1) -6.06 ± 1.59(3) -6.6 ± 1.5(4)	-78, -79
1103	-36.79 ± 12.02	3.06	-47.92 ± 11.85	4.04	22/112	-36.95 ± 11.45	3.23	0/112	-11.38 ± 3.53		-59
1139	-11.46 ± 4.18	2.74	-10.79 ± 4.16	2.59	0/105	-10.98 ± 4.16	2.64	0/105	-3.58 ± 1.35		
1620	-2.57 ± 1.06	2.42	-1.68 ± 1.05	1.6	37/82	-3.13 ± 0.86	3.64	0/82	-1.34 ± 0.37	-1.02 ± 0.5(1) -2.5 ± 0.5(4) -1.18 ± 0.39(5)	-49
1685	-4.0 ± 0.83	4.82	-3.72 ± 0.82	4.54	20/102	-3.51 ± 0.8	4.39	0/102	-1.57 ± 0.36	-1.57 ± 0.4 (1) -1.68 ± 0.38(2) -1.27 ± 0.34(3) -1.4 ± 0.7(4) -0.52 ± 0.27(5)	-69
1747	-16.8 ± 6.72	2.5	-16.55 ± 6.69	2.47	43/133	-14.41 ± 6.54	2.2	0/133	-4.74 ± 2.15		31
1864	-30.43 ± 9.5	3.2	-27.45 ± 9.44	2.91	14/82	-25.33 ± 9.18	2.76	0/82	-14.3 ± 5.18	-11.67 ± 5.8(1) -11.67 ± 8.2(4) -2.26 ± 2.5(1)	
1866	0.88 ± 4.69	0.19	0.49 ± 4.69	0.1	4/41	0.23 ± 4.68	0.05	0/41	0.1 ± 2.03		
1943	21.49 ± 23.38	0.92	25.06 ± 22.98	1.09	0/136	21.02 ± 22.4	0.94	0/136	7.99 ± 8.51		
2062	-15.26 ± 2.13	7.16	-15.13 ± 2.08	7.27	38/69	-8.18 ± 1.24	6.6	0/69	-3.65 ± 0.55	-5.34 ± 0.7(1) -5.89 ± 0.68(2) -6.29 ± 1.10(3) -7.5 ± 2.4(4)	
2063	-19.62 ± 4.63	4.24	-19.53 ± 4.63	4.22	0/22	-18.16 ± 4.39	4.14	0/22	-8.46 ± 2.05	-6.22 ± 1.9 (1) -4.17 ± 3.7 (4) -10.59 ± 2.21 (5)	
2100	-3.93 ± 0.86	4.57	-3.91 ± 0.85	4.6	5/33	-3.94 ± 0.85	4.64	0/33	-2.27 ± 0.49	-2.04 ± 0.6(1) -2.67 ± 0.63(2) -6.31 ± 1.30(3) -5.4 ± 1.5(4)	-65
2629	-12.33 ± 12.09	1.02	-18.31 ± 11.94	1.53	37/163	-24.94 ± 11.66	2.14	0/163	-8.47 ± 3.96		
3103	-9.07 ± 3.83	2.37	-10.35 ± 3.86	2.68	36/65	-9.64 ± 3.58	2.69	0/65	-3.95 ± 1.47	-2.83 ± 2.2(1)	-70, -69
3200	-3.9 ± 1.09	3.58	-5.5 ± 1.13	4.87	20/118	-3.05 ± 1.01	3.02	0/118	-5.52 ± 1.83	-9.57 ± 2.1(1) -6.9 ± 1.9(6)	-47
3554	-18.18 ± 11.67	1.56	62.48 ± 6.68	9.35	18/69	1.94 ± 5.59	0.35	0/69	0.91 ± 2.61	9.0 ± 8.8 (4)	
3753	-4.13 ± 4.43	0.93	-5.28 ± 4.4	1.2	9/41	-4.63 ± 4.34	1.07	0/41	-2.68 ± 2.51	-5.14 ± 3.4(1) -11.2 ± 5.3(4)	
3800	-13.33 ± 12.12	1.1	-57.67 ± 9.95	5.8	21/155	-11.34 ± 8.71	1.3	0/155	-3.86 ± 2.96		
4769	-11.68 ± 4.98	2.35	-8.59 ± 4.84	1.77	61/117	-6.08 ± 3.05	1.99	1/117	-3.27 ± 1.64	-6.14 ± 2.8(1) -17.2 ± 11.7(4)	
4953	-17.28 ± 17.72	0.98	-8.13 ± 17.18	0.47	4/72	-3.29 ± 16.76	0.2	0/72	-1.93 ± 9.85		
5381	-0.93 ± 5.06	0.18	-4.02 ± 4.75	0.85	19/96	-1.97 ± 4.89	0.4	0/96	-0.94 ± 2.34		
5427	-27.69 ± 27.98	0.99	-43.66 ± 26.36	1.66	27/109	-15.27 ± 24.91	0.61	0/109	-4.69 ± 7.65		-83
6618	22.71 ± 15.37	1.48	22.09 ± 15.38	1.44	28/80	25.17 ± 15.34	1.64	0/80	7.82 ± 4.77		
7889	-30.66 ± 9.78	3.13	-37.16 ± 9.72	3.82	11/45	-30.37 ± 9.72	3.12	0/45	-13.05 ± 4.18	-6.15 ± 5.2(1)	
10563	-20.99 ± 10.41	2.02	-34.0 ± 9.65	3.52	24/34	-16.15 ± 5.08	3.18	0/34	-7.36 ± 2.31	17.09 ± 7.7 (1) 32.3 ± 14.50 (4)	
12711	-14.32 ± 8.68	1.65	-18.01 ± 8.66	2.08	21/37	-14.33 ± 8.64	1.66	0/37	-6.03 ± 3.64		
66146	-9.57 ± 6.62	1.45	-14.72 ± 6.58	2.24	39/68	-4.38 ± 6.12	0.72	0/68	-2.74 ± 3.82	-5.60 ± 3.9(1)	
66391	-5.31 ± 2.04	2.6	-6.38 ± 1.8	3.54	4/24	-4.83 ± 0.36	13.42	0/24	-4.86 ± 0.36	-5.73 ± 2.2(1)	
68216	20.37 ± 22.07	0.92	13.17 ± 19.08	0.69	7/24	6.73 ± 16.23	0.41	0/24	2.78 ± 6.72		
85818	-89.21 ± 70.82	1.26	-42.14 ± 68.39	0.62	19/79	-110.22 ± 65.99	1.67	0/79	-43.99 ± 26.34		
86667	1.83 ± 4.99	0.37	0.59 ± 4.97	0.12	19/51	1.98 ± 4.98	0.4	0/51	1.4 ± 3.53		
87684	-2.53 ± 6.26	0.4	-19.38 ± 6.16	3.15	89/160	-5.0 ± 5.89	0.85	0/160	-3.9 ± 4.6	-14.35 ± 7.1(1)	
88710	-0.27 ± 8.61	0.03	45.26 ± 11.34	3.99	34/108	-0.64 ± 7.72	0.08	0/108	-0.28 ± 3.43		
96590	3.26 ± 2.18	1.5	3.24 ± 2.18	1.49	7/15	3.78 ± 2.18	1.73	0/15	1.92 ± 1.11	2.30 ± 1.1(1)	
105140	-11.1 ± 4.44	2.5	-10.66 ± 4.4	2.42	15/49	-13.29 ± 3.79	3.51	0/49	-17.75 ± 5.06	-15.73 ± 14.02(3)	
137805	-15.78 ± 5.87	2.69	-17.05 ± 5.7	2.99	15/39	-13.63 ± 5.62	2.43	0/39	-9.23 ± 3.81	-6.27 ± 5.3(1)	
137925	-1.72 ± 6.88	0.25	-10.59 ± 6.53	1.62	18/129	-5.36 ± 6.34	0.85	0/129	-4.81 ± 5.69		
154555	-3.86 ± 23.19	0.17	-121.12 ± 20.43	5.93	65/143	-25.41 ± 20.43	1.24	0/143	-14.95 ± 12.02		
163693	-16.59 ± 10.01	1.66	-13.07 ± 9.85	1.33	9/21	-11.56 ± 7.24	1.6	2/21	-6.36 ± 3.99		
163899	-1.4 ± 5.91	0.24	0.62 ± 5.92	0.1	35/46	4.55 ± 7.96	0.57	1/46	2.22 ± 3.89		
164121	-22.37 ± 14.77	1.51	-37.54 ± 14.66	2.56	34/54	-27.12 ± 11.08	2.45	0/54	-11.95 ± 4.88		

to the improvement of SNR_{A2} for 29 objects where 12 of them have $SNR_{A2} > 3$.

Lastly, we showed that using the complete Gaia data set and the full covariance matrix for each object is a valid approach and there is no need to reduce the astrometry to one observation from each transit as done before by other authors.

Gaia DR2 asteroid astrometry impacts the Yarkovsky drift determination, but with the limited number of observations and observing span covered, a higher number of detections will be possible with the next release of the catalogue. Gaia DR3 will both increase the number of highly accurate observations and extend the observational arc, thus

Table 5
Values of (101955) bennu properties, used in Eq. (2).

Quantity	Symbol	Value	Reference
Yarkovsky effect	$(da/dt)_B$	$-19.03 \cdot 10^{-4} \text{ AU My}^{-1}$	Greenberg et al. (2020)
Diameter	D_B	$0.482 \text{ km} \pm 0.3$	Daly et al. (2020)
Density	ρ_B	$1.194 \pm 0.003 \text{ g/cm}^3$	Daly et al. (2020)
Geometric albedo	$(p_V)_B$	0.044 ± 0.002	Hergenrother et al. (2019)
Obliquity	ϕ_B	$176 \pm 4 \text{ deg}$	Lauretta et al. (2017)

Table 6
Average density for asteroid taxonomic type (Carry, 2012).

Spectral type	Density [g/cm ³]
S	2.6 ± 1.29
V	1.93 ± 1.07
X	2.87 ± 2.59
B	2.19 ± 1.0

Table 7
Comparison of the A2 value determined using all observations (MPC+radar+Gaia) and only 1st observation per Gaia transit (Fedorets et al., 2018) with the use of ADES format.

Ast.	A2 (all) [10 ⁻¹⁵ AU d ⁻²]	SNR	A2 (1st from transit) [10 ⁻¹⁵ AU d ⁻²]	SNR
244	-14.47 ± 6.57	2.2	-14.46 ± 6.59	2.19
1036	-9.58 ± 2.67	3.59	-11.69 ± 2.8	4.17
1103	-36.95 ± 11.45	3.23	-36.44 ± 11.59	3.14
1139	-10.98 ± 4.16	2.64	-11.33 ± 4.16	2.72
1620	-3.13 ± 0.86	3.64	-3.0 ± 0.92	3.26
1685	-3.51 ± 0.8	4.39	-3.77 ± 0.81	4.65
1747	-14.41 ± 6.54	2.2	-15.48 ± 6.6	2.35
1864	-25.33 ± 9.18	2.76	-26.5 ± 9.3	2.85
1866	0.23 ± 4.68	0.05	0.27 ± 4.68	0.06
1943	21.02 ± 22.4	0.94	20.94 ± 23.06	0.91
2062	-8.18 ± 1.24	6.6	-13.42 ± 1.85	7.25
2063	-18.16 ± 4.39	4.14	-19.06 ± 4.57	4.17
2100	-3.94 ± 0.85	4.64	-3.93 ± 0.86	4.57
2629	-24.94 ± 11.66	2.14	-16.35 ± 11.94	1.37
3103	-9.64 ± 3.58	2.69	-8.44 ± 3.6	2.34
3200	-3.05 ± 1.01	3.02	-3.26 ± 1.05	3.1
3554	1.94 ± 5.59	0.35	-4.34 ± 5.99	0.72
3753	-4.63 ± 4.34	1.07	-4.69 ± 4.34	1.08
3800	-11.34 ± 8.71	1.3	-11.11 ± 8.74	1.27
4769	-6.08 ± 3.05	1.99	-10.37 ± 3.79	2.74
4953	-3.29 ± 16.76	0.2	-4.96 ± 16.9	0.29
5381	-1.97 ± 4.89	0.4	-1.37 ± 4.96	0.28
5427	-15.27 ± 24.91	0.61	-20.85 ± 25.42	0.82
6618	25.17 ± 15.34	1.64	24.13 ± 15.36	1.57
7889	-30.37 ± 9.72	3.12	-29.74 ± 9.73	3.06
10563	-16.15 ± 5.08	3.18	-25.07 ± 7.81	3.21
12711	-14.33 ± 8.64	1.66	-13.99 ± 8.64	1.62
66146	-4.38 ± 6.12	0.72	-9.46 ± 6.37	1.49
66391	-4.83 ± 0.36	13.42	-4.67 ± 0.43	10.86
68216	6.73 ± 16.23	0.41	6.39 ± 16.36	0.39
85818	-110.22 ± 65.99	1.67	-101.26 ± 67.15	1.51
86667	1.98 ± 4.98	0.4	1.67 ± 4.99	0.33
87684	-5.0 ± 5.89	0.85	-2.73 ± 6.1	0.45
88710	-0.64 ± 7.72	0.08	0.42 ± 8.33	0.05
96590	3.78 ± 2.18	1.73	3.48 ± 2.18	1.6
105140	-13.29 ± 3.79	3.51	-13.22 ± 3.98	3.32
137805	-13.63 ± 5.62	2.43	-14.47 ± 5.66	2.56
137925	-5.36 ± 6.34	0.85	-5.92 ± 6.39	0.93
154555	-25.41 ± 20.43	1.24	8.84 ± 20.81	0.42
163693	-11.56 ± 7.24	1.6	-12.18 ± 7.39	1.65
163899	4.55 ± 7.96	0.57	7.15 ± 8.38	0.85
164121	-27.12 ± 11.08	2.45	-34.3 ± 13.52	2.54

most likely a higher number of candidates from Mouret and Mignard (2011) and others will be confirmed.

Acknowledgments

We thank Federika Spoto (Minor Planet Center — Center for Astrophysics, Harvard & Smithsonian, 60 Garden St., MS 15, Cambridge

(MA), USA), Palo Tanga (Université Côte d’Azur, Observatoire de la Côte d’Azur, CNRS, Laboratoire Lagrange, France), Davide Farnocchia (Jet Propulsion Laboratory, California Institute of Technology, Pasadena, CA 91109, USA) and friendly referees for insightful comments.

The research leading to these results has received funding from the Ministry of Science and Higher Education of Poland in the years 2018/2022, as a research project under the “Diamond Grant” program, grant number 0062/DIA/2018/47. DO was supported by National Science Centre, Poland, grant number 2017/26/D/ST9/00240. This work has used data from the European Space Agency (ESA) mission Gaia¹¹ and was possible thanks to the open-source OrFit software.¹² This research has used data and/or services provided by the International Astronomical Union’s Minor Planet Center, The JPL Horizons On-Line Ephemeris System, and the Gaia collaboration. We would like to thank all observers who submitted data to the Minor Planet Center.

References

- Binzel, R., DeMeo, F., Turtelboom, E., Bus, S., Tokunaga, A., Burbine, T., Lantz, C., Polishook, D., Carry, B., Morbidelli, A., et al., 2019. Compositional distributions and evolutionary processes for the near-earth object population: Results from the MIT-hawaii near-earth object spectroscopic survey (MITHNEOS). *Icarus* 324, 41–76.
- Binzel, R.P., Morbidelli, A., Merouane, S., DeMeo, F.E., Birlan, M., Vernazza, P., Thomas, C.A., Rivkin, A.S., Bus, S.J., Tokunaga, A.T., 2010. Earth encounters as the origin of fresh surfaces on near-earth asteroids. *Nature* 463 (7279), 331–334.
- Bottke Jr., W.F., Vokrouhlický, D., Rubincam, D.P., Nesvorný, D., 2006. The Yarkovsky and YORP effects: Implications for asteroid dynamics. *Annu. Rev. Earth Planet. Sci.* 34, 157–191.
- Carry, B., 2012. Density of asteroids. *Planet. Space Sci.* 73 (1), 98–118.
- Chesley, S.R., Baer, J., Monet, D.G., 2010. Treatment of star catalog biases in asteroid astrometric observations. *Icarus* 210 (1), 158–181.
- Chesley, S.R., Ostro, S.J., Vokrouhlický, D., Čapek, D., Giorgini, J.D., Nolan, M.C., Margot, J.-L., Hine, A.A., Benner, L.A., Chamberlin, A.B., 2003. Direct detection of the Yarkovsky effect by radar ranging to asteroid 6489 Golevka. *Science* 302 (5651), 1739–1742.
- Chesley, S., Vokrouhlický, D., Ostro, S., Benner, L., Margot, J., Matson, R., Nolan, M., Shepard, M., 2008. Direct estimation of Yarkovsky accelerations on near-Earth asteroids. *LPI Contrib.* 1405 (8330), 37.
- Daly, M., Barnouin, O., Seabrook, J., Roberts, J., Dickinson, C., Walsh, K., Jawin, E., Palmer, E., Gaskell, R., Weirich, J., et al., 2020. Hemispherical differences in the shape and topography of asteroid (101955) Bennu. *Sci. Adv.* 6 (41), eabd3649.
- Del Vigna, A., Faggioli, L., Milani, A., Spoto, F., Farnocchia, D., Carry, B., 2018. Detecting the Yarkovsky effect among near-Earth asteroids from astrometric data. *Astron. Astrophys.* 617, A61.
- Farnocchia, D., Chesley, S., Chamberlin, A., Tholen, D., 2015. Star catalog position and proper motion corrections in asteroid astrometry. *Icarus* 245, 94–111.
- Farnocchia, D., Chesley, S.R., Milani, A., Gronchi, G.F., Chodas, P.W., 2015. Orbits, long-term predictions, impact monitoring. In: *Asteroids IV*. pp. 815–834.
- Farnocchia, D., Chesley, S., Vokrouhlický, D., Milani, A., Spoto, F., Bottke, W., 2013. Near Earth asteroids with measurable Yarkovsky effect. *Icarus* 224 (1), 1–13.
- Fedorets, G., Muinonen, K., Pauwels, T., Granvik, M., Tanga, P., Virtanen, J., Berthier, J., Carry, B., David, P., Dell’Oro, A., et al., 2018. Optimizing asteroid orbit computation for Gaia with normal points. *Astron. Astrophys.* 620, A101.
- Greenberg, A.H., Margot, J.-L., Verma, A.K., Taylor, P.A., Hodge, S.E., 2017a. Yarkovsky Drift Detections for 159 Near-Earth Asteroids. eScholarship, University of California.
- Greenberg, A.H., Margot, J.-L., Verma, A.K., Taylor, P.A., Hodge, S.E., 2020. Yarkovsky drift detections for 247 near-earth asteroids. *Astron. J.* 159 (3), 92.
- Greenberg, A.H., Margot, J.-L., Verma, A.K., Taylor, P.A., Naidu, S.P., Brozovic, M., Benner, L.A., 2017b. Asteroid 1566 Icarus’s size, shape, orbit, and Yarkovsky drift from radar observations. *Astron. J.* 153 (3), 108.

¹¹ <https://www.cosmos.esa.int/gaia>.

¹² <http://adams.dm.unipi.it/orbit/>.

- Hanuš, J., Vokrouhlický, D., Delbo, M., Farnocchia, D., Polishook, D., Pravec, P., Hornoch, K., Kučáková, H., Kušnirák, P., Stephens, R., et al., 2018. (3200) Phaethon: Bulk density from Yarkovsky drift detection. *Astron. Astrophys.* 620, L8.
- Hergenrother, C., Maleszewski, C., Nolan, M., Li, J.-Y., d'Aubigny, C.D., Shelly, F., Howell, E., Karet, T., Izawa, M., Barucci, M., et al., 2019. The operational environment and rotational acceleration of asteroid (101955) Bennu from OSIRIS-REX observations. *Nature Commun.* 10 (1), 1–10.
- La Spina, A., Paolicchi, P., Kryszczyńska, A., Pravec, P., 2004. Retrograde spins of near-Earth asteroids from the Yarkovsky effect. *Nature* 428 (6981), 400–401.
- Lauretta, D., Balram-Knutson, S., Beshore, E., Boynton, W., Drouet d'Aubigny, C., DellaGiustina, D., Enos, H., Golish, D., Hergenrother, C., Howell, E., et al., 2017. OSIRIS-REX: sample return from asteroid (101955) Bennu. *Space Sci. Rev.* 212 (1), 925–984.
- Milani, A., Gronchi, G., 2010. *Theory of Orbit Determination*. Cambridge University Press.
- Mouret, S., Mignard, F., 2011. Detecting the Yarkovsky effect with the Gaia mission: list of the most promising candidates. *Mon. Not. R. Astron. Soc.* 413 (2), 741–748.
- Nesvorný, D., Bottke, W.F., 2004. Detection of the Yarkovsky effect for main-belt asteroids. *Icarus* 170 (2), 324–342.
- Nugent, C., Margot, J., Chesley, S., Vokrouhlický, D., 2012. Detection of semimajor axis drifts in 54 near-Earth asteroids: New measurements of the Yarkovsky effect. *Astron. J.* 144 (2), 60.
- Öpik, E.J., 1951. Collision probabilities with the planets and the distribution of interplanetary matter. In: *Proceedings of the Royal Irish Academy. Section a: Mathematical and Physical Sciences*, Vol. 54. JSTOR, pp. 165–199.
- Pérez-Hernández, J.A., Benet, L., 2022. Non-zero Yarkovsky acceleration for near-Earth asteroid (99942) Apophis. *Commun. Earth Environ.* 3 (1), 1–5.
- Rozitis, B., Green, S.F., 2014. Physical characterisation of near-Earth asteroid (1620) geographos-reconciling radar and thermal-infrared observations. *Astron. Astrophys.* 568, A43.
- Spoto, F., Milani, A., Knežević, Z., 2015. Asteroid family ages. *Icarus* 257, 275–289.
- Spoto, F., Tanga, P., Mignard, F., Berthier, J., Carry, B., Cellino, A., Dell'Oro, A., Hestroffer, D., Muinonen, K., Pauwels, T., et al., 2018. Gaia data release 2-observations of solar system objects. *Astron. Astrophys.* 616, A13.
- Thomas, C., Trilling, D.E., Emery, J., Mueller, M., Hora, J., Benner, L., Bhattacharya, B., Bottke, W., Chesley, S., Delbó, M., et al., 2011. ExploreNEOs. V. Average albedo by taxonomic complex in the near-Earth asteroid population. *Astron. J.* 142 (3), 85.
- Vereš, P., Farnocchia, D., Chesley, S.R., Chamberlin, A.B., 2017. Statistical analysis of astrometric errors for the most productive asteroid surveys. *Icarus* 296, 139–149.
- Vokrouhlický, D., Milani, A., Chesley, S., 2000. Yarkovsky effect on small near-earth asteroids: Mathematical formulation and examples. *Icarus* 148 (1), 118–138.
- Yarkovsky, I., 1901. *The Density of Luminiferous Ether and the Resistance it Offers to Motion* (Available in the Appendix of M. Brož's thesis). Bryansk.

Publication III

The Yarkovsky effect and bulk density of near-Earth asteroids from *Gaia* DR3

Karolina Dziadura¹ , Dagmara Oszkiewicz¹, Federica Spoto², Benoit Carry³, Paolo Tanga³, and Przemysław Bartczak^{1,4}

¹ Astronomical Observatory Institute, Faculty of Physics, A. Mickiewicz University, Słoneczna 36, 60-286 Poznań, Poland
e-mail: karolinadziadura36@gmail.com

² Center for Astrophysics, Harvard & Smithsonian, 60 Garden St., MS 15, Cambridge, MA, USA

³ Université Côte d'Azur, Observatoire de la Côte d'Azur, CNRS, Laboratoire Lagrange, Nice, France

⁴ Instituto Universitario de Física Aplicada a las Ciencias y las Tecnologías (IUFACyT), Universidad de Alicante, Ctra. San Vicente del Raspeig s/n, 03690 San Vicente del Raspeig, Alicante, Spain

Received 3 July 2023 / Accepted 13 October 2023

ABSTRACT

Aims. The primary objective of this study is to utilize *Gaia* DR3 asteroid astrometry to detect the Yarkovsky effect, a non-gravitational acceleration that affects the orbits of small asteroids. We then computed the bulk densities for the sample of objects for which we obtained an estimation of the Yarkovsky effect.

Methods. We used the version of the OrbFit software that is currently developed at the Minor Planet Center (MPC). We utilized the complete astrometric dataset from the MPC, encompassing all radar data and *Gaia* DR3 observations. The orbital computation was performed for a total of 446 Near-Earth Asteroids (NEAs; including 93 Potentially Hazardous Asteroids (PHAs)), and 54 094 Inner Main Belt Asteroids (IMBAs) as well as Mars Crossing asteroids. Furthermore, we used a new validation method which involved computing the A2 (the Yarkovsky effect) using different observational arcs to observe the stability of the result. We applied the Yarkovsky effect to determine the density of the studied asteroids.

Results. Thanks to *Gaia* DR3 we significantly constrained orbital uncertainties and determined reliable A2 values for 49 Near-Earth Asteroids, including 10 new detections and for all improvements in signal-to-noise ratio. Additionally, we successfully determined the density, along with their uncertainties, for all of these objects. However, regarding IMBAs, although we have made progress, we do not detect Yarkovsky drift for any asteroid in the main belt.

Conclusions. Adding a relatively small amount of ultra-precise astrometry from *Gaia* DR3 to the observations from the Minor Planet Center (MPC) not only significantly improves the orbit of the asteroid but also enhances the detectability of non-gravitational parameters. Utilizing this improved dataset, we were able to determine the densities, along with their uncertainties, for the studied asteroids. Looking ahead, with the upcoming release of *Gaia* DR4, we anticipate even more detections for NEAs and new detections for IMBA and Mars Crossing Asteroids.

Key words. planets and satellites: dynamical evolution and stability – minor planets, asteroids: general – planets and satellites: physical evolution

1. Introduction

The Yarkovsky effect is the change in the semi-major axis, caused by anisotropic thermal radiation from the surface of the asteroid (Bottke et al. 2006). It can be divided into diurnal and seasonal components (Vokrouhlický et al. 2015a). The first component relates to a delay between the absorption and re-emission of thermal radiation on a rotating body having some thermal inertia. Generally, the diurnal Yarkovsky effect increases the semimajor axis of prograde rotators and decreases for retrograde rotating asteroids. The seasonal effect is related to the seasonal heating and cooling of the asteroid's hemispheres during its yearly orbital motion. The seasonal effect always leads to an decrease in the semi-major axis. For asteroids larger than 100 m in diameter, the diurnal effect dominates (Farinella et al. 1998).

The diurnal effect depends on the physical and dynamic properties of the asteroid. The typical diameter for which the diurnal effect is the strongest is considered to be on the order of centimetres to meters. Larger objects will be less affected, and

the effect is negligible for bodies with $d \gtrsim 40$ km (Bottke et al. 2006). Contrary to the seasonal effect, the diurnal effect is maximum for obliquity $\gamma = 0^\circ$ or 180° and null for $\gamma = 90^\circ$. Moreover, the overall Yarkovsky effect depends on the surface conductivity, density, shape, and heliocentric distance of the object (see Bottke et al. 2006; Vokrouhlický et al. 2015a, for a full description).

The Yarkovsky effect was first detected for the LAGEOS (Rubincam 1988) artificial Earth satellite as an explanation of the residuals in its orbital elements. The semimajor axis exhibited a decrease at a rate of approximately 1.1 mm day^{-1} . Considering LAGEOS' rapid rotation and its high surface thermal inertia, this specific rate of change aligned with the seasonal component of the Yarkovsky effect (Rubincam 1988). Later, the Yarkovsky effect was detected for the asteroid (6489) Golevka (Chesley et al. 2003), thanks to radar observations during Golevka's close approaches in 1991, 1995, and 2003.

As of today, a few objects have a precisely (signal to noise $S/N > 100$) determined Yarkovsky effect (Farnocchia et al. 2021; Pérez-Hernández & Benet 2022; Vokrouhlický et al. 2015b). Thanks to the NASA OSIRIS-REx mission Lauretta et al. (2017),

the asteroid with the most accurately determined Yarkovsky drift is (101955) Benu. The latest research has led to the result of $da/dt = -284.6 \pm 0.2 \text{ m yr}^{-1}$, which corresponds to a large S/N of ~ 1400 (Farnocchia et al. 2021).

The Yarkovsky effect also plays a significant role in the long-term assessment and mitigation strategies of Earth’s impact risk (Farnocchia et al. 2015). For example, (99942) Apophis was on the top of the Risk lists¹ for about 17 yr (Chesley 2005). Due to accurate astrometry from new radar and stellar occultation observations, made during its close approach in 2021, the impact could now be ruled out (at least for the next 100 yr)². This was possible due to the precise Yarkovsky drift determination ($da/dt = -199.0 \pm 1.5 \text{ m yr}^{-1}$; Pérez-Hernández & Benet 2022). Improvement of the Yarkovsky effect will lead to a better estimate of collision probability, because it has been found to be the most significant non-gravitational acceleration affecting asteroid orbits (Chesley et al. 2014).

Estimations of the Yarkovsky effect can also be used to constrain asteroid densities. Since its determination is agnostic about the physical parameters of the object, the only assumption to make is that the non-gravitational acceleration is dominated by the Yarkovsky effect (Chesley et al. 2014). Solving the approximate analytical expression of the Yarkovsky effect allows for the determination of the bulk density (Golubov et al. 2016; Nugent et al. 2012). Using this method, the bulk density of (101955) Benu was accurately determined at $1260 \pm 70 \text{ kg m}^{-3}$ (Chesley et al. 2014), prior to the OSIRIS-REx mission’s encounter with the asteroid (Goossens et al. 2021). This was later confirmed to be $1191.57 \pm 1.74 \text{ kg m}^{-3}$ using data collected during the mission (Goossens et al. 2021). Furthermore, seven additional asteroids have undergone density determinations utilizing this approach: (3200) Phaethon, with a reported density of $\rho = 1.67 \pm 0.47 \text{ g cm}^{-3}$ (Hanuš et al. 2018), (6489) Golevka, with a density of $\rho = 2.7_{-0.6}^{+0.4} \text{ g cm}^{-3}$ (Chesley et al. 2003), (1862) Apollo with a density of $\rho = 2.85_{-0.68}^{+0.48} \text{ g cm}^{-3}$ (Rozitis et al. 2013), (1620) Geographos with a density of $\rho = 2.10_{-0.45}^{+0.55} \text{ g cm}^{-3}$ (Rozitis & Green 2014) and asteroids with bulk density functions presented in Farnocchia et al. (2013).

The Yarkovsky effect plays a crucial role in understanding the dynamical evolution of individual asteroids, asteroid families, and the overall asteroid population (Bottke et al. 2001; Nesvorný & Bottke 2004). It also contributes to our understanding of meteorite delivery to Earth (Bottke et al. 2006), aids in determining the ages of asteroid families (Spoto et al. 2015), and impact monitoring (Farnocchia et al. 2015). So far the effect has been directly detected for about a few hundred asteroids, all of them being NEOs (Greenberg et al. 2020; Del Vigna et al. 2018; Farnocchia et al. 2013; Nugent et al. 2012; Chesley et al. 2008).

Orbital inversion (without the Yarkovsky effect) is performed routinely in the *Gaia* development units DU456 and DU457 (Coordination Unit CU4 object processing) of the *Gaia* Data Processing and Analysis Consortium (DPAC). The methods implemented in the short-term processing pipeline are derived from the work of Muinonen et al. (2016), Oszkiewicz et al. (2009), Virtanen et al. (2001; DU456). The long-term data processing (DU457) of astrometry involves the traditional least-squares method with the differential correction algorithm (Gaia Collaboration 2018; Tanga et al. 2023; Spoto et al. 2018; Milani & Gronchi 2010).

¹ <https://cneos.jpl.nasa.gov/sentry/>

² https://www.esa.int/Space_Safety/Planetary_Defence/Apophis_impact_ruled_out_for_the_first_time

Prior to the start of the *Gaia* mission, the expectation was that the high precision of astrometry from the ESA’s *Gaia* space mission will allow for the detection of the effect for a large number of asteroids, including Main Belt objects (Mignard et al. 2007; Mouret & Mignard 2011; Mouret 2011; Spoto et al. 2018). In Dziadura et al. (2022) we determined the effect for 42 asteroids from the *Gaia* DR2 catalog. Here, we significantly extended our sample and used the latest release of the *Gaia* catalog. *Gaia* DR3 was published on 13 June 2022 and contains astrometry for over 150 000 Solar System Objects (SSOs). Moreover, compared to DR2, this data release not only contains more objects and observations but also provides a longer observational arc (22 vs 63 months) which is critical for precise orbit determination (Tanga et al. 2023).

The present study focuses on the determination of the non-gravitational transverse acceleration (the Yarkovsky effect – A2 or da/dt) with the use of *Gaia* DR3 asteroid astrometry, similar to Dziadura et al. (2022). We process the DR3 astrometry of all near-Earth asteroids (NEAs) and asteroids in the inner main belt in combination with all the available observations from the MPC and radar measurements from Jet Propulsion Laboratory (JPL). In Sect. 2, we describe the data used in this work. In Sect. 3, we describe the methodology used for the orbit determination and the density determination process. In Sect. 4, we present the results of the A2 and densities. We summarize our results in Sect. 5.

2. Data and selection of asteroids

Gaia is a space observatory orbiting at the Lagrangian point L2 of the Sun-Earth system. On 13 June 2022, it had the third complete data release (*Gaia* DR3). The DR3 catalog contains a large number of stellar data and a large number of asteroid observations. In particular, there are 23 336 467 astrometric measurements that represent 3 214 776 focal CCD plane transits (Tanga et al. 2023). The DR3 along scan astrometric uncertainty is at a sub-milliarcsecond level for objects of magnitude $G < 18$. For the purpose of this study, we used the astrometry of selected Solar System objects from DR3.

Gaia mission was designed for stellar astrometry; therefore, moving objects (such as asteroids) will drift during observation on the focal plane. Due to this effect, its signal can be cut at the scanning window. Moreover, the information across the scan of the object comes only from the sky mapper field of the CCD. Thus, the accuracy of the across scan is around one arcsecond while for the along scan information comes from the astrometric field of *Gaia* and reaches the milliarcsecond level. For this reason, the *Gaia* astrometry data points are highly correlated, and it is crucial to use both error components (systematic and random) of the astrometry (Spoto et al. 2018; Tanga et al. 2023; Dziadura et al. 2022).

Generally, the detection of the Yarkovsky effect depends on the formal uncertainty of the orbital elements, especially the semi-major axis (Del Vigna et al. 2018). Asteroids with longer observational arcs have typically been observed in more oppositions; thus, uncertainties of the orbital parameters are usually smaller. *Gaia* mission observes numbered asteroids with relatively long observational arcs. Therefore, we selected all objects from *Gaia* DR3 without additional requirements for the length of the observing arc.

From the *Gaia* DR3 catalog, we selected all available NEA (446), including 93 Potentially Hazardous Asteroids (PHAs), and all Inner Main Belt Asteroids (IMBAs) and Mars Crossers

Table 1. Number of objects and observations.

Group	Number objects	N_{total} observations	N_{MPC} observations	N_{radar} observations	N_{Gaia} observations
NEA	446	645 921	611 893	664	33 364
IMBA and Mars crossing	154 094	77 536 340	70 246 354	17	7 289 969

Notes. N_{total} are all observations. N_{MPC} are ground-based and satellite astrometry downloaded from MPC. N_{radar} is the number of radar data. and N_{Gaia} is the number of *Gaia* DR3 observations.

(semi-major axes $a < 2.5$ au) which accounts for 54 094 asteroids. The total number of *Gaia* observations used for this study is 7 323 333. For these objects, we also downloaded all available optical data (ground-based and satellite) from [Minor Planet Center \(2022\)](#) and radar observations from [JPL Solar System Dynamics \(2022b\)](#). The number of optical and radar observations incorporated in this research is 70 858 247 and 681, respectively.

We present a summary of the data used for this study in Table 1. For each population, we indicate the number of total observations used and the number of optical, radar, and DR3 data. Furthermore, in Table 2 we present a more detailed breakdown of the data, we indicate the date of the first and last observations, and the number of each type of observation (MPC, radar, *Gaia* DR3) used in this study, diameters, and the dynamical group. All available diameters and their uncertainties were retrieved from the SsODNet service ([Berthier et al. 2023](#)) using its `rocks python` package³. Most of the diameters come from the NEOWISE mission ([Masiero et al. 2011](#); [Masiero et al. 2012, 2014](#); [Nugent et al. 2016](#)). If the uncertainty was not available, we assumed it to be 1/3 of the diameter (as in [Greenberg et al. 2020](#)) and if the diameter was not available, we estimated it from the absolute magnitude and albedo.

Astrometric data were corrected for biases arising from the use of various stellar catalogs ([Farnocchia et al. 2015](#); [Eggl et al. 2020](#)). We use a modified version of the OrbFit software developed at the Minor Planet Center that accounts for corrections of the biases arising from the use of various stellar catalogs ([Farnocchia et al. 2015](#); [Eggl et al. 2020](#)) and the weighting scheme ([Farnocchia et al. 2015](#); [Vereš et al. 2017](#)).

3. Methodology

3.1. Detection of the Yarkovsky effect

We used the standard linearized least-squares orbit computation method with differential corrections described, for example, in [Milani & Gronchi \(2010\)](#), [Milani et al. \(2005\)](#), [Farnocchia et al. \(2015\)](#). We follow the procedure outlined in our previous work ([Dziadura et al. 2022](#)) that we summarize here.

The general idea of orbit determination is to minimize the linearized target function (Eq. (1)) and the vectors of residuals.

$$Q(x) = \frac{1}{m} \xi(x)^T W \xi(x) \quad (1)$$

where $Q(x)$ is the target function, m is the number of observations, $\xi(x)$ are residuals and W is the weight matrix. To find the best fit (minimum residual), we search for stationary points of the target function. In each iteration, an orbit improvement is

³ <https://rocks.readthedocs.io/en/latest/>

made, and the solution is given by the differential corrections algorithm.

Different observations from various telescopes have different weights, which are included in the weighing scheme that is used during the orbiting computation. Outliers are automatically removed from the fit using a threshold value of χ^2 . The rejected observation can be recovered for the fit in a further iteration if it provides a smaller χ^2 ([Carpino et al. 2003](#); [Milani & Gronchi 2010](#)).

In the N -body problem, we included the masses of all planets, the Moon, Pluto and the 16 most massive asteroids in accordance with the precision of the astrometric observations and because they have a significant gravitational effect ([Milani & Gronchi 2010](#)). The list of the 16 most massive asteroids used in this work can be found in [Del Vigna et al. \(2018; Table 1\)](#).

3.2. Density estimation

The daily and annual components of the Yarkovsky effect can be written, using the formalism adapted from [Farinella et al. \(1998\)](#) and [Vokrouhlický et al. \(2015a\)](#):

$$\frac{da}{dt} = \frac{6(1-A)S_{\odot}}{9nD\rho c\Delta^2} [W_n \sin^2 \gamma - 2W_{\omega} \cos \gamma] \quad (2)$$

with :

$$W_{\nu} \approx -\frac{0.5 \Theta_{\nu}}{1 + \Theta_{\nu} + 0.5\Theta_{\nu}^2}$$

$$\Theta_{\nu} = \frac{\Gamma \sqrt{\nu}}{\epsilon \sigma_B T_{\star}^3} \quad \text{with } \nu = n \text{ or } \nu = \omega$$

$$T_{\star}^4 = \frac{(1-A)S_{\odot}}{\eta \sigma_B \epsilon \Delta^2}$$

where n is the orbital mean motion (rad s^{-1}) dictating the annual component $W_n \sin^2 \gamma$, ω is the asteroid angular rotation frequency (rad s^{-1}) responsible for the daily component $W_{\omega} \cos \gamma$, D is the asteroid diameter (m), A its Bond albedo ($(0.29 + 0.684G)p_V$, with G the phase slope and p_V the geometric albedo in V band), ρ its density (kg m^{-3}), Γ its thermal inertia ($\text{J m}^{-2} \text{s}^{-1/2} \text{K}^{-1}$), γ its obliquity (the angle between its orbital and rotational angular momenta, in rad), Δ is the distance to the Sun (au), S_{\odot} is the solar constant at 1 au (W m^{-2}), T_{\star} is the subsolar point temperature (K) and the other parameters are constants: (c the speed of light, ϵ the emissivity, σ_B the Stefan-Boltzmann constant, and η the beaming parameter). The Eq. (2) derives from the solution of the linearized heat diffusion in a spherical body orbiting the Sun on a circular trajectory. Depending on the specific shape, the Yarkovsky effect value can deviate by several tens of percent from the true value ([Vokrouhlický 1998](#)) Those factors introduce an element of uncertainty.

Table 2. Summary of the data used for this study.

Number	Name	Group	First obs.	Last obs.	N_{total}	N_{MPC}	N_{radar}	N_{Gaia}
1566	Icarus	P	1949-06-27	2022-07-25	1438	1384	23	31
1685	Toro		1948-07-17	2021-08-04	3828	3680	9	139
1862	Apollo	BP	1930-12-13	2022-03-14	2468	2300	17	151
1865	Cerberus		1971-10-26	2021-09-23	2148	2036	0	112
1943	Anteros		1968-06-03	2022-02-14	4815	4623	0	192
2062	Aten		1955-12-17	2019-11-10	1144	987	7	150
2063	Bacchus		1977-04-24	2022-09-19	935	869	12	54
2100	Ra-Shalom		1975-10-03	2022-10-10	3778	3724	10	44
3103	Eger		1982-01-20	2022-06-16	4587	4475	4	108
3200	Phaethon	P	1983-10-11	2022-10-07	6861	6498	8	355
3908	Nyx		1980-08-06	2022-05-22	2160	2072	16	72
4179	Toutatis	P	1934-02-10	2022-05-06	6741	6641	63	37
4769	Castalia	P	1989-08-01	2022-07-10	468	314	15	139
6239	Minos	P	1983-01-14	2021-01-10	1274	1200	3	71
7335	1989 JA	P	1989-04-06	2022-10-06	2464	2412	5	47
7341	1991 VK	P	1981-10-23	2022-06-07	2352	2284	13	55
7482	1994 PC1	P	1974-09-22	2022-07-28	1732	1490	2	240
7822	1991 CS	P	1991-01-19	2022-07-08	1963	1845	4	114
10302	1989 ML		1989-06-06	2022-09-24	1195	1111	0	84
11054	1991 FA		1937-11-28	2022-06-04	1313	1294	0	19
17511	1992 QN		1992-08-29	2022-10-06	2064	2042	1	21
22099	2000 EX106		1994-01-30	2022-10-02	1186	1115	0	71
29075	1950 DA	P	1950-02-22	2021-12-03	999	933	12	54
33342	1998 WT24	P	1998-11-24	2022-02-20	1954	1883	17	54
38086	Beowulf		1992-05-01	2022-03-23	1066	911	0	155
52750	1998 KK17		1992-08-29	2022-08-19	1452	1377	0	75
55408	2001 TC2		1979-11-13	2018-09-09	290	259	0	31
66391	Moshup	BP	1998-05-29	2022-07-18	4322	4240	37	45
68950	2002 QF15	P	1955-07-23	2021-10-15	2939	2862	13	64
85953	1999 FK21		1971-03-26	2022-02-04	1300	1284	0	16
85989	1999 JD6		1990-06-22	2022-06-25	3022	2980	15	27
86667	2000 FO10		1988-05-11	2022-04-28	1679	1610	0	69
87024	2000 JS66		1979-01-06	2022-03-03	2062	2018	1	43
88710	2001 SL9	B	1954-11-27	2016-01-04	1134	1007	0	127
99907	1989 VA		1989-11-02	2022-10-05	1075	1029	0	46
99935	2002 AV4		1955-01-29	2022-08-05	1840	1762	0	78
105140	2000 NL10		1952-09-17	2022-10-09	2681	2589	0	92
137924	2000 BD19		1997-02-10	2022-04-16	876	834	7	35
138852	2000 WN10		2000-11-20	2022-01-31	1182	1173	0	9
138947	2001 BA40		2001-01-23	2022-03-23	552	522	0	30
141531	2002 GB		2002-04-01	2021-04-13	794	744	0	50
161989	Cacus	P	1978-02-08	2022-10-03	1660	1543	0	117
162142	1998 VR		1998-11-10	2021-12-06	618	581	0	37
162173	Ryugu	P	1986-04-14	2021-06-21	2215	2121	0	94
162181	1999 LF6		1979-12-20	2022-05-24	1694	1659	2	33
163000	2001 SW169		1997-12-25	2022-10-07	1233	1158	0	75
163243	2002 FB3	P	2002-03-18	2022-07-01	1110	1027	0	83
164206	2004 FN18		1954-10-05	2022-07-29	570	545	0	25
172034	2001 WR1		1953-02-14	2022-03-08	814	791	0	23
188174	2002 JC		1991-05-16	2022-06-28	417	379	3	35
192563	1998 WZ6	P	1998-11-23	2022-09-17	1123	1078	0	45
276409	2002 YN2		2002-12-27	2021-02-12	351	222	0	129
311554	2006 BQ147		1992-02-01	2021-02-26	521	500	1	20
317643	2003 FH1		2003-03-24	2021-05-25	813	789	0	24
345705	2006 VB14		2006-11-15	2021-01-12	1377	1285	1	91
363505	2003 UC20	P	1954-12-05	2021-12-12	749	638	5	106
385186	1994 AW1	P	1986-12-29	2022-09-19	2430	2341	3	86

Notes. We include only accepted and marginal objects (Sect. 4) The columns denote asteroid number and name, date of the first and last observation, number of all observations, number of MPC records (satellite and ground-based observations), number of radar observations, number of *Gaia* DR3 observing points. Potentially hazardous asteroids are marked with the letter P. Binary systems are marked with the letter B.

From the knowledge of the semi-major axis drift (da/dt) derived from the astrometry (Sect. 3.1) and of the other parameters in Eq. (2), one can determine the density ρ of the asteroid (e.g., Chesley et al. 2014). We thus compiled the best estimates for these parameters for each asteroid in our sample, using the ssoCard of SsODNet⁴ through its rocks⁵ interface (Berthier et al. 2023). This service contains all parameters from all available literature. If there are multiple measurements of one parameter present in the literature, it provides the one obtained using the most accurate technique or computes a statistically weighted average of the parameter. Many parameters are, however, unknown for many targets, such as their thermal inertia or their obliquity. We thus build a reference probability density function (PDF) of each parameter based on all asteroids (using the BFT, see Berthier et al. 2023). To determine the density and its uncertainty, we use a Monte-Carlo approach, drawing 20 000 random samples for each parameter (either from its known estimate or from the reference PDFs).

4. Results

We computed orbits for 54,633 asteroids using a modified version OrbFit software⁶ (Milani & Gronchi 2010) developed at the Minor Planet Center. For each object, we estimated the six usual orbital parameters along with A2, the non-gravitational transverse acceleration.

To verify the reliability of the detection, we computed the theoretically expected values of the Yarkovsky effect for all of the studied objects and compared them to our empirical estimates. We used the same approach as in Spoto et al. (2015); Del Vigna et al. (2018); Dziadura et al. (2022, Eq. (2)) with one exception. All the previous works have used the asteroid (101955) Bennu as a benchmark to validate the detected Yarkovsky accelerations. Recent results from the OSIRIS-REx mission (Farnocchia et al. 2021; Hergenrother et al. 2019) proved that modelling the Yarkovsky effect for Bennu requires more attention than just fitting the available optical and radar astrometry. Therefore, we have decided to adopt another asteroid as our benchmark, namely (99942) Apophis. Thanks to its close approach to Earth in 2021, Apophis has now the second best-known value of the Yarkovsky effect (Sect. 1). The orbital parameters of (101955) Bennu are better known; however, its semimajor axis undergoes variations influenced by its intrinsic activity. Consequently, we computed the expected values $A2_{\text{expected}}$ of the Yarkovsky effect using the physical and orbital parameters of the studied objects and scaling it to the Apophis elements provided in Table 3.

Next, we determined the parameter S , which is the ratio between the estimated A2 based on astrometry (empirical approach) and the expected value (theoretical approach) $S = A2_{\text{empirical}}/A2_{\text{expected}}$. Detection is considered accepted when the S parameter < 2 (the determined value is less than twice the theoretically expected A2) and the signal-to-noise ratio (S/N_{A2}) > 3 . The marginal results are those with $S < 2$ and $2.5 < S/N_{A2} < 3$. The remaining supposed detections are rejected. Objects with $S/N > 3$ but $S > 2$ have much higher A2 values than predicted and the reason for that may be related to other effects (e.g. cometary-like activity) or wrong estimation of physical properties for which we determine the theoretical effect. However, we are not able to tell if it is just a systematic bias in astrometry

Table 3. Apophis orbital and physical parameters.

Param.	Value	Ref.
A2	$-29.01 \pm 0.23 \times 10^{-15}$ au d ⁻²	Computed
ρ	2.66 g cm ⁻³	Following Carry (2012)
A	$0.14^{+0.03}_{-0.04}$	Müller et al. (2014)
γ	167.1 deg	Vokrouhlický et al. (2015b)
D	0.34 km	Brozović et al. (2018)
a	$0.9227 \pm 2.0453 \times 10^{-9}$ au	JPL Solar System Dynamics (2022a)
e	$0.1914 \pm 1.1454 \times 10^{-9}$	JPL Solar System Dynamics (2022a)

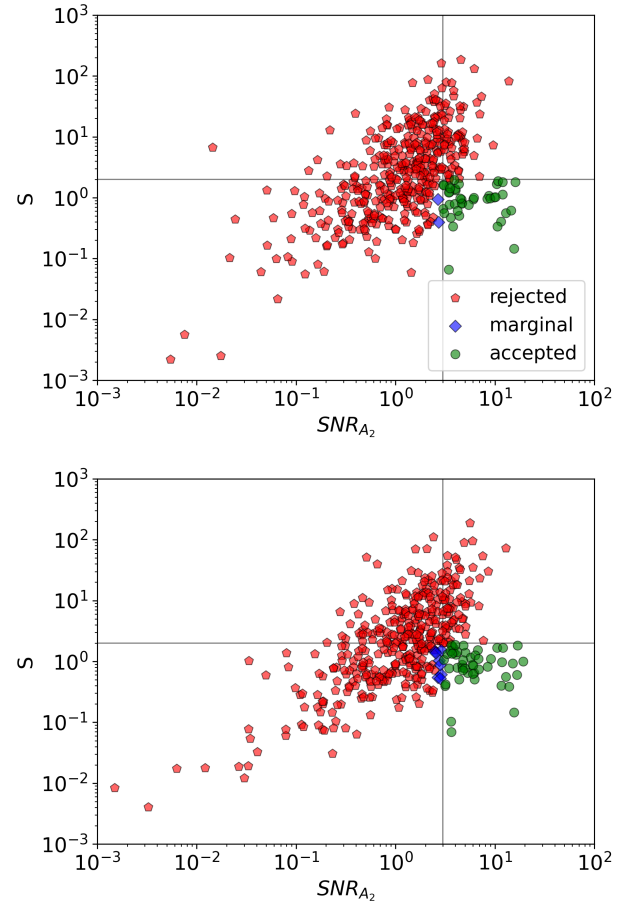


Fig. 1. Parameter S as a function of S/N_{A2} for all NEA without using *Gaia* DR3 – top panel, using *Gaia* DR3 – bottom panel. Green circles represent accepted values ($S/N_{A2} > 3$ and $S < 2$) – consistent with the expected value scaled to the (99942) Apophis A2 value, blue circles are marginal cases with $2.5 < S/N_{A2} < 3$ and $S < 2$ and red are values with $S/N_{A2} > 3$ or $S > 2.5$. The horizontal line represents $S = 2$. The vertical line represents $S/N_{A2} = 3$.

therefore further studies for these objects are needed and here we categorise them as rejected. Using a different approach for computing the expected value yield more accepted objects. Nevertheless, we selected the most stringent and accurate method to ensure the validity of our results and avoid any potential false claims.

First, we determined A2 for all NEAs without using *Gaia* DR3 data. The results are presented in Fig. 1 top panel. There are 41 accepted (green circles), 2 marginal (blue diamonds), and 403 rejected (red pentagons) asteroids. Next, we repeat the computation by adding *Gaia* DR3 observations. The results are presented

⁴ <https://ssp.imcce.fr/webservices/ssodnet/>

⁵ <https://rocks.readthedocs.io/en/latest/>

⁶ <http://adams.dm.unipi.it/orbfit/>

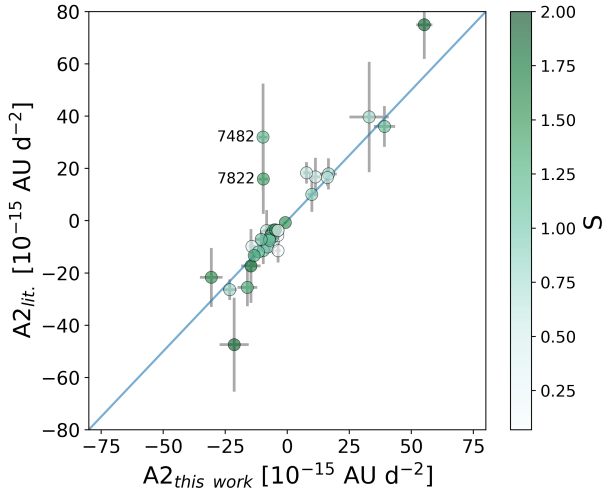


Fig. 2. Comparison of the A2 value determined in this work with the literature Greenberg et al. (2020), Āurech et al. (2018), Del Vigna et al. (2018), Farnocchia et al. (2013), Nugent et al. (2012). S value computed for the A2 parameter determined in this work.

in Fig. 1 bottom panel. We obtained 49 accepted asteroids, 8 marginal asteroids, and 389 rejected asteroids. As a result of adding *Gaia* DR3 observations, there are 10 new accepted results for asteroids. Two of the asteroids that were accepted without using *Gaia* DR3, due to the reduction of both the A2 value and the uncertainty, fell into marginal cases. For most objects, adding the *Gaia* data resulted in the reduction of the orbital element uncertainties and global Root Mean Square (RMS) of the observations. In Table A.1 we list the results and other parameters of all accepted NEAs when using *Gaia* DR3. There are 20 PHAs and 3 binary objects in this data set.

We compared the results of A2 presented in this work with the value of A2 from the literature. We show the comparison in Fig. 2. Generally, the results agree well. Most objects are consistent with the literature. However, there are two objects, 7782 and 7822, with opposite signs. Any other minor discrepancies in values are likely attributed to the utilization of distinct data sets for orbit determination, particularly the inclusion of *Gaia* DR3 in our study. Furthermore, for all asteroids, the uncertainty of A2 is smaller in this work than in the literature. In the figure, we also present the S value as a colour bar.

We introduced an additional verification method for the accepted results. This method involved calculating the orbit using the most recent 5 yr of observations, and then progressively including older observations in two-year intervals. This approach allowed us to assess the behaviour of the A2 parameter and determine if its value or signal-to-noise ratio (S/N) was significantly influenced by the oldest observations. In most cases, we observed a distinct pattern of decreasing the absolute value of A2 and decreasing uncertainty. A notable example of this behaviour can be seen in the case of (3200) Phaethon (see Fig. 3). However, we obtained a different result for asteroid (433) Eros (Fig. 4). If we had considered only the last observation in 1952 for the fit, the result would have been positive with considerably high uncertainty. We refrain from claiming accepted results if they are only based on old observations. Additionally, the obliquity of (433) Eros, which suggested the A2 to be positive, further supported the decision to exclude it from the accepted group. As a result, (433) Eros was not used for further computations, and it was removed from Fig. 1.

The theoretical equation of the drift of the Yarkovsky effect predicts a diameter dependence $\langle da/dt \rangle \propto D^{-1.0}$ (Greenberg et al. 2020). We compute the empirical value of A2 based on astrometric measurements independent of the physical properties of the asteroids. Therefore, we can determine the dependence of the Yarkovsky effect on the diameter. To compare the results, we derived the value da/dt from A2 as in Farnocchia et al. (2013). In Fig. 5, we present a comparison of the magnitude of the Yarkovsky effect and the diameter of the object. We used an Orthogonal Distance Regression (Jones et al. 2001) and fit a power law. The best fit $\langle da/dt \rangle \propto D^{-1.09 \pm 0.15}$, similar to Greenberg et al. (2020). In Fig. 5, there is an exceptional green object located at the top right. This object corresponds to (3200) Phaethon. The reason for this behaviour is its high eccentricity, with a value of $e \sim 0.89$ and the A2 value is inversely proportional to $(1 - e^2)$.

Among the accepted A2 values for NEA, there are 39 negative and 10 positive results. This corresponds to 39 retrograde rotators N_r and 10 prograde rotators N_p . It leads to the preponderance of retrograde rotators (N_r) over prograde rotators (N_p), the ratio is $N_r/N_p = 3.9$. Similar to the Farnocchia et al. (2013) $N_r/N_p = 4$ and higher than in Greenberg et al. (2020) $N_r/N_p = 2.7$, La Spina et al. (2004) $N_r/N_p = 2^{+1}_{-0.7}$, Greenberg et al. (2017) $N_r/N_p = 2.9 \pm 0.7$ and Nugent et al. (2012) $N_r/N_p = 2.5 \pm 0.1$. The excess in retrograde rotators was to be expected, considering that all the objects examined are small NEAs primarily injected into their current orbits by the ν_6 resonance (Āurech et al. 2018; La Spina et al. 2004; Granvik et al. 2018). This resonance is located in the Inner Main Belt area therefore, only objects evolve towards the Sun (retrograde rotators). Other resonances (like 3:1 resonance) that are injecting NEAs from the Main Belt are affecting both types of asteroids (prograde and retrograde). Therefore, the presence of retrograde axes in NEAs is important not only for their rotational characteristics but also for understanding their dynamical evolution and the implications of the Yarkovsky effect on these objects.

Furthermore, we analyzed the dependence of formal semi-major axis uncertainties on the detectability of the Yarkovsky effect for NEAs. The theoretical Yarkovsky drift for a 1 km asteroid is in order of 3×10^{-10} au y^{-1} , therefore it causes an orbit change of 3×10^{-9} au in 10 yr (Farnocchia et al. 2013). For this reason, the theoretical uncertainty of the semimajor axis, for ~ 1 km object, should be lower than $\sigma(a) < 3 \times 10^{-9}$ au, so we could detect the effect (Del Vigna et al. 2018). Among the accepted NEAs, the formal uncertainty was $\sigma(a) < 3 \times 10^{-9}$ au with the exception of one small object (141531) with $\sigma(a) < 3.7 \times 10^{-9}$ and diameter = 303 ± 14 m (Nugent et al. 2016). Overall, including *Gaia* DR3 in the fit resulted in a decrease in the orbital parameters uncertainties.

We have computed the density values for all accepted and marginally accepted results. An example of physical properties presented as a function of density can be found in Fig. 6. Ten results were excluded from the list due to physically implausible values. A histogram showing the distribution of these results, grouped according to taxonomic class, is presented in Fig. 7. The values are presented in Table A.1. There were three results available in the literature for comparison. For (1862) Apollo $\rho \sim 2050 \pm 350$ kg m^{-3} in Ford et al. (2014) and $\rho = 2850^{+480}_{-680}$ kg m^{-3} (Rozitis et al. 2013), while our work yielded a value of $2792.61^{+410.85}_{-506.58}$ kg m^{-3} . For (66391) Moshup $\rho \sim 1267.9 \pm 627.16$ kg m^{-3} (Scheirich & Pravec 2009; Scheirich et al. 2021) and here we obtained $2253.60^{+783.01}_{-620.77}$ kg m^{-3} . For (88710) $\rho \sim 1800.0 \pm 1500.0$ kg m^{-3} (Scheirich et al. 2021),

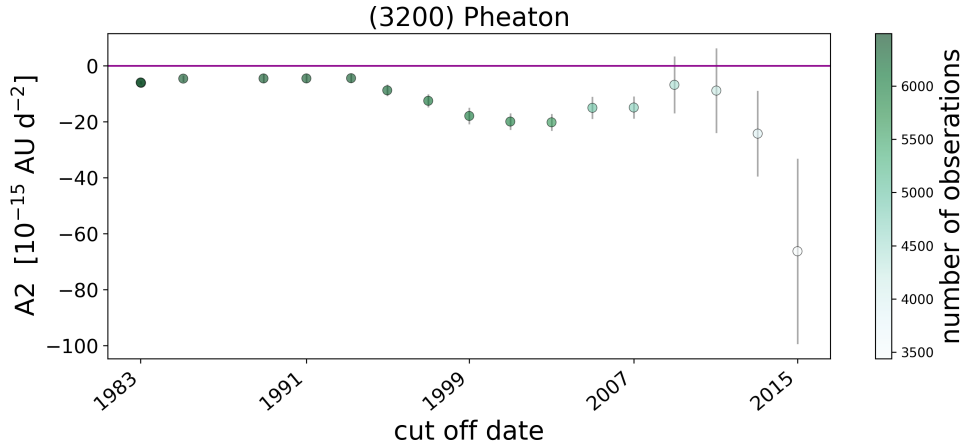


Fig. 3. A2 value of (3200) Phaethon, depicted as a function of the observational arc utilized for orbit determination, with the cut-off date representing the date of the last observation included in the fit. The colorbar indicates the number of observations used for the determination of A2. The horizontal line is set at the value 0.

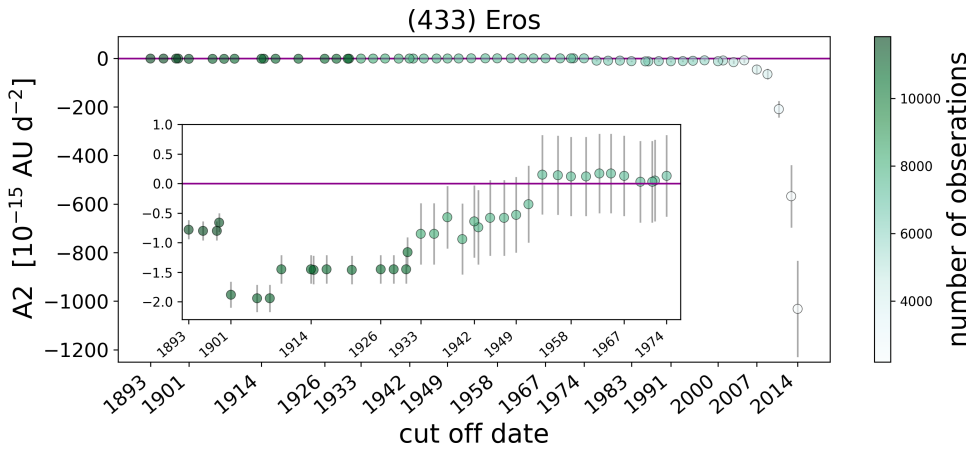


Fig. 4. A2 value of (433) Eros as a function of observational arc. Axes, colours, horizontal line as in Fig. 3. The inside panel is zoomed in on the years 1893–1974.

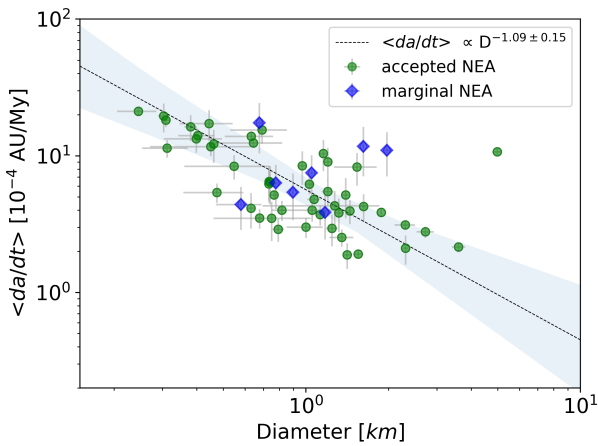


Fig. 5. Non-gravitational transverse acceleration as a function of the object diameter, D , for accepted and marginal NEA. Our analysis yields a diameter dependence of $D^{-1.09 \pm 0.15}$, consistent with the theoretical expectation for the Yarkovsky effect of $D^{-1.0}$ and the one estimated in Greenberg et al. (2020), $D^{-1.06 \pm 0.05}$.

whereas our result was $2249.96_{-935.36}^{+1344.43} \text{ kg m}^{-3}$. These consistent findings further support the reliability of our measurements.

Moreover, we computed orbits including A2, for all IMBAs and Mars-crossing asteroids in *Gaia* DR3 (54,094 objects). We used the same approach to determine the S value as we used for NEAs. Results are presented in Fig. 8, where we present the S/N_{A2} versus S for all IMBAs and Mars-crossing asteroids. We are yet not ready to claim the first detections for Non-NEA

objects. However, when we used a less restrictive approach – just comparing the A2 to Bennu diameter only – there were 3 accepted and 18 marginal results and 54 073 rejected. Nevertheless, this indicates that we are really close to detecting the A2 for the non-NEA object. Further investigation of these objects is necessary using *Gaia* DR4 or maybe even the focus product release (October 2023), which will provide a 5-yr observational arc.

5. Conclusions

We have computed orbits for 54 094 objects in the Main Belt and Mars Crosser groups and 446 NEAs with the goal of estimating the Yarkovsky effect. We obtained 41 accepted A2 results without using *Gaia* DR3 data and 49 accepted A2 results when using *Gaia* DR3 data. None of the previous studies used *Gaia* Data Release 3 (DR3) for orbit determination. Our results prove that adding a small number of ultraprecise astrometry allows better detections of the Yarkovsky effect.

Based on the results of the Yarkovsky effect for accepted NEAs, we determined the retrograde to prograde rotation ratio as $N_r/N_p = 3.9$ and the diameter dependence $\langle da/dt \rangle \propto D^{-1.09 \pm 0.15}$. Furthermore, in this study, we introduced an additional validation method. Firstly, we employed the A2 dependence of the observational arc utilized for orbit determination, resulting in the exclusion of (433) Eros from the accepted list. Secondly, we used the Yarkovsky effect to determine the density by considering the A2 values of all accepted and marginal detections and verifying the physicality of the obtained results. Additionally, we provided density measurements for all of these objects.

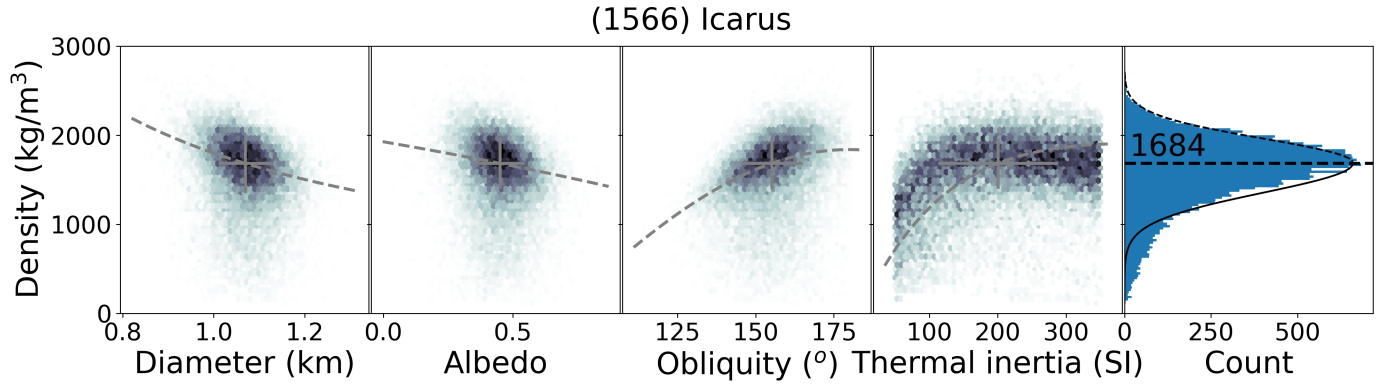


Fig. 6. Example of density determination for (1566) Icarus. The cross indicates the best solution, and the dashed line the variation for each parameter. The reported density and uncertainties (Table A.1) are computed by fitting a two-sided Gaussian on the distribution of density.

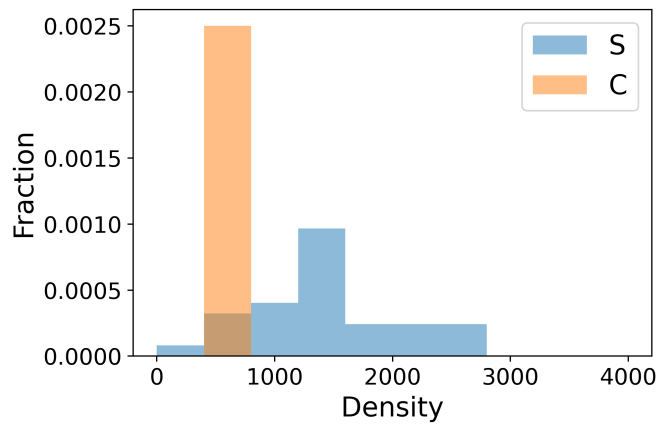


Fig. 7. Histogram displaying the density results, categorized by the taxonomic type of the asteroids.

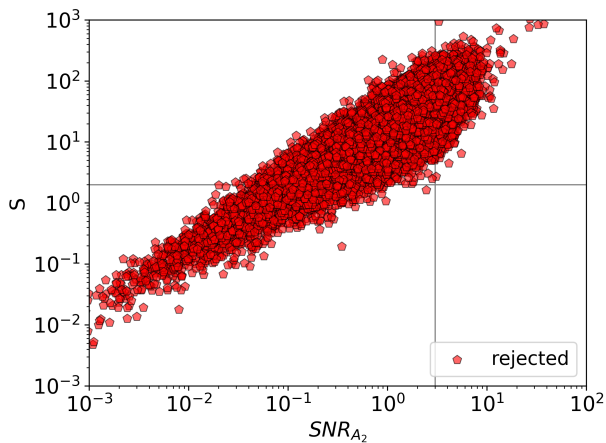


Fig. 8. Parameter S as a function of S/N_{A2} for all IMBAs and Mars-crossing asteroids using *Gaia* DR3. Axes, colours, horizontal and vertical lines as in Fig. 1.

In this study, we have made significant progress towards the detection of the Yarkovsky effect in non-NEA objects. We are nearing the threshold of detecting a reliable A2 measurement for these objects. However, it is important to note that further investigation is required to establish the discovery of this effect, using an empirical approach, in Main Belt asteroids. Our current methodology is limited in its ability to consider all

potential close approaches of other Solar System objects, thereby making it challenging to disentangle non-gravitational effects from small gravitational perturbations. Our gravitational force calculations encompass the influence of all planets, the moon, the 16 most massive asteroids, and Pluto. Consequently, there exists a possibility of ambiguity in our findings.

Moreover, through our analysis, we have identified a set of 11 069 objects with $S/N > 2$, providing a valuable catalogue of promising Main Belt asteroids that warrant additional scrutiny. These objects represent the initial targets for future investigations into the Yarkovsky effect among MBAs. As we move forward, it is imperative to incorporate data from a more comprehensive ensemble of perturbing asteroids, in conjunction with forthcoming *Gaia* focus product release and *Gaia* DR4 data, to enhance our understanding of this phenomenon.

Acknowledgements. We thank the referee David Vokrouhlický for insightful comments. The research leading to these results has received funding from the National Science Center, Poland, grant number 2022/45/N/ST9/01403 in the years 2023/2024 and Ministry of Science and Higher Education of Poland in the years 2018/2021, as a research project under the “Diamond Grant” program, grant number 0062/DIA/2018/47. D.O. was supported by the National Science Center, Poland, grant number 2017/26/D/ST9/00267. P.B. was supported by grant no. 2022/45/ST9/00267 and through the Spanish Government retraining plan “María Zambrano 2021–2023” at the University of Alicante (ZAMBRANO22-04). This work has used data from the European Space Agency (ESA) *Gaia* mission (<https://www.cosmos.esa.int/gaia>). This work presents results from the European Space Agency (ESA) *Gaia* space mission. *Gaia* data are being processed by the *Gaia* Data Processing and Analysis Consortium (DPAC). Funding for the DPAC is provided by national institutions, in particular, the institutions participating in the *Gaia* MultiLateral Agreement (MLA). The *Gaia* mission website is <https://www.cosmos.esa.int/gaia>. The *Gaia* archive website is <https://archives.esac.esa.int/gaia> and was possible thanks to the open source OrbFit software (<http://adams.dm.unipi.it/orbfit/>). This research has used data and/or services provided by the International Astronomical Union Minor Planet Center, The JPL Horizons On-Line Ephemeris System, and the Gaia Collaboration. We thank all observers who submitted data to the Minor Planet Center. We did an extensive use of the VO tools TOPCAT (Taylor 2005) and SsODNet (Berthier et al. 2023). Thanks to all the developers and maintainers.

References

- Alí-Lagoa, V., Müller, T. G., Usui, F., & Hasegawa, S. 2018, *A&A*, 612, A85
 Benner, L. A. M., Hudson, R. S., Ostro, S. J., et al. 1999, *Icarus*, 139, 309
 Benner, L. A. M., Ostro, S. J., Hudson, R. S., et al. 2002, *Icarus*, 158, 379
 Berthier, J., Carry, B., Mählke, M., & Normand, J. 2023, *A&A*, 671, A151
 Binzel, R. P., DeMeo, F. E., Turtelboom, E. V., et al. 2019, *Icarus*, 324, 41
 Botke, W. F., Vokrouhlický, D., Brož, M., Nesvorný, D., & Morbidelli, A. 2001, *Science*, 294, 1693
 Botke, W. F., Vokrouhlický, D., Rubincam, D. P., & Nesvorný, D. 2006, *Annu. Rev. Earth Planet. Sci.*, 34, 157

- Brozović, M., Benner, L. A., McMichael, J. G., et al. 2018, *Icarus*, **300**, 115
- Busch, M. W., Giorgini, J. D., Ostro, S. J., et al. 2007, *Icarus*, **190**, 608
- Busch, M. W., Benner, L. A. M., Ostro, S. J., et al. 2008, *Icarus*, **195**, 614
- Carpino, M., Milani, A., & Chesley, S. R. 2003, *Icarus*, **166**, 248
- Carry, B. 2012, *Planet. Space Sci.*, **73**, 98
- Carry, B., Solano, E., Ettl, S., & DeMeo, F. E. 2016, *Icarus*, **268**, 340
- Chesley, S. R. 2005, *Proc. Int. Astron. Union*, **1**, 215
- Chesley, S. R., Ostro, S. J., Vokrouhlický, D., et al. 2003, *Science*, **302**, 1739
- Chesley, S., Vokrouhlický, D., Ostro, S., et al. 2008, *LPI Contrib.*, **1405**, 37
- Chesley, S. R., Farnocchia, D., Nolan, M. C., et al. 2014, *Icarus*, **235**, 5
- Dandy, C. L., Fitzsimmons, A., & Collander-Brown, S. J. 2003, *Icarus*, **163**, 363
- Delbo, M. 2004, PhD thesis, Free University of Berlin, Germany
- Delbo, M., Harris, A. W., Binzel, R. P., Pravec, P., & Davies, J. K. 2003, *Icarus*, **166**, 116
- Del Vigna, A., Faggioli, L., Milani, A., et al. 2018, *A&A*, **617**, A61
- Durech, J., Vokrouhlický, D., Kaasalainen, M., et al. 2008, *A&A*, **488**, 345
- Đurech, J., Vokrouhlický, D., Baransky, A., et al. 2012, *A&A*, **547**, A10
- Đurech, J., Vokrouhlický, D., Pravec, P., et al. 2018, *A&A*, **609**, A86
- Dziadura, K., Oszkiewicz, D., & Bartczak, P. 2022, *Icarus*, **383**, 115040
- Ettl, S., Farnocchia, D., Chamberlin, A. B., & Chesley, S. R. 2020, *Icarus*, **339**, 113596
- Farinella, P., Vokrouhlický, D., & Hartmann, W. K. 1998, *Icarus*, **132**, 378
- Farnocchia, D., Chesley, S., Vokrouhlický, D., et al. 2013, *Icarus*, **224**, 1
- Farnocchia, D., Chesley, S., Chamberlin, A., & Tholen, D. 2015, *Icarus*, **245**, 94
- Farnocchia, D., Chesley, S. R., Milani, A., Gronchi, G. F., & Chodas, P. W. 2015, *Orbits, Long-Term Predictions, Impact Monitoring*, 815
- Farnocchia, D., Chesley, S. R., Takahashi, Y., et al. 2021, *Icarus*, **369**, 114594
- Ford, T. F., Benner, L. A., Brozovic, M., et al. 2014, in *AAS/Division for Planetary Sciences Meeting Abstracts*, **46**, 213
- Gaia Collaboration (Brown, A.G.A., et al.) 2018, *A&A*, **616**, A1
- Golubov, O., Kravets, Y., Krugly, Y. N., & Scheeres, D. 2016, *MNRAS*, **458**, 3977
- Goossens, S., Rowlands, D. D., Mazarico, E., et al. 2021, *Planet. Sci. J.*, **2**, 219
- Granvik, M., Morbidelli, A., Jedicke, R., et al. 2018, *Icarus*, **312**, 181
- Greenberg, A. H., Margot, J.-L., Verma, A. K., Taylor, P. A., & Hodge, S. E. 2017, *Yarkovsky Drift Detections for 159 Near-Earth Asteroids* (eScholarship, University of California)
- Greenberg, A. H., Margot, J.-L., Verma, A. K., Taylor, P. A., & Hodge, S. E. 2020, *AJ*, **159**, 92
- Grott, M., Knollenberg, J., Hamm, M., et al. 2019, *Nat. Astron.*, **3**, 971
- Hanuš, J., Delbo', M., Durech, J., & Alí-Lagoa, V. 2015, *Icarus*, **256**, 101
- Hanuš, J., Delbo', M., Vokrouhlický, D., et al. 2016, *A&A*, **592**, A34
- Hanuš, J., Vokrouhlický, D., Delbo', M., et al. 2018, *A&A*, **620**, A8
- Hergenrother, C., Maleszewski, C., Nolan, M., et al. 2019, *Nat. Commun.*, **10**, 1
- Hromakina, T., Birlan, M., Barucci, M. A., et al. 2021, *A&A*, **656**, A89
- Huang, J., Ji, J., Ye, P., et al. 2013, *Sci. Rep.*, **3**, 3411
- Hudson, R. S., Ostro, S. J., & Harris, A. W. 1997, *Icarus*, **130**, 165
- Hung, D., Hanuš, J., Masiero, J. R., & Tholen, D. J. 2022, *Planet. Sci. J.*, **3**, 56
- Jackson, S. L., Rozitis, B., Dover, L. R., et al. 2022, *MNRAS*, **513**, 3076
- Jones, E., Oliphant, T., & Peterson, P. 2001, SciPy: Open Source Scientific Tools for Python, <http://www.scipy.org>
- JPL Solar System Dynamics 2022a, JPL Small-Body Database Lookup, <https://ssd.jpl.nasa.gov/sbdb.cgi>
- JPL Solar System Dynamics 2022b, JPL Small-Body Radar Astrometry, <https://ssd.jpl.nasa.gov/?radar>
- Kaasalainen, M., Durech, J., Warner, B. D., Krugly, Y. N., & Gaftonyuk, N. M. 2007, *Nature*, **446**, 420
- Kim, M. J., Lee, H. J., Lee, S. M., et al. 2018, *A&A*, **619**, A123
- La Spina, A., Paolicchi, P., Kryszczyńska, A., & Pravec, P. 2004, *Nature*, **428**, 400
- Lauretta, D., Balram-Knutson, S., Beshore, E., et al. 2017, *Space Sci. Rev.*, **212**, 925
- Mahlke, M., Carry, B., & Mattei, P. A. 2022, *A&A*, **665**, A26
- Mainzer, A., Grav, T., Bauer, J., et al. 2011, *ApJ*, **743**, 156
- Mainzer, A., Grav, T., Masiero, J., et al. 2012, *ApJ*, **760**, L12
- Mainzer, A., Bauer, J., Grav, T., et al. 2014, *ApJ*, **784**, 110
- Marchis, F., Enriquez, J. E., Emery, J. P., et al. 2012, *Icarus*, **221**, 1130
- Masiero, J. R., Mainzer, A. K., Grav, T., et al. 2011, *ApJ*, **741**, 68
- Masiero, J. R., Mainzer, A., Grav, T., et al. 2012, *ApJ*, **759**, L8
- Masiero, J. R., Grav, T., Mainzer, A., et al. 2014, *ApJ*, **791**, 121
- Masiero, J. R., Nugent, C., Mainzer, A. K., et al. 2017, *AJ*, **154**, I68
- Masiero, J. R., Wright, E. L., & Mainzer, A. K. 2019, *AJ*, **158**, 97
- Masiero, J. R., Mainzer, A. K., Bauer, J. M., et al. 2020a, *Planet. Sci. J.*, **1**, 5
- Masiero, J. R., Smith, P., Teodoro, L. D., et al. 2020b, *Planet. Sci. J.*, **1**, 9
- Masiero, J. R., Mainzer, A. K., Bauer, J. M., et al. 2021, *Planet. Sci. J.*, **2**, 162
- Mignard, F., Cellino, A., Muinonen, K., et al. 2007, *Earth Moon Planets*, **101**, 97
- Milani, A., & Gronchi, G. 2010, *Theory of Orbit Determination* (Cambridge University Press)
- Milani, A., Sansaturio, M. E., Tommei, G., Arratia, O., & Chesley, S. R. 2005, *A&A*, **431**, 729
- Minor Planet Center 2022, IAU MPC, <http://minorplanetcenter.net>
- Mouret, S. 2011, *Phys. Rev. D*, **84**, 122001
- Mouret, S., & Mignard, F. 2011, *MNRAS*, **413**, 741
- Mueller, M. 2012, ArXiv e-prints [arXiv:1208.3993]
- Mueller, M., Delbo', M., Hora, J. L., et al. 2011, *AJ*, **141**, 109
- Muinonen, K., Fedorets, G., Pentikäinen, H., et al. 2016, *Planet. Space Sci.*, **123**, 95
- Müller, T., Kiss, C., Scheirich, P., et al. 2014, *A&A*, **566**, A22
- Myhrvold, N., Pinchuk, P., & Margot, J.-L. 2022, *Planet. Sci. J.*, **3**, 30
- Nesvorný, D., & Bottke, W. F. 2004, *Icarus*, **170**, 324
- Nugent, C., Margot, J., Chesley, S., & Vokrouhlický, D. 2012, *AJ*, **144**, 60
- Nugent, C. R., Mainzer, A., Masiero, J., et al. 2015, *ApJ*, **814**, 117
- Nugent, C. R., Mainzer, A., Bauer, J., et al. 2016, *AJ*, **152**, 63
- Okada, T., Fukuhara, T., Tanaka, S., et al. 2020, *Nature*, **579**, 518
- Ostro, S. J., Margot, J.-L., Benner, L. A. M., et al. 2006, *Science*, **314**, 1276
- Oszkiewicz, D., Muinonen, K., Virtanen, J., & Granvik, M. 2009, *Meteor. Planet. Sci.*, **44**, 1897
- Pérez-Hernández, J. A., & Benet, L. 2022, *Commun. Earth Environ.*, **3**, 1
- Rozitis, B., & Green, S. F. 2014, *A&A*, **568**, A43
- Rozitis, B., Duddy, S. R., Green, S. F., & Lowry, S. C. 2013, *A&A*, **555**, A20
- Rozitis, B., MacLennan, E., & Emery, J. P. 2014, *Nature*, **512**, 174
- Rubincam, D. P. 1988, *J. Geophys. Res.: Solid Earth*, **93**, 13805
- Scheirich, P., & Pravec, P. 2009, *Icarus*, **200**, 531
- Scheirich, P., Pravec, P., Kušnirák, P., et al. 2021, *Icarus*, **360**, 114321
- Sergeyev, A. V., & Carry, B. 2021, *A&A*, **652**, A59
- Shepard, M. K., Clark, B. E., Nolan, M. C., et al. 2008, *Icarus*, **193**, 20
- Shimaki, Y., Senshu, H., Sakatani, N., et al. 2020, *Icarus*, **348**, 113835
- Spoto, F., Milani, A., & Knežević, Z. 2015, *Icarus*, **257**, 275
- Spoto, F., Tanga, P., Mignard, F., et al. 2018, *A&A*, **616**, A13
- Sugita, S., Honda, R., Morota, T., et al. 2019, *Science*, **364**, eaaw0422
- Tanga, P., Pauwels, T., Mignard, F., et al. 2023, *A&A*, **674**, A12
- Taylor, M. B. 2005, in *ASP Conf. Ser.*, **347**, Astronomical Data Analysis Software and Systems XIV, eds. P. Shopbell, M. Britton, & R. Ebert, 29
- Trilling, D. E., Mueller, M., Hora, J. L., et al. 2010, *AJ*, **140**, 770
- Usui, F., Kuroda, D., Müller, T. G., et al. 2011, *PASJ*, **63**, 1117
- Vereš, P., Farnocchia, D., Chesley, S. R., & Chamberlin, A. B. 2017, *Icarus*, **296**, 139
- Virtanen, J., Muinonen, K., & Bowell, E. 2001, *Icarus*, **154**, 412
- Vokrouhlický, D. 1998, *A&A*, **335**, 1093
- Vokrouhlický, D., Bottke, W. F., Chesley, S. R., Scheeres, D. J., & Statler, T. S. 2015a, *The Yarkovsky and YORP Effects*, eds. P. Michel, F. DeMeo, & W. F. Bottke, 509
- Vokrouhlický, D., Farnocchia, D., Čapek, D., et al. 2015b, *Icarus*, **252**, 277
- Warner, B. D. 2018, *Minor Planet Bull.*, **45**, 138
- Watanabe, S., Hirabayashi, M., Hirata, N., et al. 2019, *Science*, **364**, 268
- Wolters, S. D., & Green, S. F. 2009, *MNRAS*, **400**, 204

Appendix A: Results of the Yarkovsky effect and densities.

Table A.1. Estimated Yarkovsky effect for all accepted cases, orbital and physical parameters including determined densities.

Num	Name	Tax.	da/dt (10^{-4} au/My)	Density (kg/m^3)	H (mag)	D (km)	p_V	Γ (SI)	γ (deg.)	$R_{Tax.}$	R_D	R_T	R_Y
1566	Icarus	S	-4.81 ± 0.31	1684^{+277}_{-331}	16.34	1.07 ± 0.06	0.45 ± 0.10			2	3,4,5		1
1685	Toro	S	-2.15 ± 0.18	1139^{+134}_{-138}	14.33	3.60 ± 0.15	0.25 ± 0.05	335^{+85}_{-55}	158.50 ± 10.00	2	6	6	6
1862	Apollo	Q	-1.91 ± 0.14	2793^{+411}_{-507}	16.08	1.55 ± 0.07	0.27 ± 0.06	150^{+140}_{-109}	162.30 ± 5.00	2	7	43,44	7
1865	Cerberus	Q	-5.49 ± 1.14	1090^{+310}_{-252}	16.73	1.20 ± 0.12	0.25 ± 0.05	864^{+219}_{-134}	175.50 ± 5.00	2	6	45,6	6
1943	Anteros	S	-2.11 ± 0.51	1367^{+516}_{-486}	15.60	2.31 ± 0.05	0.19 ± 0.04			2	3,8,9		1
2062	Aten	Q	-5.17 ± 0.34	1473^{+639}_{-888}	17.10	0.77 ± 0.03	0.44 ± 0.09			2	10,3		17
2063	Bacchus	Q	-6.21 ± 0.98	609^{+330}_{-296}	17.25	1.03 ± 0.03	0.21 ± 0.04		114.20 ± 10.00	2	10	46	56
2100	Ra-Shalom	K	-3.12 ± 0.26	1284^{+329}_{-506}	16.24	2.30 ± 0.20	0.11 ± 0.03		158.00 ± 5.00	2	11	47	57
3103	Eger	S	-2.95 ± 0.77	1513^{+538}_{-388}	15.19	1.24 ± 0.06	0.96 ± 0.20		177.60 ± 4.00	2	4,12,13,8	48	57
3200	Phaethon	B	-10.72 ± 0.83	104^{+26}_{-21}	14.32	4.98 ± 0.21	0.13 ± 0.03	654^{+221}_{-220}	152.60 ± 10.00	2	14,15,16	49	15,16,14
3908	Nyx	V	3.01 ± 0.50	2046^{+751}_{-679}	17.33	1.00 ± 0.15	0.21 ± 0.07			2	17		1
4179	Toutatis	S	-2.78 ± 0.27	727^{+226}_{-245}	15.24	2.73 ± 0.19	0.16 ± 0.03			2	18		1
4769	Castalia	S	-5.18 ± 1.69	-2402^{+730}_{-731}	16.90	1.40 ± 0.03	0.16 ± 0.03		74.20 ± 13.00	2	19	50	50
6239	Minos	S	5.40 ± 0.87	2478^{+1163}_{-946}	18.49	0.47 ± 0.10	0.32 ± 0.15			2	9		1
7335	1989 JA		-6.50 ± 1.96	960^{+370}_{-449}	17.00	0.73 ± 0.02	0.52 ± 0.10				10,20,21		1
7341	1991 VK	Q	-2.90 ± 0.55	1829^{+726}_{-581}	16.70	0.79 ± 0.04	0.59 ± 0.12			2	12,19,13		1
7482	1994 PC1	S	-4.01 ± 0.71	1298^{+684}_{-475}	16.50	1.05 ± 0.30	0.40 ± 0.24			2	5		1
7822	1991 CS	S	-3.96 ± 0.79	1469^{+424}_{-424}	17.33	1.44 ± 0.01	0.10 ± 0.02			2	19,8,22,20		1
10302	1989 ML	E	21.15 ± 1.25	1042^{+503}_{-492}	19.40	0.24 ± 0.04	0.51 ± 0.20			2	8,9		1
11054	1991 FA	S	-1.89 ± 0.40	1921^{+973}_{-780}	16.90	1.13 ± 0.28	0.24 ± 0.10			2			1
17511	1992 QN	K	1.17 ± 0.04		17.30	0.94 ± 0.24	0.24 ± 0.10		115.80 ± 5.00	2		51	51
22099	2000 EX106	S	0.58 ± 0.11		17.90	0.58 ± 0.10	0.36 ± 0.14			2	10,9		1
29075	1950 DA	L	-2.53 ± 0.37	2322^{+544}_{-528}	17.10	1.35 ± 0.14	0.14 ± 0.04	36^{+20}_{-14}	167.70 ± 2.50	2	21,23,20	52	24
33342	1998 WT24	K	-14.09 ± 1.67	485^{+221}_{-205}	17.90	0.40 ± 0.06	0.75 ± 0.27	200^{+100}_{-100}	105.20 ± 5.00	2	25,4	53	26
38086	Beowulf		-15.47 ± 3.21	525^{+267}_{-230}	17.29	0.69 ± 0.16	0.45 ± 0.22			2	10,8		1
52750	1998 KK17	V	1.05 ± 0.02		16.45	1.05 ± 0.02	0.42 ± 0.08			2	10,22,20		1
55408	2001 TC2		-12.20 ± 3.31	1277^{+544}_{-728}	18.80	0.46 ± 0.01	0.25 ± 0.05		165.40 ± 3.00	2	20	27	27
66391	Moshup	Q	-3.83 ± 1.06	2265^{+728}_{-629}	16.58	1.32 ± 0.04	0.24 ± 0.05			2	27		27
68950	2002 QF15	S	-3.72 ± 0.63	1257^{+673}_{-648}	16.36	1.13 ± 0.04	0.40 ± 0.08			2	28,12,23,13,19		1
85953	1999 FK21	S	-13.92 ± 1.20	858^{+462}_{-452}	18.10	0.63 ± 0.13	0.25 ± 0.11			2	19,29,30		1
85989	1999 JD6	K	-4.26 ± 0.98	1202^{+525}_{-494}	17.06	1.62 ± 0.03	0.10 ± 0.02			2	20,10,23,31,8,30		1
86667	2000 FO10	S	6.41 ± 2.01	896^{+731}_{-494}	17.56	0.74 ± 0.02	0.31 ± 0.06			2	10,23		1
87024	2000 JS66	S	11.37 ± 1.66	1450^{+751}_{-719}	18.70	0.31 ± 0.05	0.60 ± 0.22			2	9		1
88710	2001 SL9	S	-3.49 ± 1.11	2032^{+1561}_{-619}	17.60	0.75 ± 0.29	0.29 ± 0.23			2	10		1
99907	1989 VA	Q	12.44 ± 0.75	966^{+300}_{-312}	17.90	0.64 ± 0.17	0.30 ± 0.17			2	28,30		1
99935	2002 AV4	L	-8.28 ± 2.22	430^{+312}_{-187}	16.04	1.53 ± 0.27	0.29 ± 0.11			2	25,23,28		1
105140	2000 NL10	Q	1.97 ± 0.05	2069^{+1094}_{-152}	15.73	1.97 ± 0.05	0.23 ± 0.04			32	10		1
137924	2000 BD19	V	-8.46 ± 2.33	862^{+152}_{-374}	17.20	0.97 ± 0.04	0.25 ± 0.05			33	20		1

138852	2000 WN10	S	18.27 ± 2.01	2203 ⁺⁷⁰⁸ ₋₅₃₄	20.20	0.25±0.06	0.24±0.10	10.00±5.00	2		54	54
138947	2001 BA40	S	-17.24 ± 4.34	857 ⁺⁴⁶³ ₋₃₇₈	18.60	0.44±0.09	0.33±0.15		2		9,3	1
141531	2002 GB	S	19.54 ± 4.67	1016 ⁺⁵³⁷ ₋₅₄₃	19.15	0.30±0.01	0.42±0.09		2		20	1
161989	Cacus	S	-3.51 ± 0.57	3701 ⁺⁷⁷⁶ ₋₅₉₄	17.20	0.68±0.03	0.51±0.10	177.70±2.00	2		10,30,20	47
162142	1998 VR	S	8.40 ± 1.69	1287 ⁺⁸²⁶ ₋₆₈₃	18.70	0.55±0.19	0.20±0.14		2		19,30	1
162173	Ryugu	C	0.90 ± 0.01		19.39	0.90±0.01	0.04±0.00	325 ⁺⁶⁶ ₋₄₆	2		34	34
162181	1999 LF6	S	-6.24 ± 1.54	1348 ⁺⁶²⁴ ₋₅₉₁	18.20	0.73±0.02	0.17±0.03		2		3,20	1
163000	2001 SW169	S	-11.66 ± 1.74	1145 ⁺⁶³⁶ ₋₄₈₂	19.20	0.45±0.18	0.18±0.15		2		23	1
163243	2002 FB3	S	1.62 ± 0.01	3029 ⁺²⁰⁰⁶ ₋₁₈₄₆	16.52	1.62±0.01	0.17±0.03		2		30,22,20,19	1
164206	2004 FN18	M	-4.32 ± 1.21	868 ⁺³⁹⁷ ₋₃₇₇	17.63	1.27±0.58	0.10±0.09		2		10,19	1
172034	2001 WR1	S	-4.14 ± 1.20	2556 ⁺¹⁰⁴⁶ ₋₈₂₇	17.80	0.63±0.02	0.34±0.07		39,40		3,10	1
188174	2002 JC	S	-10.42 ± 2.71	867 ⁺⁴⁵⁵ ₋₃₃₉	17.33	0.93±0.23	0.24±0.10		2			1
192563	1998 WZ6	V	-9.03 ± 2.47	749 ⁺³⁸⁹ ₋₃₂₁	17.25	0.88±0.19	0.29±0.10		2			1
276409	2002 YN2	S	0.68 ± 0.02		18.50	0.54±0.14	0.24±0.10		2			1
311554	2006 BQ147	S	-16.30 ± 3.48	1178 ⁺⁵²⁵ ₋₅₀₆	18.70	0.38±0.02	0.41±0.09		2		10	1
317643	2003 FH1	D	0.78 ± 0.03	6339 ⁺²⁰⁰⁶ ₋₂₀₀₀	18.20	0.62±0.16	0.24±0.10		41			1
345705	2006 VB14	Q	-13.34 ± 2.81	1431 ⁺⁷²⁶ ₋₅₄₅	18.50	0.40±0.10	0.44±0.23		2		5,19,28	1
363505	2003 UC20	P	-3.85 ± 0.20	1290 ⁺⁵⁶³ ₋₇₁₇	18.40	1.88±0.01	0.02±0.00		2		10,3	1
385186	1994 AW1	L	4.01 ± 0.67	2287 ⁺⁷³⁶ ₋₈₃₂	17.60	0.82±0.03	0.24±0.05		2		19,10,42	1

Notes. R_{Tax.}, R_D, R_r, R_y are references of the parameters: taxonomy, diameter, thermal inertia and obliquity. 1: present study (PDF), 2: Mahliké et al. (2022), 3: Nugent et al. (2015), 4: Wolters & Green (2009), 5: Mainzer et al. (2012), 6: Hung et al. (2022), 7: Rozitis et al. (2013), 8: Trilling et al. (2010), 9: Mueller et al. (2011), 10: Nugent et al. (2016), 11: Shepard et al. (2008), 12: Usui et al. (2011), 13: Alf-Lagoa et al. (2018), 14: Masiero et al. (2019), 15: Hanuš et al. (2018), 16: Hanuš et al. (2016), 17: Benner et al. (2002), 18: Huang et al. (2013), 19: Masiero et al. (2017), 20: Mainzer et al. (2011), 21: Masiero et al. (2011), 22: Myhrvold et al. (2022), 23: Masiero et al. (2021), 24: Rozitis et al. (2014), 25: Delbo (2004), 26: Mueller (2012), 27: Ostro et al. (2006), 28: Masiero et al. (2020a), 29: Delbó et al. (2003), 30: Masiero et al. (2020b), 31: Mainzer et al. (2014), 32: Dandy et al. (2003), 33: Binzel et al. (2019), 34: Watanabe et al. (2019), 35: Shimaki et al. (2020), 36: Grott et al. (2019), 37: Okada et al. (2020), 38: Stigita et al. (2019), 39: Carry et al. (2016), 40: Sergeev & Carry (2021), 41: Hromakina et al. (2021), 42: Marchis et al. (2012), 43: Durech et al. (2008), 44: Kaasalainen et al. (2007), 45: Hanuš et al. (2015), 46: Benner et al. (1999), 47: Durech et al. (2018), 48: Durech et al. (2012), 49: Kim et al. (2018), 50: Hudson et al. (1997), 51: Warner (2018), 52: Busch et al. (2007), 53: Busch et al. (2008), 54: referee 55: Jackson et al. (2022), 56: Durech et al. (2018), 57: Durech et al. (2012).